Die approbierte gedruckte Originalversion dieser Diplomarbeit ist an der TU Wien Bibliothek verfügbar
The approved original version of this thesis is available in print at TU Wien Bibliothek.

TECHNISCHE UNIVERSITÄT WIEN

DIPLOMARBEIT

MACHINE LEARNING-BASED ISOCITRATDEHYDROGENASE AND GRADE CLASSIFICATION OF GLIOMAS USING HIGH-RESOLUTION 7T MAGNETIC RESONANCE SPECTROSCOPY IMAGING

Technische Universität Wien
Atominstitut

Medizinische Universität Wien
High Field Magnetic Resonance Center

Betreuer

Em.Univ.Prof. Dipl.-Ing. Dr.techn. Gerald BADUREK
Ao.Univ.Prof. Dipl.-Ing. Dr.techn. Martin GRÖSCHL
Privatdoz. Dipl.-Ing. Gilbert HANGEL, PhD

Eingereicht von

Sukrit SHARMA, BSc
sukritsharmap@gmail.com
Matrikel-Nr: 01429163
UE 066 453– Masterstudium Biomedical Engineering

TU Bibliothek Your knowledge hub WIEN

Die approbierte gedruckte Originalversion dieser Diplomarbeit ist an der TU Wien Bibliothek verfügbar
The approved original version of this thesis is available in print at TU Wien Bibliothek.

TECHNISCHE UNIVERSITÄT WIEN

MASTER'S THESIS

MACHINE LEARNING-BASED ISOCITRATDEHYDROGENASE AND GRADE CLASSIFICATION OF GLIOMAS USING HIGH-RESOLUTION 7T MAGNETIC RESONANCE SPECTROSCOPY IMAGING

Vienna University of Technology
Atominstitute

Medical University of Vienna
High Field Magnetic Resonance Center

Supervisors

Em.Univ.Prof. Dipl.-Ing. Dr.techn. Gerald BADUREK
Ao.Univ.Prof. Dipl.-Ing. Dr.techn. Martin GRÖSCHL
Privatdoz. Dipl.-Ing. Gilbert HANGEL, PhD

Submitted by

Sukrit SHARMA, BSc
sukritsharmap@gmail.com
Student ID: 01429163

UE 066 453–Master's Programme Biomedical Engineering

Die approbierte gedruckte Originalversion dieser Diplomarbeit ist an der TU Wien Bibliothek verfügbar
The approved original version of this thesis is available in print at TU Wien Bibliothek.

TU WIEN Bibliothek Your knowledge hub
Die approbierte gedruckte Originalversion dieser Diplomarbeit ist an der TU Wien Bibliothek verfügbar
The approved original version of this thesis is available in print at TU Wien Bibliothek.

Abstract (EN)

Detecting the presence, molecular-genetic properties, and volume of neoplastic lesions is important for modern medical image processing studies. For example, precise lesion classification according to up-to-date WHO guidelines, relevant for treatment decisions, is currently not automatically feasible in brain tumors. This thesis is a part of the development of a processing pipeline for the quantification of lesions through a statistical evaluation of tumor regions of interest (ROI) in high-resolution 7 Tesla (7T) magnetic resonance spectroscopy imaging (MRSI). MRSI enables the detection of the presence and concentration of different metabolites in body tissues based on their resonance frequency. Compared to 3T MRSI, 7T MRSI with a higher signal-to-noise ratio and increased spectral dispersion makes measurement of additional metabolites possible.

The first step of the processing pipeline involved statistical evaluation between different hotspot regions based on manual segmentation by a neuroradiologist. In the second step, statistical tests were performed on hotspot segmentation, including a contrast enhancement (CE) region, a non-contrast enhancement (nCE) region, and a necrosis (NEC) region extracted from a clinical segmentation. The evaluation involved comparing different regions and metabolites ratios like total Choline (tCho) to total creatine (tCr) using a Boxplot diagram with the Mann-Whitney-Wilcoxen Test and classification of IDH mutation and grade using random forest. Isocitrate dehydrogenase (IDH) is an enzyme that plays a vital role in cell homeostasis and metabolic processes and is involved in the glioma cycle. This study's main objective was finding the most important metabolite ratios for the classification of IDH mutation status and grade, utilizing the capability of 7T to detect multiple metabolites

Die approbierte gedruckte Originalversion dieser Diplomarbeit ist an der TU Wien Bibliothek verfügbar
The approved original version of this thesis is available in print at TU Wien Bibliothek.
TU Bibliothek Your knowledge hub WIEN

with high resolution and to use them for classification. Comparison between different machine learning methods allows differentiating between classifiers and obtaining better accuracy. It also helps us to determine the robustness of our classification algorithm. Random forest and support vector machine (SVM) are compared in this study.

Using multiple features, the AUC of 0.85 was achieved for IDH classification and 0.91 for grade classification. The spatial resolution of 7T MRSI makes achieving high accuracy in IDH and grade classification possible even with a small cohort of patients.

Die approbierte gedruckte Originalversion dieser Diplomarbeit ist an der TU Wien Bibliothek verfügbar
The approved original version of this thesis is available in print at TU Wien Bibliothek.
TU Bibliothek Your knowledge hub WIEN

Abstract (De)

Die Erkennung des Vorhandenseins, der molekulargenetischen Eigenschaften und des Volumens von neoplastischen Läsionen ist für moderne medizinische Bildverarbeitungsstudien von großer Bedeutung. So ist beispielsweise bei Hirntumoren eine präzise Klassifizierung der Läsionen nach den aktuellen WHO-Richtlinien, die für Behandlungsentscheidungen relevant ist, derzeit nicht automatisch möglich. Diese Arbeit ist Teil der Entwicklung einer Verarbeitungspipeline zur Quantifizierung von Läsionen durch eine statistische Auswertung von Tumorregionen von Interesse (ROI) in hochauflösender 7 Tesla (7T) Magnetresonanzspektroskopie-Bildgebung (MRSI). MRSI ermöglicht den Nachweis des Vorhandenseins und der Konzentration verschiedener Metaboliten in Körpergeweben auf der Grundlage ihrer Resonanzfrequenz. Im Vergleich zur 3T-MRSI ermöglicht die 7T-MRSI mit einem höheren Signal-Rausch-Verhältnis und einer größeren spektralen Streuung die Messung zusätzlicher Metaboliten.

Der erste Schritt der Verarbeitungspipeline umfasste die statistische Auswertung zwischen verschiedenen Hotspot-Regionen auf der Grundlage einer manuellen Segmentierung durch einen Neuroradiologen. Im zweiten Schritt wurden statistische Tests für die Hotspot-Segmentierung durchgeführt, einschließlich einer Region mit Kontrastverstärkung (CE), einer Region ohne Kontrastverstärkung (nCE) und einer Region mit Nekrose (NEC), die aus einer klinischen Segmentierung extrahiert wurde. Die Auswertung umfasste den Vergleich verschiedener Regionen und Metaboliten-Verhältnisse wie Gesamt-Cholin (tCho) zu Gesamt-Kreatin (tCr) unter Verwendung eines Boxplot-Diagramms mit dem Mann-Whitney-Wilcoxen-Test und die Klassifizierung von IDH-Mutation und -Grad unter Verwendung von Random Forest.

Die approbierte gedruckte Originalversion dieser Diplomarbeit ist an der TU Wien Bibliothek verfügbar
The approved original version of this thesis is available in print at TU Wien Bibliothek.
TU Bibliothek Your knowledge hub WIEN

Isocitrat-Dehydrogenase (IDH) ist ein Enzym, das eine wichtige Rolle bei der Zellhomöostase und bei Stoffwechselprozessen spielt und am Gliomzyklus beteiligt ist. Hauptziel dieser Studie war es, die wichtigsten Metabolitenverhältnisse für die Klassifizierung von IDH-Mutationsstatus und -Grad zu finden, wobei die Fähigkeit des 7T genutzt wurde, mehrere Metaboliten mit hoher Auflösung zu erkennen und sie für die Klassifizierung zu verwenden. Der Vergleich zwischen verschiedenen Methoden des maschinellen Lernens ermöglicht es, zwischen den Klassifikatoren zu unterscheiden und eine bessere Genauigkeit zu erzielen. Er hilft uns auch, die Robustheit unseres Klassifizierungsalgorithmus zu bestimmen. In dieser Studie werden Random Forest und Support Vector Machine (SVM) miteinander verglichen.

Bei Verwendung mehrerer Merkmale wurde ein AUC von 0,85 für die IDH-Klassifizierung und 0,91 für die Grad-Klassifikation.Die räumliche Auflösung der 7T MRSI ermöglicht eine hohe Genauigkeit bei der IDH- und Grad-Klassifikation auch bei einer kleinen Patientenkohorte.

Die approbierte gedruckte Originalversion dieser Diplomarbeit ist an der TU Wien Bibliothek verfügbar
The approved original version of this thesis is available in print at TU Wien Bibliothek.

Acknowledgements

First and foremost, I would like to express my deep appreciation to my supervisor Privatdozent Gilbert Hangel, PhD, for his insightful feedback and constructive suggestions, which have significantly enhanced the quality of my work. His counsel and motivation have been a noteworthy contribution to my academic triumph. I wish to convey my profound gratitude to my supervisors, Professor Gerald Badurek, Professor Martin Gröschl and Professor Wolfgang Bogner, for their guidance, backing, and proficiency.

My profound gratitude to my mother, Sarita, and my late father, Govinda, for their steadfast love, support, and motivation throughout my academic odyssey. Their sacrifices and unwavering encouragement have been the motivation behind my achievements. I wish to convey my heartfelt love and appreciation for my wife, Nandita, for her forbearance, comprehension, and backing during the challenging phases of my research. Her persistent faith in me has been a perpetual fount of inspiration. My sisters, Samikshya and Samrachana, and my brother-in-law, Anish, have been a stronghold throughout my studies. Their constant encouragement and support have been priceless. I am grateful to my in-laws, Alaka, Rudra, and Dhawal, for their affection and backing. Their insightful inputs and recommendations have been of immense aid. Furthermore, my heartfelt appreciation to the Dhungana family in Austria for their continuous love and support.

I would like to recognize the valuable contribution of my colleagues, Cornelius, Philipp, and Roxane, who have provided me with indispensable resources and tools to conduct my research. My heartfelt thanks go out to all my colleagues in the HFMR Center for all the good times we spent together.

Thank you all for being a part of my academic expedition and for your valuable

Die approbierte gedruckte Originalversion dieser Diplomarbeit ist an der TU Wien Bibliothek verfügbar
The approved original version of this thesis is available in print at TU Wien Bibliothek.
TU Bibliothek Your knowledge hub WIEN

contribution to the successful completion of my Master's thesis.

TU Bibliothek Your knowledge hub WIEN
Die approbierte gedruckte Originalversion dieser Diplomarbeit ist an der TU Wien Bibliothek verfügbar
The approved original version of this thesis is available in print at TU Wien Bibliothek.

Die approbierte gedruckte Originalversion dieser Diplomarbeit ist an der TU Wien Bibliothek verfügbar
The approved original version of this thesis is available in print at TU Wien Bibliothek.

Contents

1 Introduction **1**

1.1 Nuclear Magnetic Resonance (NMR) 2

1.1.1 Magnetic Resonance Imaging 7

1.1.2 Signal localization 8

1.1.3 Image acquisition 13

1.1.4 Image quality 14

1.1.5 Pulse sequence 15

1.1.6 Magnetic Resonance Spectroscopy (MRS) 16

1.1.7 Magnetic Resonance Spectroscopy Imaging (MRSI) 20

1.1.8 7 Tesla Magnetic Resonance Spectroscopy Imaging (7T MRSI) 24

1.1.9 Water and lipid suppression 25

1.2 Glioma 31

1.2.1 Isocitrate dehydrogenase (IDH) 34

1.3 Classification 35

1.3.1 Random forest 35

1.3.2 Support Vector Machine (SVM) 36

1.3.3 Feature Selection 37

Die approbierte gedruckte Originalversion dieser Diplomarbeit ist an der TU Wien Bibliothek verfügbar
The approved original version of this thesis is available in print at TU Wien Bibliothek.

1.3.4 Receiver Operating Characteristic (ROC) curve and Area Under the Curve (AUC) 38

2 Methods **43**

2.1 Patient recruitment 43

2.2 Measurement Procedure 45

2.3 Data post-processing 46

2.4 Pipeline 47

2.4.1 Tumor segmentation 48

2.4.2 Preliminary image quality assessment 49

2.5 MRSI Statistical Evaluation 50

2.5.1 CSV Database 51

2.5.2 Histogram Analysis 53

2.5.3 Mann-Whitney-Wilcoxon Test and Boxplot 53

2.5.4 IDH Classification 54

2.5.5 Grade Classification 55

2.5.6 Threshold Comparisons 55

2.5.7 Single vs Multiple Feature Comparison 57

2.5.8 ROC Curve and AUC 57

3 Results **59**

3.1 Histogram analysis and threshold 59

3.2 IDH and grade differentiation 63

3.3 IDH and grade classification 65

3.4 ROC curve and AUC 69

3.4.1 Classification with multiple features 71

Die approbierte gedruckte Originalversion dieser Diplomarbeit ist an der TU Wien Bibliothek verfügbar
The approved original version of this thesis is available in print at TU Wien Bibliothek.
TU Bibliothek Your knowledge hub WIEN

3.4.2 Classification with a single feature 73

4 Discussion **79**

4.1 Classification with a single feature 81

4.2 Classifictaion with multiple features 82

4.2.1 IDH Classification 82

4.2.2 Grade Classification 82

5 Conclusion and Outlook **85**

Die approbierte gedruckte Originalversion dieser Diplomarbeit ist an der TU Wien Bibliothek verfügbar
The approved original version of this thesis is available in print at TU Wien Bibliothek.

TU Bibliothek Your knowledge hub WIEN
Die approbierte gedruckte Originalversion dieser Diplomarbeit ist an der TU Wien Bibliothek verfügbar
The approved original version of this thesis is available in print at TU Wien Bibliothek.

List of Figures

1.1 Nuclei with longitudinal and transverse magnetization 6
1.2 Magnetic Resonance Image (MRI) scanner 7
1.3 Magnetic field gradient approach for a slice selection 10
1.4 frequency-gradient (G_F) and phase-gradient (G_P) 11
1.5 Fourier transformation from k-space to the image space 13
1.6 Spin Echo (SE) signal 16
1.7 Spin echo (SE) pulse sequence 17
1.8 MRSI pulse sequence without a SE 21
1.9 Pulse sequence for FID MRSI 23
1.10 Point-resolved Spectroscopy (PRESS) and Stimulated Echo Acquisition Mode (STEAM) 24
1.11 Chemical Shift Selective Saturation (CHESS) pulse sequence 25
1.12 outer volume suppression (OVS) 27
1.13 Metabolites spectrum in white matter(WM) and grey matter (GM) of the brain 28
1.14 Decision tree 36
1.15 SVM Margins 37
1.16 Confusion matrix 39

Die approbierte gedruckte Originalversion dieser Diplomarbeit ist an der TU Wien Bibliothek verfügbar
The approved original version of this thesis is available in print at TU Wien Bibliothek.
TU Bibliothek Your knowledge hub WIEN

1.17 Receiver Operating Characteristic (ROC) curve and Area Under the Curve (AUC) . . . 41

2.1 Sankey plot for data distribution . . . 45
2.2 Tumor segmentation including peritumoral region . . . 48
2.3 Process of statistical evaluation . . . 50
2.4 Database structure . . . 53

3.1 Histogram plot for all patients . . . 60
3.2 Histogram plot for single patients . . . 61
3.3 Sankey diagram with the patient to segmentation data flow . . . 62
3.4 Boxplot for three ratio metabolites IDH . . . 63
3.5 Boxplot for three ratio metabolites grade . . . 64
3.6 Correlation map for the metabolite ratios . . . 66
3.7 Cross-validation score determining features idh . . . 67
3.8 Cross-validation score determining features grade . . . 67
3.9 Important features for IDH classification . . . 68
3.10 Important features for grade classification . . . 68
3.11 IDH prediction map . . . 70
3.12 ROC curve for the random forest for IDH classification . . . 71
3.13 ROC curve for SVM for IDH classification . . . 72
3.14 ROC curve for the random forest for grade classification . . . 72
3.15 ROC curve for SVM for grade classification . . . 73
3.16 ROC curve for IDH classification with GPC+PCH/NAA+NAAG using random forest . . . 74
3.17 ROC curve for IDH classification with GPC+PCH/NAA+NAAG using SVM . . . 74

Die approbierte gedruckte Originalversion dieser Diplomarbeit ist an der TU Wien Bibliothek verfügbar
The approved original version of this thesis is available in print at TU Wien Bibliothek.
TU Bibliothek Your knowledge hub WIEN

3.18 ROC curve for grade classification with GPC+PCH/NAA+NAAG using random forest 75
3.19 ROC curve for grade classification with GPC+PCH/NAA+NAAG using SVM 75
3.20 Summarized AUC for IDH classification 76
3.21 Summarized AUC for grade classification 77

Die approbierte gedruckte Originalversion dieser Diplomarbeit ist an der TU Wien Bibliothek verfügbar
The approved original version of this thesis is available in print at TU Wien Bibliothek.
TU Bibliothek Your knowledge hub WIEN

TU Bibliothek Your knowledge hub WIEN
Die approbierte gedruckte Originalversion dieser Diplomarbeit ist an der TU Wien Bibliothek verfügbar
The approved original version of this thesis is available in print at TU Wien Bibliothek.

List of Tables

2.1 Patients list with information 44
2.2 Threshold table 56

Die approbierte gedruckte Originalversion dieser Diplomarbeit ist an der TU Wien Bibliothek verfügbar
The approved original version of this thesis is available in print at TU Wien Bibliothek.

Die approbierte gedruckte Originalversion dieser Diplomarbeit ist an der TU Wien Bibliothek verfügbar
The approved original version of this thesis is available in print at TU Wien Bibliothek.

Abbreviations

3T 3 Tesla.

7T 7 Tesla.

ADC Analog-to-digital converter.

BBB Blood-brain barrier.

CHESS Chemical Shift Selective.

Cho Choline.

CNS Central nervous system.

Cr Creatine.

CRLB Cramér–Rao lower bound.

CSF cerebrospinal fluid.

CSI Chemical Shift Imaging.

CV Cross Validation.

Die approbierte gedruckte Originalversion dieser Diplomarbeit ist an der TU Wien Bibliothek verfügbar
The approved original version of this thesis is available in print at TU Wien Bibliothek.
TU Bibliothek Your knowledge hub WIEN

EPI Echo-planer Imaging.

FID Free Induction Decay.

FOV Field of view.

FT Fourier transformation.

FWHM Full width at half maximum.

G$_F$ Frequency-encoding gradient.

G$_P$ Phase-encoding gradient.

GABA γ -Aminobutyric acid.

Gln Glutamine.

Glu Glutamate.

GSH Gluthathione.

HG High Grade.

IDH Isocitrate dehydrogenase.

Ins Inositol.

LG Low Grade.

MOIST Multiple Optimizations Insensitive Suppression Train.

MRI Magnetive Resonance Imaging.

Die approbierte gedruckte Originalversion dieser Diplomarbeit ist an der TU Wien Bibliothek verfügbar
The approved original version of this thesis is available in print at TU Wien Bibliothek.
TU Bibliothek Your knowledge hub WIEN

MRS Magnetic Resonance Spectroscopy.

MRSI Magnetic Resonance Spectroscopy Imaging.

MS Multiple Sclerosis.

NAA N-acetylaspartate.

NAAG N-acetylaspartylglutamate.

NMR Nuclear Magnetic Resonance.

OVS Outer volume suppression.

PCr Phosphocreatine.

PRESS Point Resolved Spectroscopy.

PSF Point spread function.

RF Radio frequency.

RFE Recursive Feature Elimination.

RFECV Recursive Feature Elimination Cross Validation.

ROC Receiver operating characteristic.

ROI Regions of interest.

RT Repetition time.

SE Spin Echo.

Die approbierte gedruckte Originalversion dieser Diplomarbeit ist an der TU Wien Bibliothek verfügbar
The approved original version of this thesis is available in print at TU Wien Bibliothek.
TU Bibliothek Your knowledge hub WIEN

SNR signal-to-noise ratio.

STEAM Stimulated Echo Acquisition Mode.

SWAMP Suppression of Water with Adiabatic-Modulated Pulses.

Tau Taurine.

tCho Total Choline.

tCr total Creatine.

tNAA Total N-acetylaspartate.

VAPOR Variable Power radiofrequency pulses with Optimized Relaxation delays).

VOI Volume of interest.

WET Water suppression Enhanced through T1 effects.

WHO World Health Organization.

Die approbierte gedruckte Originalversion dieser Diplomarbeit ist an der TU Wien Bibliothek verfügbar
The approved original version of this thesis is available in print at TU Wien Bibliothek.
TU Bibliothek Your knowledge hub WIEN

Die approbierte gedruckte Originalversion dieser Diplomarbeit ist an der TU Wien Bibliothek verfügbar
The approved original version of this thesis is available in print at TU Wien Bibliothek.

Chapter 1

Introduction

Magnetic Resonance Spectroscopic Imaging (MRSI) has been increasingly studied for the noninvasive localization of brain tumors in the last decades. The High Field Magnetic Resonance Center at the Medical University of Vienna uses an in-house 3D MRSI sequence in a 7 Tesla (7T) Siemens Magnetom to do preoperative Magnetic Resonance Imaging (MRI) scans. The manual evaluation of vast data from 7T MRI is challenging due to thousands of intra-tumoral voxel spectra compared to about ten in a clinical MRSI scan. This thesis is part of developing a processing pipeline for quantifying brain lesions by statistically evaluating tumor regions of interest (ROI) in high-resolution 7T MRSI. The pipeline begins with a preparation of a data set for statistical evaluation. For that cause, a tabular data set is created from a 3D MRSI image. Once a tabular data set is ready, a statistical analysis of the quantification of brain lesions is performed. The main objective of this research is to show the prospect that, with the help of spectroscopic images of the wide range of metabolites obtained through MRSI, we can predict the IDH mutation status and glioma grades. MRI and MRSI are fundamentally based on Nuclear Magnetic Resonance (NMR).

So, let us begin with NMR.

1.1 Nuclear Magnetic Resonance (NMR)

The history of NMR is fascinating. From the very early period of its development, it won some Nobel Prizes. At the same time, it was acoustically unpleasant among the patients, due to which it lost its 'nuclear' identity and was an unpleasant experience among the patients. NMR was first introduced in 1938 by Isidor Isaac Rabi. His study demonstrated that a molecular beam sent through a magnetic field could emit radiofrequency waves at specific frequencies.
Furthermore, after two years, during the 1940s, two scientists independently defined the atomic and molecular magnetic resonance properties of solids and liquids. Edward Purcell experimented with solid paraffin, whereas Felix Bloch worked with water. In 1952, both scientists were jointly awarded the Nobel Prize in Physics.

Later in 1971, chemist Paul C. Lauterbur developed the first MR image of two water-filled test tubes and introduced the idea of stacking 2D images to reconstruct those into 3D images. His findings were proved outstanding in the field because they introduced the concept of living imaging tissue for the first time in the history of NMR.
During the same period, physicist Sir Peter Mansfield tried to reduce the time of magnetic resonance scans. He used echo-planar imaging (EPI), which had advantages in working with movement artefacts. Using NMR, he produced an image of a human body part (image of a finger) in 15-23 minutes. Subsequently, he imaged the cardiac cycle of a rabbit and a human. The method developed by Mansfield and Lauterbur was adopted for clinical use and was awarded the 2003 Nobel Prize in Medicine

Die approbierte gedruckte Originalversion dieser Diplomarbeit ist an der TU Wien Bibliothek verfügbar
The approved original version of this thesis is available in print at TU Wien Bibliothek.
TU Bibliothek Your knowledge hub WIEN

(Slavkovsky & Uhliar, 2004).

In 1980, John Mallard and his team at Aberdeen University introduced the clinically used whole-body MR scanner for the first time (Tabakov, 2021). It was a turning point for the use of MR. Since then, MR scanners have been vastly used, and their development has led to the clinical application of 7 Tesla MRI in modern days. Even though NMR Spectroscopy first became popular among chemists in the 1950s, MRSI has only been used in humans since the 1980s.

From a quantum mechanical perspective, the basic principle of NMR is based on the ability of specific atomic nuclei like Hydrogen-1 and Carbon-13 to transition between two different energy states in a quantum system. Purcell et al. (1946) described the phenomenon of the nuclei absorbing energy from an electromagnetic wave that reaches the high energy state and emits an electromagnetic wave signal while transitioning to a lower energy state. Quantum mechanical explanation of NMR provides a complete view of NMR. However, the interpretation of Bloch (1946) is easy to understand, which is mentioned as a classical view in literature. According to the classical analogy, the magnetic field of a magnetic body is randomly oriented until an external magnetic field is applied to it. Under the influence of the external magnetic field, the magnetic body oscillates around the magnetic field at its natural frequency. When a third magnetic effect is introduced upon the oscillating magnetic body supporting oscillation, with the frequency equal to the natural frequency of the oscillating magnetic body, the system is said to be in magnetic resonance. The resonating frequency of the magnetic field can be produced using a coil with the current flow in the coil controlling the magnetic field frequency. When the current flow is stopped in the coil, the oscillating magnetic body induces an electric voltage due to electromagnetic induction. The oscillating magnetic body, after some time, stops oscillating and aligns with the external magnetic field, which is the lowest en-

Die approbierte gedruckte Originalversion dieser Diplomarbeit ist an der TU Wien Bibliothek verfügbar
The approved original version of this thesis is available in print at TU Wien Bibliothek.
TU Bibliothek Your knowledge hub WIEN

ergy state. The highest energy state would be the alignment opposite the external magnetic field.

For a proper understanding of NMR, first, we need to know about the spin, a quantum mechanical property of nuclei, which can be a multiple of positive or negative 1/2. Spin is not easy to understand in quantum mechanics, but we can analogically relate it with classical rotation for our work. The angular momentum represents analogically the fact that the nuclei are spinning, whereas, in reality, they are not. The magnetic moment is the magnetic property of nuclei. With all these considerations, when we introduce nuclei to an external magnetic field, the magnetic moment of nuclei precesses around the magnetic field orientation in a particular frequency called Larmor frequency ω. ω is directly proportional to the external magnetic field strength $\vec{B}$ in Tesla and defined by the Larmor equation as

$$\omega = \gamma \vec{B} \tag{1.1}$$

γ is a nuclei-based constant called gyromagnetic ratio (γ). The γ of hydrogen is 42.58MHz/T.

That is, however, only the case when we observe the nuclei individually, which is, in reality, not the case. In human brain tissue, with approximately 6×10^{19} spin per cubic mm volume (De Graaf, 2019), the magnetic moment of each proton is influenced by the magnetic moment of others. Due to this fact, the net magnetization parallel to the external magnetic field is not caused by all the protons. Still, only 0.1% of protons contribute to net magnetization in the orientation of the external magnetic field (De Graaf, 2019) called equilibrium magnetization (M_0). M_0 is rotated towards the xy plane where M_0 rotates with ω frequency. A new magnetic field (B_1) perpendicular to M_0 is used to rotate M_0. B_1 here also rotates with frequency ω

Die approbierte gedruckte Originalversion dieser Diplomarbeit ist an der TU Wien Bibliothek verfügbar
The approved original version of this thesis is available in print at TU Wien Bibliothek.
TU Bibliothek Your knowledge hub WIEN

along the longitudinal axis (Z-axis) in constant phase with M_0 to ensure coherent rotation of M_0 towards the transverse plane (xy-plane). The flip angle of M_0 can be determined as

$$\alpha = 2\pi\gamma B_1 T \tag{1.2}$$

α ... flip angle [rad]

γ ... gyromagnetic ratio [T/MHz]

B_1 ... magnetic field amplitude [μT]

T ... magnetic field duration [s]

From the equation 1.2 flip angle can be determined by magnetic field duration and magnetic field amplitude. B_1 is referred to as a radio frequency (RF) pulse. During the rotation of M_0 towards the transverse plane, M_0 precesses along the z-axis. The precession of M_0 here refers to the precession of all the protons contributing to M_0. After M_0 is flipped by angle α the protons lose their coherence during the precession, and the M_0 disappears in the transverse direction while the M_0 builds up in the longitudinal direction. The relaxation of the longitudinal magnetization component from a higher energy state (non-equilibrium state) to a lower energy state (equilibrium state) is called spin-lattice relaxation. The duration required for longitudinal magnetization to reach $(1 - 1/e)$ of M_0 is called spin-lattice relaxation time (T_1), as described in the equation 1.4 below. Similarly, the relaxation of transverse components of magnetization is called spin-spin relaxation, and the time to reduce transverse magnetization by a factor of e is called spin-spin relaxation time (T_2), as detailed in the equation 1.3 below.

Die approbierte gedruckte Originalversion dieser Diplomarbeit ist an der TU Wien Bibliothek verfügbar
The approved original version of this thesis is available in print at TU Wien Bibliothek.
TU Bibliothek Your knowledge hub WIEN

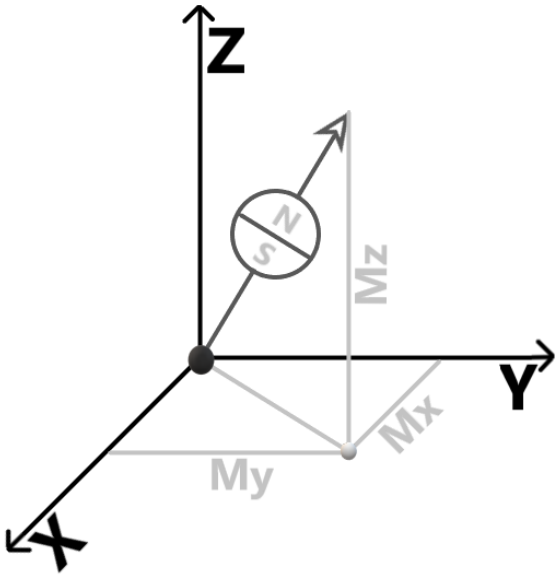

Figure 1.1: The nuclei with longitudinal (M_z) and transverse magnetization (M_{xy}).

$$M_z(t) = M_0 \cdot (1 - e^{\frac{-t}{T_1}}) \tag{1.3}$$

$$M_{xy}(t) = M_{xy,0} \cdot e^{\frac{-t}{T_2}} \tag{1.4}$$

T_2 relaxation here considers only irreversible loss of phase coherence. The T_2^* describes the reversible loss of phase coherence. For example, the inhomogeneity of a magnetic field in a small volume can be another reason for the loss of phase, which is possible to get reversed by magnetic field shimming.

T_2 times are generally shorter than T_1. T_1 and T_2 are dependent on the type of tissues. For example, relaxation times are generally longer in water or cerebrospinal fluid and shorter in lipids.

If a coil is placed on the transverse axis. In that case, the electromagnetic induction

Die approbierte gedruckte Originalversion dieser Diplomarbeit ist an der TU Wien Bibliothek verfügbar
The approved original version of this thesis is available in print at TU Wien Bibliothek.

introduces change in the transverse magnetic field which induces an electric voltage in the coil. This can be further magnified and received in an MR spectrometer. This is NMR signal and it is called Free Induction Decay (FID). The decay of a signal is controlled by T_2. These signals can be measured with the help of a coil and represented as real and imaginary components of complex-valued signals.

Actually/Generally/In current practice/T/the NMR signals in an MR spectrometer consist of signals with different ω and their respective M_0 and T_2*. Fourier transformation separates signals with different ω and analyses them in the frequency domain.

1.1.1 Magnetic Resonance Imaging

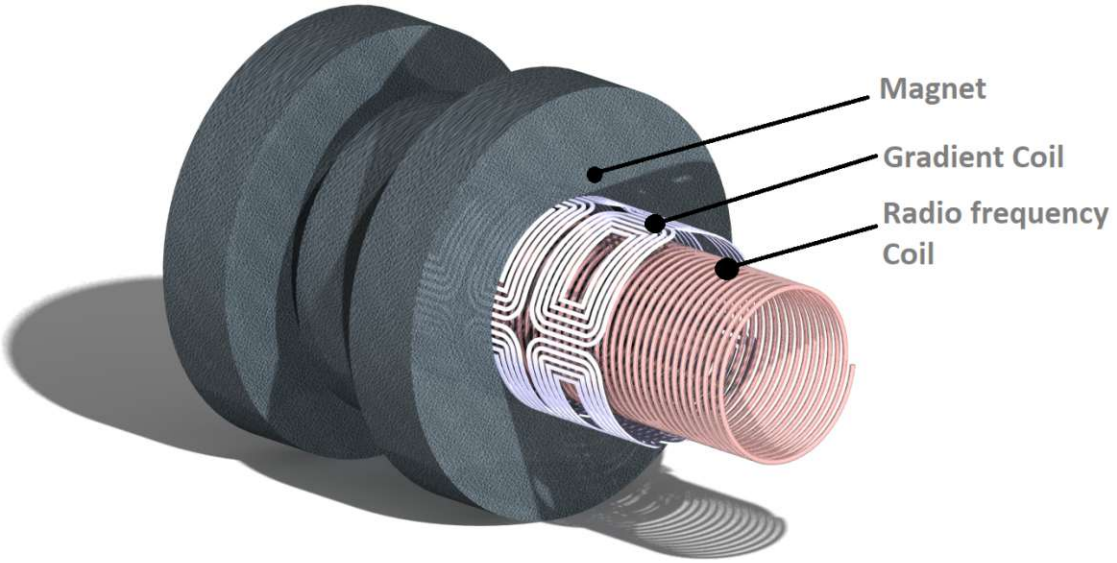

Figure 1.2: Three main parts of Magnetic Resonance Image (MRI) scanner.

MRI generates a spatial illustration of tissues and organs based on their proton density and T1 and T2 relaxation values.

Before considering the imaging part of an MRI, it is essential to understand the basic

Die approbierte gedruckte Originalversion dieser Diplomarbeit ist an der TU Wien Bibliothek verfügbar
The approved original version of this thesis is available in print at TU Wien Bibliothek.

construction parts of MRI scanners. There are three crucial parts in the scanners that we need to know about, as shown in figure 1.2 above. As an outermost scanner part, a large superconducting magnet is responsible for the homogeneous magnetic field (B_0). The gradient coils are placed inside the magnet that localises the radio frequency signals by altering the homogeneous magnetic field inside the scanner in all three directions of 3D space. The loud noise one hears during an MRI scan is produced due to this process. The scanner also contains an RF coil, which sends and receives radio-frequency signals. The signals emitted by the subject during relaxation are called FID signals, are received by the receiver coil. Furthermore, the FID signals are degitised by the analog-to-digital converter (ADC) and are stored for post-processing. RF coils are generally responsible for the reception and transmission of the signals. The RF coil is externally placed on the head as the head coil in our 7T MRSI scanners. Transmission and reception coils are separately built in an external head coil. After figuring out about the production and storage process of the signals, now we move on and learn about how thousands of voxels in 3D space are located to form a well-ordered image.

1.1.2 Signal localization

The magnetic field gradient system with frequency encoding and/or phase encoding is used for localisation. The 3D space is defined by the Cartesian coordinate system x, y, and z as spatial direction. For our interpretation, we use z-direction for slice selection and xy as the in-plane direction of an image. Preliminary slice selection is performed with the help of the z-direction. The gradient constant in the z-direction is considered as follows:

$$G_z = \frac{dB_z}{dz} = constant \tag{1.5}$$

Die approbierte gedruckte Originalversion dieser Diplomarbeit ist an der TU Wien Bibliothek verfügbar
The approved original version of this thesis is available in print at TU Wien Bibliothek.

If we consider B_0 as the homogeneous magnetic field, the position-dependent magnetic field $B(z)$ due to the gradient magnetic field is given by:

$$B(z) = B_0 + z \cdot G_z \tag{1.6}$$

The resonance frequency along z also varies linearly, as seen in the equation 1.9.

$$\omega(z) = \gamma B(z) \tag{1.7}$$

$$\omega(z) = \gamma B_0 + \gamma z \cdot G_z \tag{1.8}$$

$$\omega(z) = w_0 + \gamma z \cdot G_z \tag{1.9}$$

In reference to the above equation, we can use G_z gradient and radiofrequency pulse with $\Delta\omega$ bandwidth as illustrated in the equation 1.10 and figure 1.3 for a selection of a single slice with Δz thickness,. Considering the z-gradient for transversal slices, sagittal and frontal slices can be localised using x-gradient and y-gradient.

$$\Delta z = \frac{\Delta\omega}{\gamma G_z} \tag{1.10}$$

Die approbierte gedruckte Originalversion dieser Diplomarbeit ist an der TU Wien Bibliothek verfügbar
The approved original version of this thesis is available in print at TU Wien Bibliothek.
TU Bibliothek Your knowledge hub WIEN

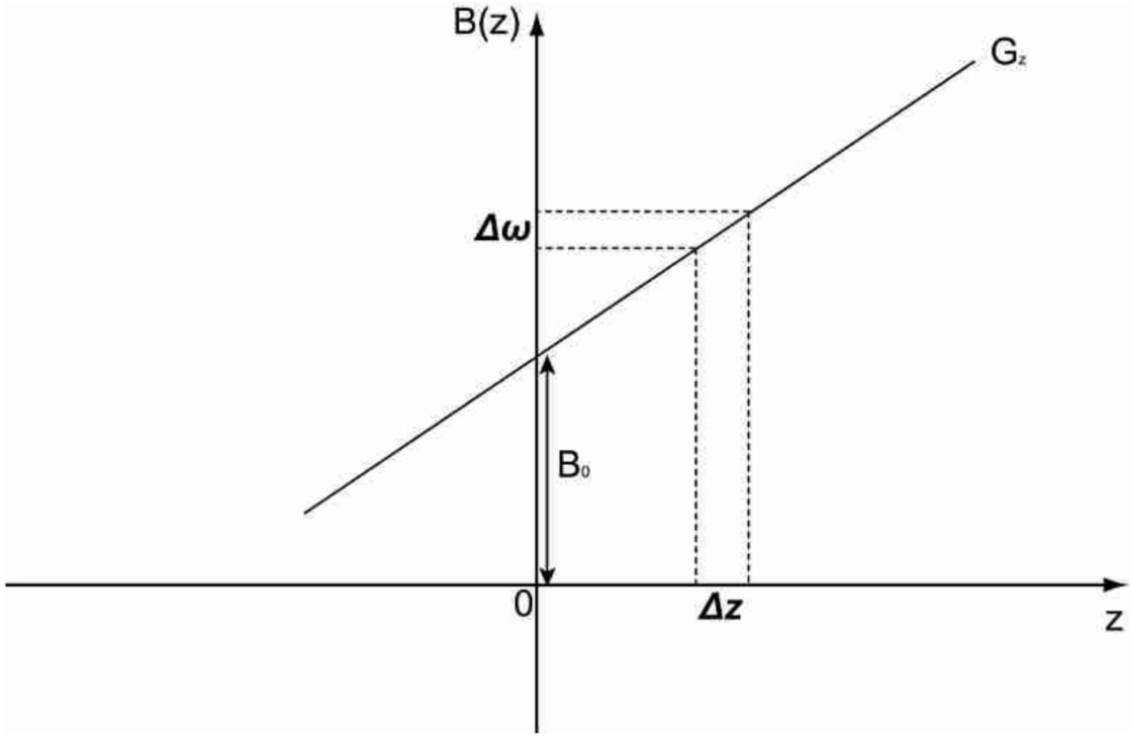

Figure 1.3: The magnetic field gradient approach for a slice selection in the z-direction. From *Accelerated high-resolution 3D MRSI in the brain at 7 T* by *Gilbert Hangel*, 2015, PhD thesis, Medical University of Vienna. Creative Commons Attribution 4.0 License. (Hangel, 2015)

After the position of a slice is localised, it is time for the x and y in-plane localisation. A frequency-encoding gradient (G_F) is used to localise another dimension x. The x dimension is considered to be fixed left to the right direction as shown in the figure 1.4 below. The previous magnetic gradient does not affect in-slice localisation. G_F is perpendicular to the direction of the slice-selection magnetic gradient. The Larmor frequency is varied along the x-direction by G_f, as given in the equation 1.11.

$$w(x) = w_0 + \gamma x \cdot G_F \tag{1.11}$$

Die approbierte gedruckte Originalversion dieser Diplomarbeit ist an der TU Wien Bibliothek verfügbar
The approved original version of this thesis is available in print at TU Wien Bibliothek.
TU Bibliothek Your knowledge hub WIEN

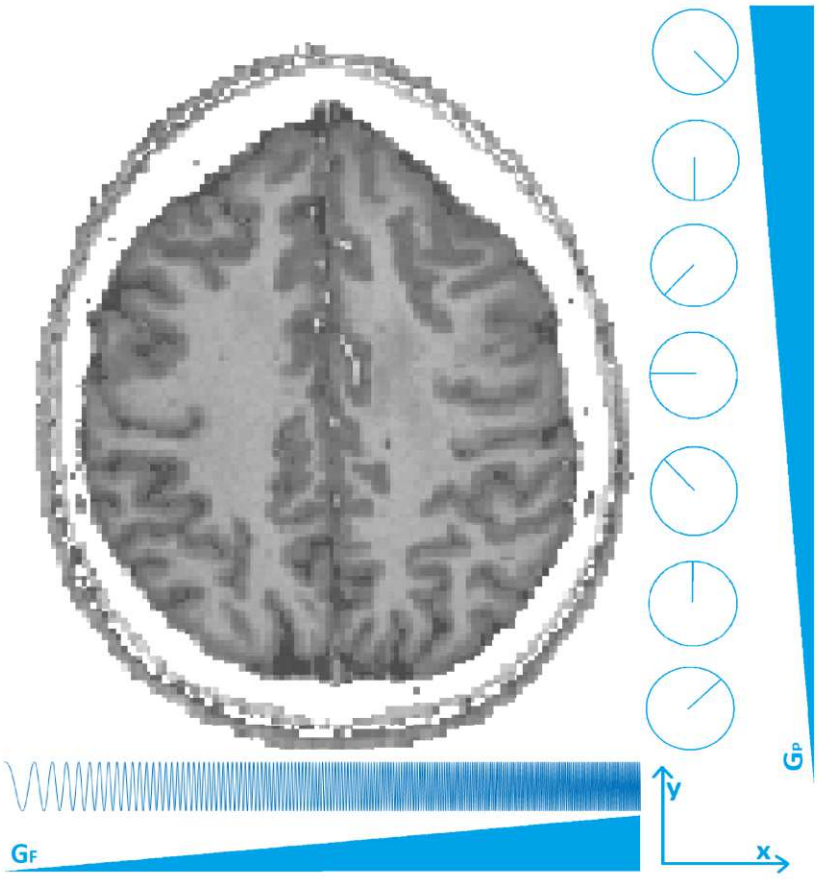

Figure 1.4: The figure shows the how the frequency-gradient (G_F) and phase-gradient (G_P) works during in-plane localization.

A signal from a selected slice consists of signals for all the locations in the slice. It is exactly where Fourier transformation (FT) comes into play; as an output of Fourier Transform, we get separated signals with different frequencies $\omega(X)$. Again, each signal corresponds to each position perpendicular to the x-direction accompanying the frequency $\omega(X)$ as seen in the figure 1.4. Lastly, we need localisation along the y-axis, obtained by phase-encoding gradient (G_P) applied perpendicular to both magnetic gradient and G_F. The equation for Larmor frequency is quite similar to

Die approbierte gedruckte Originalversion dieser Diplomarbeit ist an der TU Wien Bibliothek verfügbar
The approved original version of this thesis is available in print at TU Wien Bibliothek.
TU Bibliothek Your knowledge hub WIEN

earlier as seen in equation 1.12.

$$\omega(x) = \omega_0 + \gamma y \cdot G_P \tag{1.12}$$

We cannot extract the signal for each point as we previously did in the case of x-direction. A measurement is performed with different phase encoding for the signals from every point. The number of measurements equals the number of points in the phase encoding direction. The time between consecutive RF pulses is called repetition time (TR). The duration of repetition time determines longitudinal magnetisation recovered between each radio-frequency pulse. The dimension of the slice matrix and TR primarily influences the total measurement time. The total measurement time can be determined using the TR :

$$Total\ measurement\ time = TR \times Number\ of\ phaseencodingsteps \tag{1.13}$$

Reducing TR means triggering nuclei to excitation before completely relaxing to an equilibrium state. The shift in phase along the y-direction for each measurement is given by an equation 1.14 where t is an active gradient time.

$$\Delta\phi(y) = \Delta\omega_0(y)t = (\gamma y \cdot G_P)t \tag{1.14}$$

In brief, magnetic field, frequency, and phase gradients are used for the 3D positional localisation of signals.

Die approbierte gedruckte Originalversion dieser Diplomarbeit ist an der TU Wien Bibliothek verfügbar
The approved original version of this thesis is available in print at TU Wien Bibliothek.
TU Bibliothek Your knowledge hub WIEN

1.1.3 Image acquisition

The signals acquired by phase and frequency encoding are now stored in an image matrix. This image matrix is not the image where we see the anatomical structure of the image (see the right image of the figure 1.5). It looks like the one on the left image of the figure1.5, known as k-space. Each point in k-space represents a spatial frequency, i.e. the periodicity of brightness variation of the image. It is essential to understand that each point in k-space does not directly correspond to a pixel or voxel in image space. Instead, each point is a signal with collective information about the whole image space.

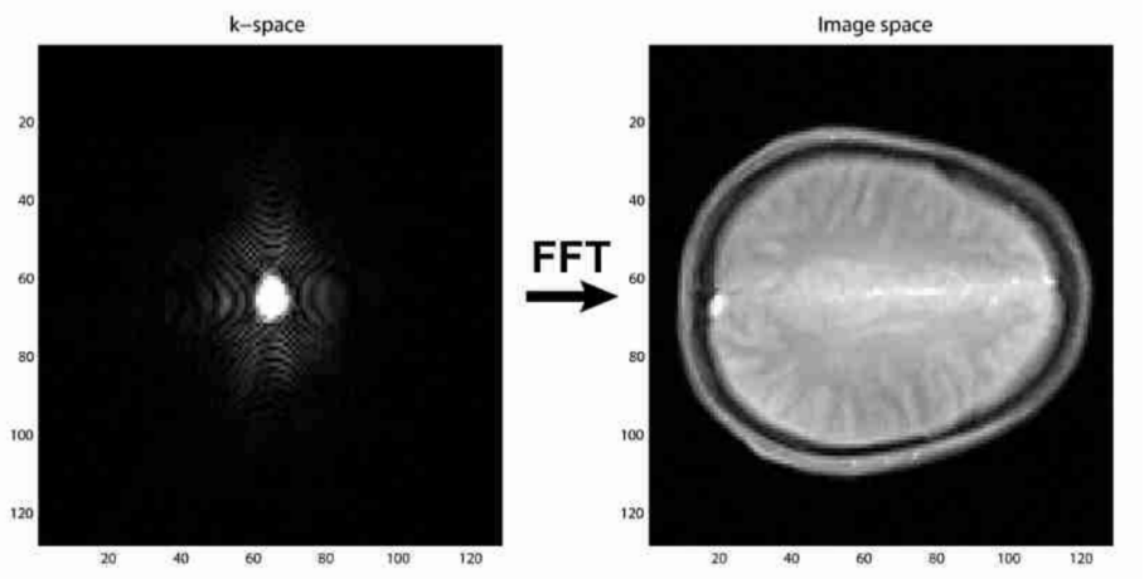

Figure 1.5: Fourier transformation from k-space to the image space. Source: *Accelerated high-resolution 3D MRSI in the brain at 7 T* by *Gilbert Hangel*, 2015, PhD thesis, Medical University of Vienna. Creative Commons Attribution 4.0 License. (Hangel, 2015)

Those signals are made up of imaginary and real parts. The information in those

Die approbierte gedruckte Originalversion dieser Diplomarbeit ist an der TU Wien Bibliothek verfügbar
The approved original version of this thesis is available in print at TU Wien Bibliothek.
TU Bibliothek Your knowledge hub WIEN

signals varies according to their location and brightness. The brighter points in the k-space, mostly located at the central region, are the signals with a lower frequency and relatively more information. The darker points on the borders of the k-space are with higher frequency and relatively less information. FT of points in k-space results in anatomical MRI image. It is unnecessary to transform all the points in k-space to get an anatomical image. However, increasing the number of points in k-space results ensure a better result. Phase encoding techniques to acquire data for K-space are time-consuming. Other methods have also been introduced to avoid long acquisitions, where data from the whole 2D k-space is collected in single RF excitation. Echo-planar Imaging (EPI) is a method where one (single-shot EPI) or few (multi-shot EPI) zig-zag lines are used instead of straight lines to acquire complete k-space information. Non-Cartesian trajectories like circular trajectories are also used in the process. The MRSI images used in this thesis have also been acquired using in-plane rapid concentric ring trajectory (CRT) (Hingerl et al., 2020), which uses a set of uniformly distributed concentric rings to sample 2D k-space and phase encoding for in-plane sampling as shown in the figure 1.9 below.

1.1.4 Image quality

We need to consider the image quality for the imaging method. Field of view (FOV), image resolution, and signal-to-noise ratio (SNR) are the factors to be taken care of for the quality of an image. The FOV of MRI is given by equation 1.15.

$$FOV = \frac{2\pi}{\gamma G \Delta t} = \frac{1}{\Delta k} \tag{1.15}$$

According to the equation 1.15, FOV is inversely proportional to the Δk distance

Die approbierte gedruckte Originalversion dieser Diplomarbeit ist an der TU Wien Bibliothek verfügbar
The approved original version of this thesis is available in print at TU Wien Bibliothek.
TU Bibliothek Your knowledge hub WIEN

between points in k-space. To increase FOV, we need to reduce Δk. Δk is given by $\Delta k = \gamma G \Delta t$. Likewise, the resolution is given as in the equation 1.16.

$$\Delta V = \frac{FOV_x}{N_x} \frac{FOV_y}{N_y} \frac{FOV_z}{N_z} \tag{1.16}$$

where N_i is dimention of k in i dimension.

The SNR, as its name indicates, is a parameter for the amount of information compared to noise. The SNR is linearly dependent on B_0. Relaxation time also plays a role in determining SNR. The relation of SNR is given as in the equation 1.17:

$$SNR \infty B_0 \sqrt{\frac{T_2}{T_1}} \tag{1.17}$$

1.1.5 Pulse sequence

The pulse sequence adjusts the localisation of the MRI. The pulse sequence is also responsible for the weighting and contrast of MRI with adjustment of excitation, encoding, and sequence timing. Spin echo (SE) is a simple pulse sequence that helps understand the importance of pulse sequence. As discussed, after a single RF pulse, the net longitudinal magnetisation flips 90° to net transversal magnetisation, and FID occurs. However, suppose we apply two successive RF pulses. In that case, phase coherence of protons increases after the second 180° pulse for the time duration equal to the duration between two RF pulses and again decays, as shown in the figure 1.6. The advantage of SE is that the T_2^* relaxation after the first impulse is very short due to the inhomogeneous static magnetic field, allowing very little localisation scheme time. Whereas with SE, we cancel out the effect of inhomogeneity, resulting in slower decay and gaining some time between the first excitation and time of echo, known as echo time (TE). TE can be utilised for localisation schemes and create an anti-phase

Die approbierte gedruckte Originalversion dieser Diplomarbeit ist an der TU Wien Bibliothek verfügbar
The approved original version of this thesis is available in print at TU Wien Bibliothek.
TU Bibliothek Your knowledge hub WIEN

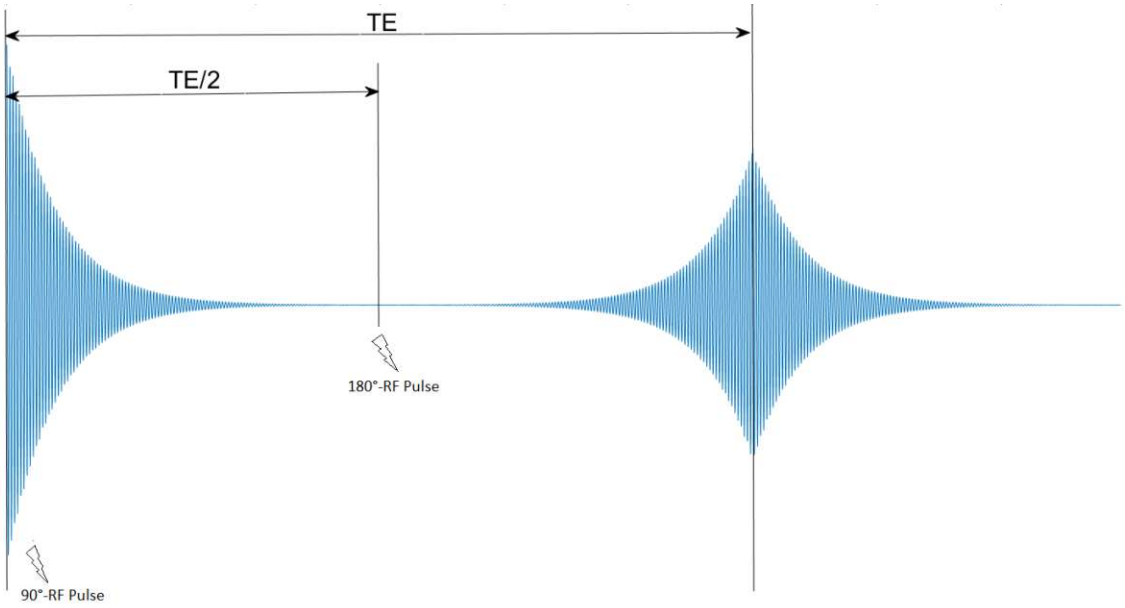

Figure 1.6: Spin Echo (SE) signal where the Free Induction occurs after 90 °pulse and the 180 °pulse at the time equals half of Excitation Time (TE) results into SE at TE.

pulse to contain contamination signals. The SE pulse sequence can be seen in figure 1.7.

1.1.6 Magnetic Resonance Spectroscopy (MRS)

MRSI is used to get information about the concentration of neurochemical molecules in the tissues. This chemical composition mainly consists of neurochemicals in the brain that are also known as metabolites. The signals from MRI scans include the frequency spectrum conveying the composition of water, fat, and metabolites. By exclusion of dominating signals from water and lipid, we reach out to the signals of metabolites. Separation of the signals for individual metabolites can be achieved through their characteristic difference in resonance frequency. This thesis deals with

Die approbierte gedruckte Originalversion dieser Diplomarbeit ist an der TU Wien Bibliothek verfügbar
The approved original version of this thesis is available in print at TU Wien Bibliothek.
TU Bibliothek Your knowledge hub WIEN

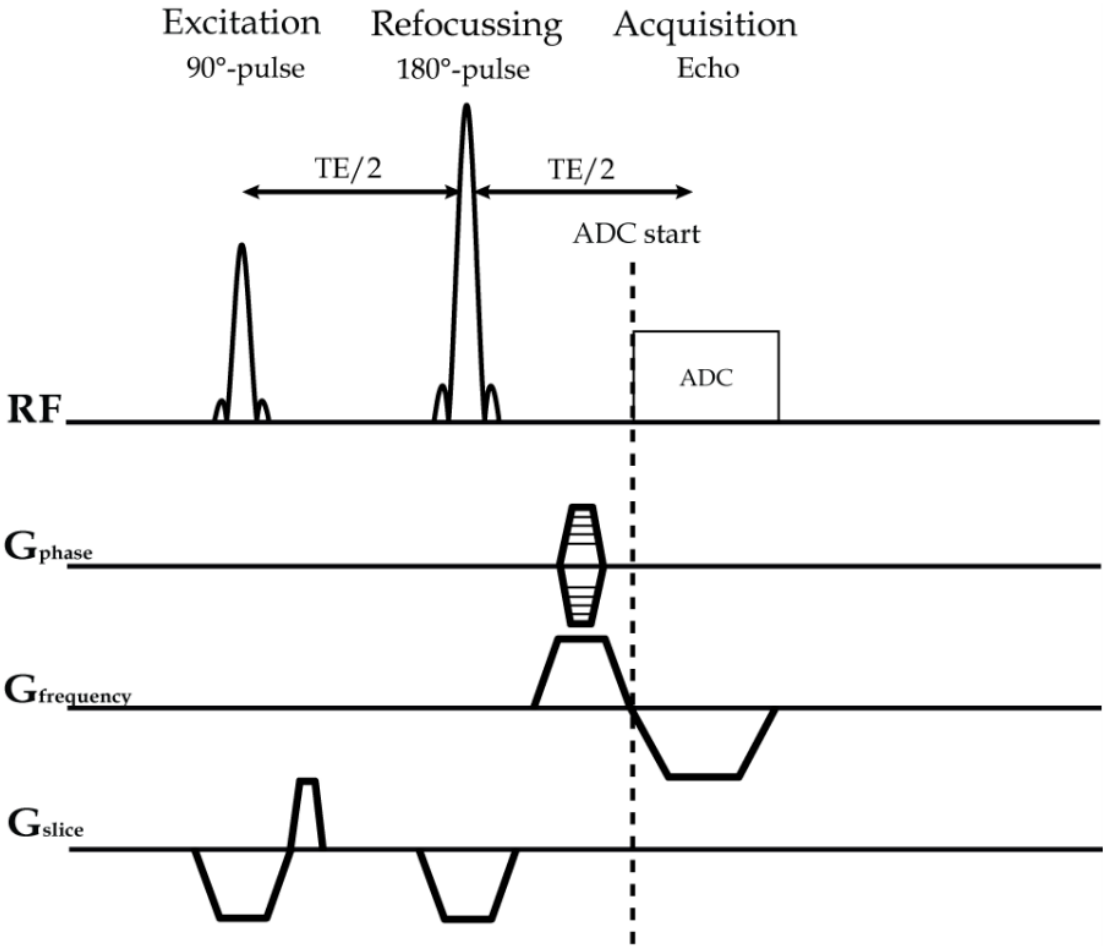

Figure 1.7: Spin echo (SE) pulse sequence. Source: *Accelerated high-resolution 3D MRSI in the brain at 7 T* by *Gilbert Hangel*, 2015, PhD thesis, Medical University of Vienna. Creative Commons Attribution 4.0 License. (Hangel, 2015)

Die approbierte gedruckte Originalversion dieser Diplomarbeit ist an der TU Wien Bibliothek verfügbar
The approved original version of this thesis is available in print at TU Wien Bibliothek.

the MRSI images of the brain while it is generally also used in the muscles, the prostate, the liver, and breasts. The data used in this thesis mainly comprise the MRS image of brains. So, it is essential to understand how those images are obtained.

The fundamental idea behind MRS is a chemical shift. The difference in resonance frequency between two otherwise identical nuclei from different environments is known as a chemical shift. The resonance frequency of a particular nucleus is not determined by the external magnetic field but rather by the local magnetic field experienced by the nucleus. Two factors determine the resonance frequency of each nucleus. Namely the type of molecule, and its regional position in the molecule. Thus, a chemical shift can provide information about molecular composition. The local magnetic field experienced by a nucleus is reduced from the external magnetic field by the means of an induced magnetic field that is produced by the electrons circulating the nucleus, which is known as electronic shielding. The outer electrons shield the nucleus from the full effect of external magnetic fields with a dimensionless shielding factor denoted by σ.

$$\vec{B}_{loc} = B_0 - B_{ind} = \vec{B}_0(1 - \sigma) \tag{1.18}$$

The relation between Larmor frequency and the magnetic field is defined as:

$$\omega_0 = \gamma \vec{B}_0 \tag{1.19}$$

In the equation above we observe a Larmor frequency is proportional to the magnetic

Die approbierte gedruckte Originalversion dieser Diplomarbeit ist an der TU Wien Bibliothek verfügbar
The approved original version of this thesis is available in print at TU Wien Bibliothek.
TU Bibliothek Your knowledge hub WIEN

field. With the magnetic field defined in the equation 1.18, we get:

$$\omega_0 = \gamma \vec{B}_0(1 - \sigma) \tag{1.20}$$

Chemical shift (δ) defined by the International Union of Physicists and Chemists (IUPAC) in 2001, is more commonly used than σ for the shielding effect. It is defined as:

$$\delta = \frac{\omega - \omega_{ref}}{\omega_{ref}} \cdot 10^6 \tag{1.21}$$

Where ω is resonance frequency and ω_{ref} is the frequency of reference compound which is tetramethylsilane in phantoms MRS whereas, water(4.7 ppm), N-acetyl-aspartate(NAA, two ppm), or other external references for *in vivo* MRS. Because of its small magnitude, the chemical shift (*delta*) is dimensionless and predominantly expressed as parts per million (ppm). ppm can describe the chemical shifts as independent of field strength. Let us consider two nuclei with a ten ppm difference in chemical shift. The Larmor reference frequency of 3 Tesla (3T) is 128 MHz, and that of 7T is 298 MHz. The difference in resonance frequency between those two nuclei would be $128\ MHz \times 10\ ppm = 1280\ Hz$ in 3T and $298\ MHz \times 10\ ppm = 2980\ Hz$ in 7T.

The quality of MRS is mainly dependent on spectral quantification, which is principally assured using SNR, the full width at half maximum (FWHM) of resonances, and the Cramér–Rao lower bounds (CRLBs) of metabolites. CRLB indicates MRS quantification quality based on mean errors during spectral fitting based on measurement data. FWHM denotes the line width of the spectrum resonance peak at half of its maximum height. FWHM is inversely proportional to T_2^*. A decrease in FWHM

Die approbierte gedruckte Originalversion dieser Diplomarbeit ist an der TU Wien Bibliothek verfügbar
The approved original version of this thesis is available in print at TU Wien Bibliothek.

results in an increase in the spectral resolution of MRSI. SNR determines the quality of measurement. The lower SNR indicates unreliable MRS quantification.
MRS has two main applications: Single voxel spectroscopy (SVS) and MRSI. SVS is a comparatively simple and fast way of MRS data acquisition. SVS localisation uses three successive gradient-based RF pulses in three orthogonal planes with possible additional outer volume suppression pulses. The intersection of those planes defines the volume of interest (VOI), defined as a voxel. The signal received from this single voxel is used to acquire spectrum. FT of acquired time-domain signal results in a spectrum in SVS. SVS, compared to MRSI, is fast and easy, with better spectral resolution and higher SNR. In comparison, MRSI has acquired multiple molecular components simultaneously (Hangel, 2015). The non-limited VOI in MRSI makes it significant for inhomogeneous lesions and other diseases like Epilepsy (Pan et al., 2013), Adenoleukodystrophy (Ratai et al., 2008), Alzheimer, Parkinson, Prostate (Trattnig et al., 2016)and Multiple Sclerosis (MS) (Srinivasan et al., 2010). Moreover, Hangel (2015) has also demonstrated the significance of MRSI in measuring the tumor near the cranium. //

1.1.7 Magnetic Resonance Spectroscopy Imaging (MRSI)

MRSI deals with the chemical composition of tissues. In our context, MRI is used to obtain the tumor structure and MRSI for information about metabolic activity in the tumor. MRSI is also known as Chemical Shift Imaging (CSI).

MRSI localisation is necessarily different from MRI as G_F is used for chemical shift differentiation between different metabolites. The most straightforward idea for localisation of MRSI could be using G_P on both dimensions of k-space point by

Die approbierte gedruckte Originalversion dieser Diplomarbeit ist an der TU Wien Bibliothek verfügbar
The approved original version of this thesis is available in print at TU Wien Bibliothek.
TU Bibliothek Your knowledge hub WIEN

point using FID. The pulse sequence shown in figure 1.8 is used for data acquisition.

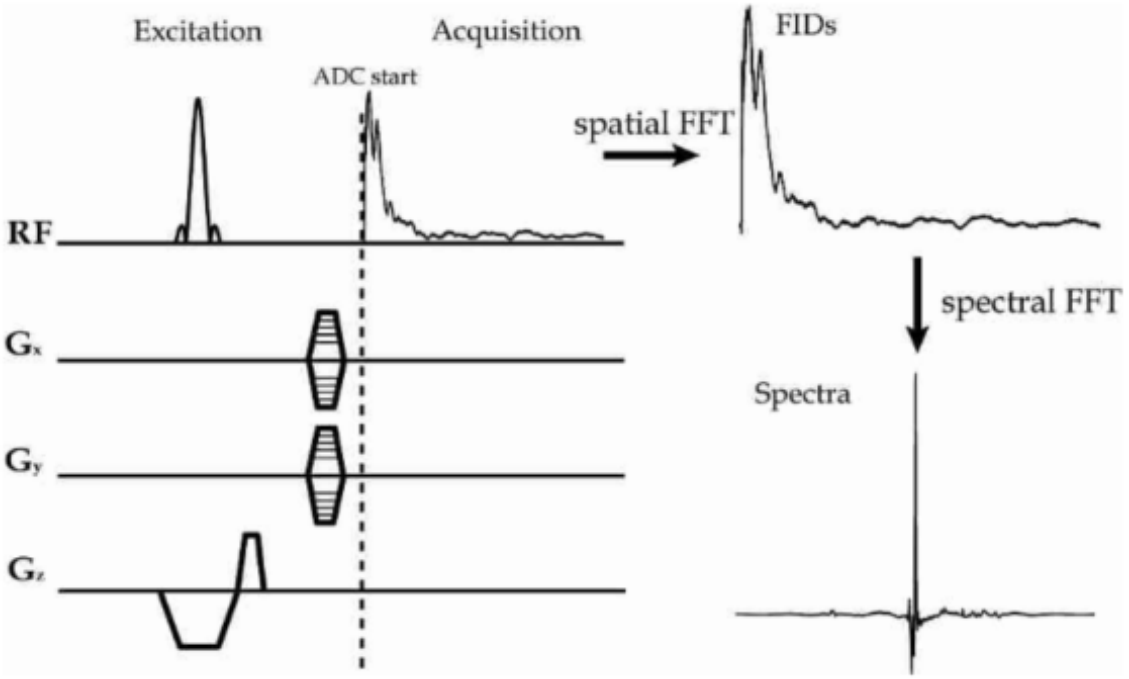

Figure 1.8: MRSI pulse sequence without a spin echo. Further, on the right, two successive fast Fourier transformations were to obtain voxel-specific FIDs and spectrum. Source: *Accelerated high-resolution 3D MRSI in the brain at 7 T* by *Gilbert Hangel*, 2015, PhD thesis, Medical University of Vienna. Creative Commons Attribution 4.0 License. (Hangel, 2015)

The phase shift (1.14PS) used in MRSI is spatially dependent, which must be considered during the post-processing of k-space. Multiple spectral data of the whole FOV in k-space are encoded in a time-domain signal. FT of spatial dependent time-domain signal helps to acquire voxel-specific FIDs. Further FT results voxel-specific spectra. So, FT plays a vital role in spectrum acquisition, but it comes with a cost. The spectrum of a voxel is influenced by the ripples of the neighbouring spectrum, which is described as the point spread function (PSF)(Skoch et al., 2008). PSF

Die approbierte gedruckte Originalversion dieser Diplomarbeit ist an der TU Wien Bibliothek verfügbar
The approved original version of this thesis is available in print at TU Wien Bibliothek.
TU Bibliothek Your knowledge hub WIEN

is a weighting function describing the contamination of neighbouring voxels to a particular voxel. To combat this effect, the spherical region in k-space for data sampling is defined, and signals in border regions are defined as zero (A. A. Maudsley et al., 1994; von Kienlin & Mejia, 1991). This method is applicable since the short-wavelength signals on the border region of k-space contain information about shape, which is less crucial for MRSI. Selection of spherical sampling in k-space results in a reduction of measurement time. Likewise, a Hamming filter (von Kienlin & Mejia, 1991) can increase amplitude in the centre of the k-space and reduce amplitude at the edges. It increases the width of the central peak, sinking the spatial resolution. Considering all these factors, the FID MRSI with concentric ring trajectories (Hingerl et al., 2020) helps to reduce scan times with better spatial resolution and SNR to perform 3-dimensional encoding of ellipsoidal k-space and phase encoding for in-plane encoding helps to reduce scan times with better spatial resolution and SNR. The pulse sequence for FID MRSI with CRT includes iMUSICAL (P. Moser et al., 2019; Strasser et al., 2013) with 5°excitation pulse followed by WET for water suppression and 3D-CRT for data acquisition as shown in the figure 1.9. This method was used for the data acquisition of MRSI images used in this thesis.

Die approbierte gedruckte Originalversion dieser Diplomarbeit ist an der TU Wien Bibliothek verfügbar
The approved original version of this thesis is available in print at TU Wien Bibliothek.

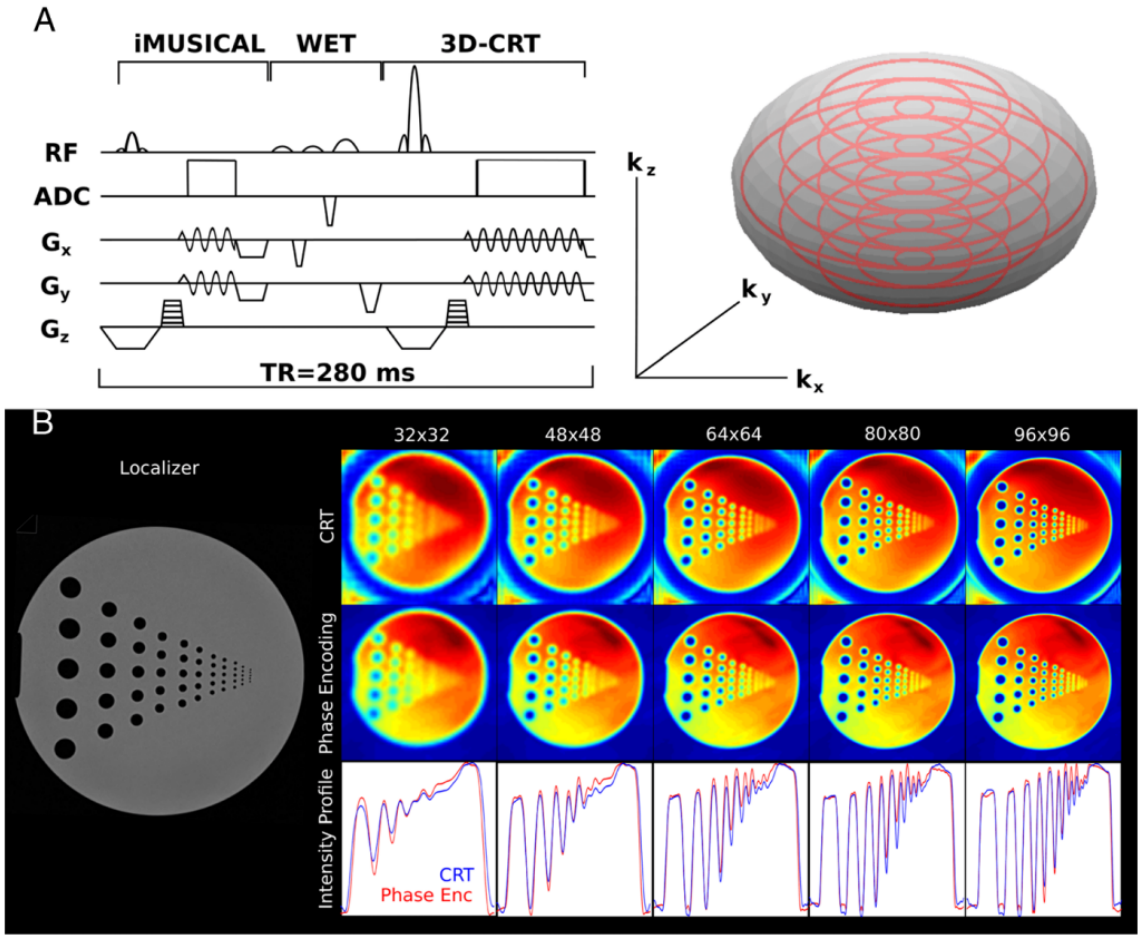

Figure 1.9: A: Pulse sequence for FID MRSI with in-plane CRT encoding and through-plane 3D ellipsoidal encoding.
B: Magnitude image and intensity image of silicon oil-filled phantom with five different matrix sizes ((32 x 32, 48 x 48, 64 x 64, 80 x 80, 96 x 96), all with a thickness of 10 mm interpolated to double matrix size for visualisation. The structures are 1-10 mm and 15mm in diameter. Source: *Clinical High-Resolution 3D-MR Spectroscopic Imaging of the Human Brain at 7 T* by *Lukas Hingerl et al.*, 2020, Wolters Kluwer Health, Inc., license number 4933021001140 (Hingerl et al., 2020)

Point-resolved Spectroscopy (PRESS) with first 90° and two successive 180° flip angles as in figure 1.10 and Stimulated Echo Acquisition Mode (STEAM) with all

Die approbierte gedruckte Originalversion dieser Diplomarbeit ist an der TU Wien Bibliothek verfügbar
The approved original version of this thesis is available in print at TU Wien Bibliothek.

three 90° flip angles (Moonen et al., 1989) shown in the figure 1.10 are popular sequences for MRS.

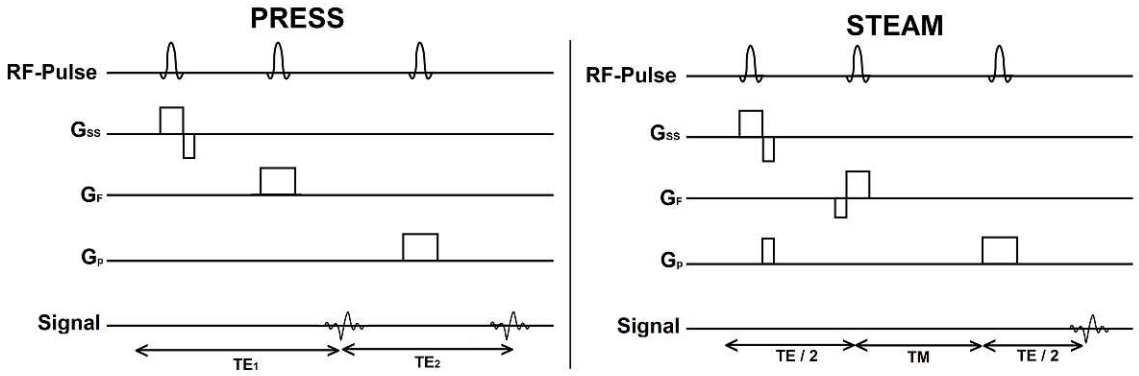

Figure 1.10: The figure on the left shows the pulse sequence of Point-resolved Spectroscopy (PRESS), and on the right is the pulse sequence of Stimulated Echo Acquisition Mode (STEAM)

The PRESS sequence offers a better SNR because the amplitude of this SE is twice that of STEAM. In comparison, STEAM helps achieve lower TE than PRESS (Moonen et al., 1989).

1.1.8 7 Tesla Magnetic Resonance Spectroscopy Imaging (7T MRSI)

Due to its improvement in mapping multiple metabolites, SNR, reproducibility, and spectral resolution (Bogner et al., 2012; Trattnig et al., 2016) 7T MRSI is well-known as High-Resolution 3D MRSI (Hangel, 2015). Although many benefits of 7T MRSI have been explored (E. Moser et al., 2012; Posse et al., 2013) since the beginning

Die approbierte gedruckte Originalversion dieser Diplomarbeit ist an der TU Wien Bibliothek verfügbar
The approved original version of this thesis is available in print at TU Wien Bibliothek.
TU Bibliothek Your knowledge hub WIEN

of the current millennium, there are still many scopes of improvement in shimming techniques, parallel imaging, pulse sequence scheme, and hardware of MRI scanner. Nevertheless, 7T MRS makes exploring the concentration of extended variation of neurochemical molecules, commonly called metabolites, possible.

1.1.9 Water and lipid suppression

Before we discuss metabolites, the subject of great concern is water and lipid in the brain. The water concentration in the brain is 10,000 times higher than the one of metabolites like NAA, Cho, and CR. The peak of the water spectrum thus dominates the MS, and other metabolites are undetectable. Therefore, the suppression of water peaks makes the analysis of metabolite peaks easier. Chemical Shift Selective (CHESS) (Haase et al., 1985) is widely popular for water suppression in MR. CHESS consists of three successive RF pulses, each followed by slice selection, phase, and frequency gradient, as shown in figure 1.11.

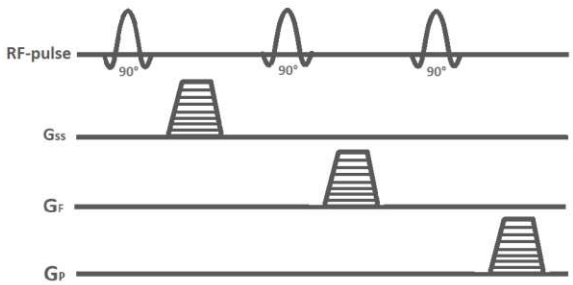

Figure 1.11: Chemical Shift Selective Saturation (CHESS) pulse sequence used for water suppression which consists of three 90 °RF-pulses each followed by slice-selection with slice selection gradient ($G_s s$), frequency gradient (G_F) and phase gradient (G_P)

Water suppression Enhanced through T1 effects (WET), Suppression of Water with Adiabatic-Modulated Pulses (SWAMP), Multiple Optimizations Insensi-

Die approbierte gedruckte Originalversion dieser Diplomarbeit ist an der TU Wien Bibliothek verfügbar
The approved original version of this thesis is available in print at TU Wien Bibliothek.

tive Suppression Train (MOIST), and Variable Power radiofrequency pulses with Optimised Relaxation delays (VAPOR) are some modern variants of CHESS. 7T optimised 35ms WET suppression with three pulses (Hangel et al., 2018) sequence is used before localisation in our measurement, as shown in the figure 1.9. WET is derived by analysing longitudinal magnetisation over T_1 and B_1 ranges of interest using Bloch equation (Ogg et al., 1994). It uses three RF pulses with numerically optimised flip angles.

Trans-cranial lipids in the brain are made up of adipose tissues. Adipose tissue is composed of free fatty acids and long-chain triglycerides. The problem in these lipids lies in the resonance frequency of adipose tissues being 0.9-1.4 ppm. The contamination of side lobes spectra from lipid tissues is observed in the metabolites like lactate with a resonance frequency of 1.3 ppm, close to that of lipid, due to the PSF effect. In our case, it is NAA.

Outer volume suppression (OVS) is a commonly practised lipid suppression method. As shown in the figure 1.12 below, the saturation bands are placed over the lipid-containing regions to avoid signals from those regions. OVS does not only remove lipid voxels but other non-lipid voxels as well. The lipid signals can also be removed during the image post-processing to optimise the measurement time. In the measurement process used in this thesis, L2-regularization was included in image post-processing for lipid removal.

After avoiding the water and lipid spectrum, concentrations of different metabolites in the brain are detectable, as in the figure 1.13.

Die approbierte gedruckte Originalversion dieser Diplomarbeit ist an der TU Wien Bibliothek verfügbar
The approved original version of this thesis is available in print at TU Wien Bibliothek.

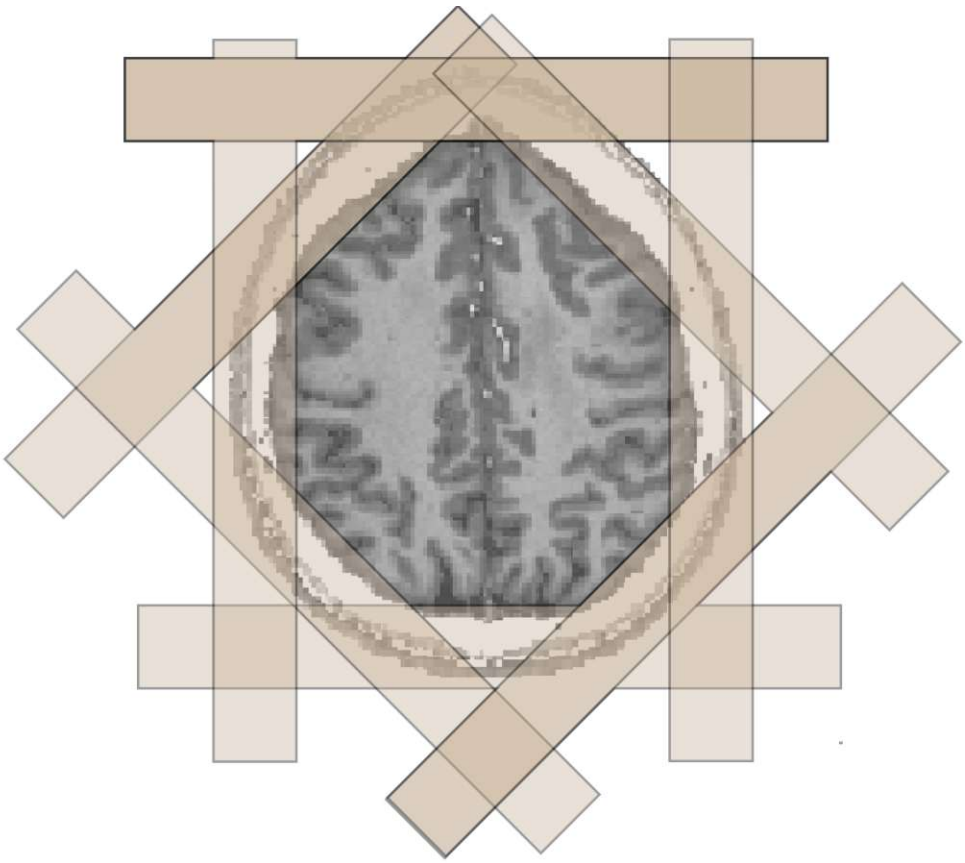

Figure 1.12: The outer volume suppression (OVS) for lipid suppression.

Die approbierte gedruckte Originalversion dieser Diplomarbeit ist an der TU Wien Bibliothek verfügbar
The approved original version of this thesis is available in print at TU Wien Bibliothek.

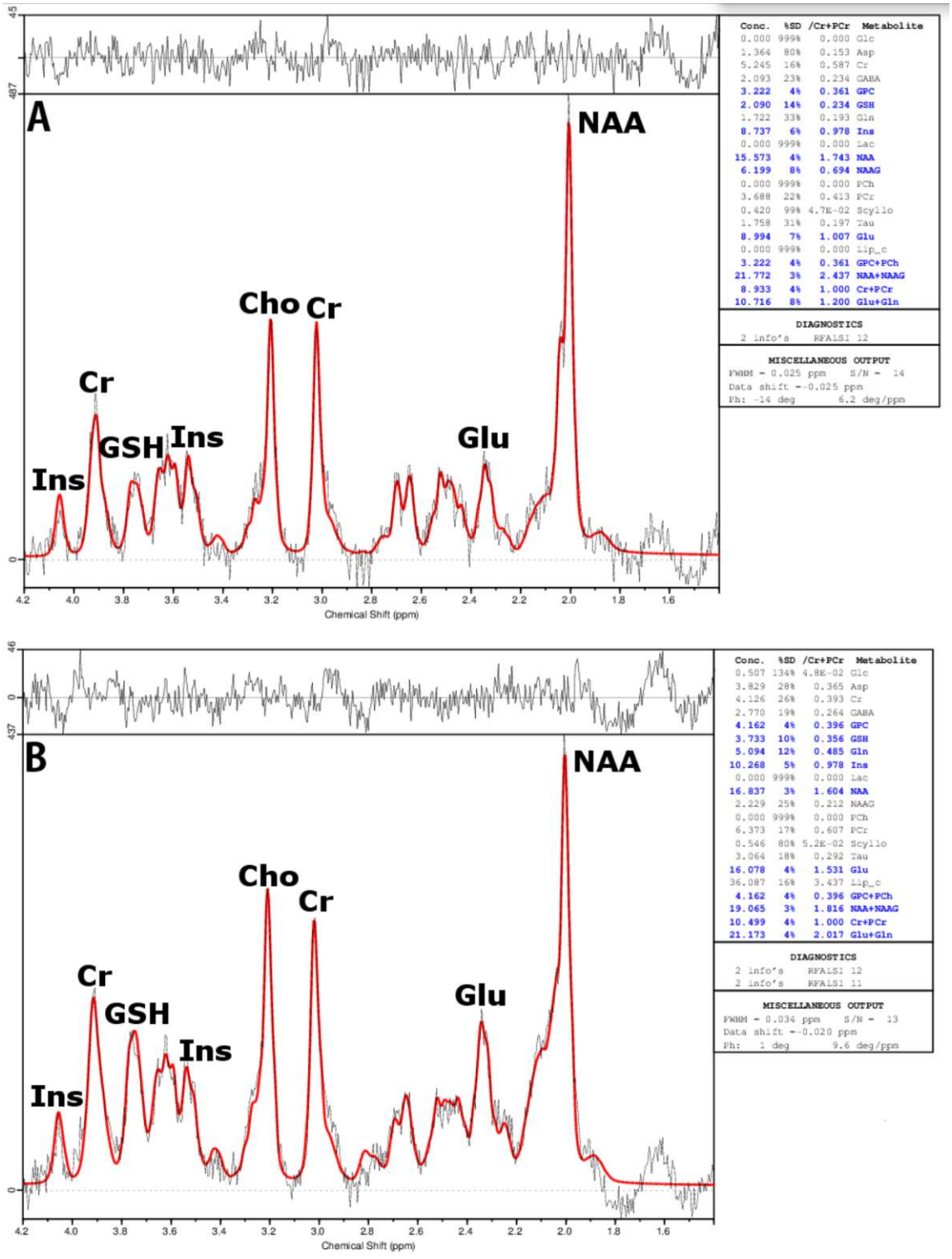

Figure 1.13: Metabolites spectrum in white matter(WM) and grey matter (GM) of the brain. Source: *Accelerated high-resolution 3D MRSI in the brain at 7 T* by *Gilbert Hangel*, 2015, PhD thesis, Medical University of Vienna. Creative Commons Attribution 4.0 License. (Hangel, 2015)

Die approbierte gedruckte Originalversion dieser Diplomarbeit ist an der TU Wien Bibliothek verfügbar
The approved original version of this thesis is available in print at TU Wien Bibliothek.

This thesis deals with some of the essential metabolites in the brain (De Graaf, 2019; Hangel, 2015). Metabolites crucial for this study are described in the following pages. The chemical structures of the following metabolites were drawn using ChemDoodle (iChemLabs, n.d.).

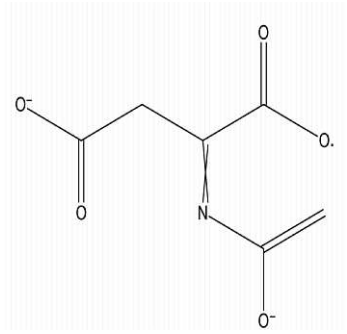

N-acetyl aspartate (NAA) is the tallest peak with a resonance frequency of 2.01 ppm. Since they are mainly found in neurons, declination of NAA is seen in neuron-destructive diseases like epilepsy, MS, tumor, stroke, and dementia and is absent in metastases and meningiomas.

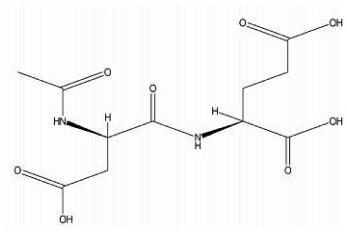

N-acetyl aspartyl Glutamate (NAAG) resonates at 2.04ppm, which is very close to the resonance frequency of NAA. That is why NAAG is difficult to detect and requires a highly homogenous magnetic field for its detection. Mostly, NAA and NAAG are summed up for estimating NAA-containing molecules. NAAG is not uniformly distributed in the brain. The actual role of NAAG remains unclear.

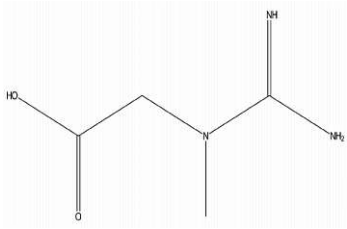

Creatine (Cr) with resonance frequencies of 3.03 and 3.91 ppm includes both Cr and Phosphocreatine (PCr) summarised as total Creatine (tCr). Cr is produced in the liver and takes part in energy metabolism. They are relatively constant in a healthy brain, decrease with brain diseases, and vanish in metastases.

Die approbierte gedruckte Originalversion dieser Diplomarbeit ist an der TU Wien Bibliothek verfügbar
The approved original version of this thesis is available in print at TU Wien Bibliothek.

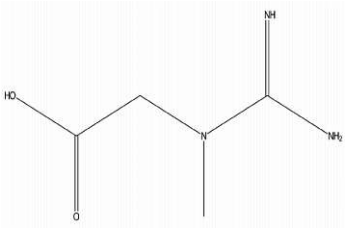

Choline (Cho) is another abundant metabolite with resonances at 3.19 ppm with an affiliation of phosphorylcholine and glycerophosphocholine. As they are a major component of cell membranes. Due to this, an increase in Cho content is observed in ischemia, demyelination, tumors (mainly during malignancy), and infections.

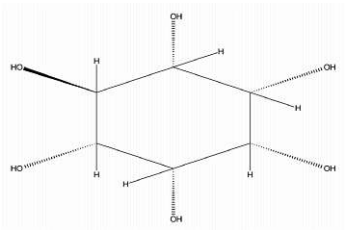

Inositole (Ins) is a metabolite with a resonance frequency of 4.05 ppm. it is believed to be decreased with ischemia, neoplasm, and demyelination.

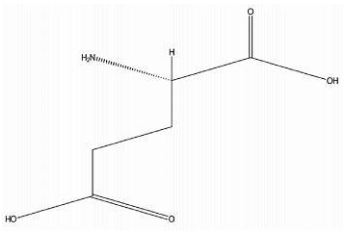

Glutamate (Glu) is a neuron-released major excitatory neurotransmitter with resonances at 3.75, 2.33, 2.04 ppm, and more. It synthesises glutathione and produces γ - Aminobutyric acid (GABA). Astrocytes convert Glu to glutamine (Gln), and Gln is again reprocessed to Glu by neurons. Elevation of Glu is observed during acute brain diseases.

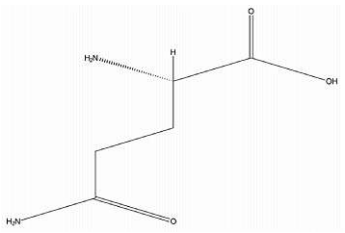

Glutamin (Gln) being structurally similar to Glu resonates at 6.8 and 1.5ppm. It is mainly located in the astroglia and plays a vital role in intermediary metabolism (De Graaf, 2019).

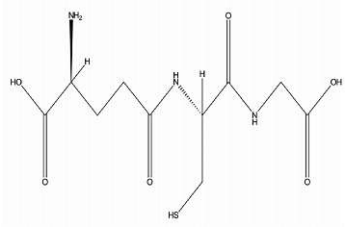

Gluthathione (GSH) with resonance frequency 3.77 and many more is responsible for maintaining red blood cells and transporting amino acids.

Die approbierte gedruckte Originalversion dieser Diplomarbeit ist an der TU Wien Bibliothek verfügbar
The approved original version of this thesis is available in print at TU Wien Bibliothek.

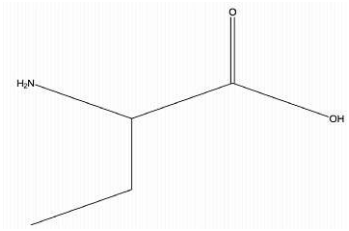

γ **-Aminobutyric acid (GABA)**, the main inhibitory transmitter, resonates at 3.01 and 1.89 ppm. They are resolved by spectral editing, a special MRS method because they overlap with dominant metabolites like Cho and NAA.

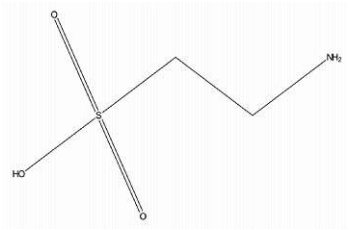

Taurine(Tau) ensures neural transmission and stabilizes cell membranes. It resonates at 3.42 and 3.25 ppm.

De Graaf (2019) includes a description of some other metabolites. Some metabolites are added up due to low SNR and deficient spectral resolution. Some examples are total Choline (tCho) from phosphorylcholine and glycerophosphorylcholin, tCR from Cr+PCr, Glx out of Glu added with Gln and total N-acetyl aspartate (tNAA) from NAA and N-acetyl-aspartyl glutamate (NAAG).

The amount of NAA is more than Cho of a normal brain. An increased amount of Cho raises suspicion of a tumor. The information about the chemical composition of these metabolites can be obtained through MRSI. MRSI is used to find information about the chemical composition of the brain. The high contrast in MRI indicates the presence of a tumor. In conclusion, MRI and MRSI are very useful methods in detecting tumors.

1.2 Glioma

The human brain comprises 86.1 billion neuron cells and 84.6 billion non-neuronal cells called glial cells (Azevedo et al., 2009). Glial cells are those in the brain that do

Die approbierte gedruckte Originalversion dieser Diplomarbeit ist an der TU Wien Bibliothek verfügbar
The approved original version of this thesis is available in print at TU Wien Bibliothek.

not produce electrical impulses. There are mainly three types of glial cells: Astrocytes, oligodendrocytes, and microglia. **Astrocytes** are mainly responsible for the structural composition and maintaining brain homeostasis. Astrocytes also form the blood-brain barrier (BBB), which controls the permeability of the brain to maintain the environment for the complex operations in the brain. However, a problem arises when antibodies cannot access the BBB to attack tumor cells in the brain. Even medical treatment gets challenging as they have difficulty accessing drugs through the barrier.

Oligodendrocytes are those glial cells in the central nervous system (CNS) involved in the myelination of axons. Myelination helps increase the conduction velocity of neuronal impulses in axons. Similar cells in peripheral nervous systems are Schwann cells. **Microglia** are administrative cells that maintain ionic concentration in extracellular compartments, interact with vessels during cell injury, and maintain structural balance for initially developing neurons.

Glioma is one of the tumors that begins in glial cells. 30% of brain and CNS tumors are gliomas (Goodenberger & Jenkins, 2012). Out of all malignant brain tumors, 80% are gliomas (Goodenberger & Jenkins, 2012). The nearest matching tissue histology defines the different types of gliomas. According to the 2021 World Health Organisation (WHO) classification of CNS tumors (fifth edition) (Louis et al., 2021), adult gliomas are histopathologically classified into three main groups:

- **Astrocytoma**

  Astrocytomas originate from astrocytes and do not spread out of CNS under normal circumstances. The patient life expectancy ranges from 1 to 10

Die approbierte gedruckte Originalversion dieser Diplomarbeit ist an der TU Wien Bibliothek verfügbar
The approved original version of this thesis is available in print at TU Wien Bibliothek.
TU Bibliothek Your knowledge hub WIEN

years after tumor diagnosis, depending on the type and grade of astrocytoma (Kennedy, 2021). They can be of grade II, III and IV (Louis et al., 2021).

- **Oligodendroglioma**

  Oligodendroglioma initiates from oligodendrocytes. They are less aggressive and grow relatively slow. The patients with oligodendroglioma have a higher survival rate in relation to the patients having other tumors. They can be of grade II and III (Louis et al., 2021).

- **Glioblastoma**

  Glioblastoma is the most common adult glioma accounting for 55 % of all gliomas, and is at the same time the most aggressive type. Patients only have a one-year survival rate of 42.8 % (Ostrom et al., 2020). All glioblastomas are of grade IV (Louis et al., 2021).

The diagnosis of glioma includes imaging diagnosis and biopsy. The imaging diagnosis of gliomas includes anatomical imaging of the brain using computed tomography (CT) and MRI. Once the tumor is detected in a CT scan or MRI, the tumor tissue is acquired through biopsy. The biopsy is done with a needle before, during or after surgery to test the type, grade and mutations of cells. Low grade and high grade are commonly used grading terms representing the malignancy of tumors based on WHO grade classification. The tumors of grade I and II are considered low-grade tumors, and those of grade III and IV are regarded as high-grade tumors.

A biopsy also includes the identification of mutations and molecular alteration in the tumor, which helps improve diagnosis, predict prognosis, make therapeutic decisions, and identify therapeutic targets. IDH and O6-methylow-gradeuanine DNA methyltransferase (MGMT) methylation status are prognostic values. Epidermal

Die approbierte gedruckte Originalversion dieser Diplomarbeit ist an der TU Wien Bibliothek verfügbar
The approved original version of this thesis is available in print at TU Wien Bibliothek.
TU Bibliothek Your knowledge hub WIEN

growth factor receptor(EGFR) mutation, Telomerase reverse transcriptase(TERT) promoter mutation, gain for 7p and loss of 10q chromosomes, and H3F3 mutation help improves diagnostic accuracy. Fibroblast growth factor receptor (FGFR) fusion and Neurotropic tyrosine receptor kinase (NTRK) fusion are therapeutic targets.

1.2.1 Isocitrate dehydrogenase (IDH)

The Isocitrate dehydrogenase (IDH) enzyme catalyses the oxidative decarboxylation of isocitrate, producing alpha-glutarate (α-ketoglurarate) and Carbon dioxide (CO_2), which are a vital part of cell homeostasis and metabolic processes. Due to this fact, they are also involved in the glioma cycle. In humans, they are mainly observed in three isoforms, IDH1, IDH2, and IDH3. IDH mutation is frequently seen in gliomas, with more than 80 % of WHO grade II/III cases with IDH1 or IDH 2 mutation (Yan et al., 2009). IDH without mutation is referred to as IDH wild-type. Gliomas with IDH wild-type behave more aggressively than those with mutations (Yan et al., 2009). WHO Classification 2021 of CNS Tumors (Louis et al., 2021) has defined IDH1 and IDH2 as characteristically altered genes for astrocytoma and oligodendroglioma and IDH wild-type for Glioblastoma along with other molecular profiles.

Surgery is done to remove the bulk of glioma tissue. Complete glioma removal is not always possible because gliomas infiltrate the surrounding brain. Due to this reason, additional radiation therapy and chemotherapy are conducted to kill the remaining glioma cells. A surgeon's goal is to remove as many gliomas as possible.

Die approbierte gedruckte Originalversion dieser Diplomarbeit ist an der TU Wien Bibliothek verfügbar
The approved original version of this thesis is available in print at TU Wien Bibliothek.
TU Bibliothek Your knowledge hub WIEN

1.3 Classification

Classification is an identification of the object's class based on its features. A single feature is not always sufficient to classify the object. The classification can be based on predefined labels and features or differences in features of the objects. The classification with the predefined label is supervised, and the one without previous labels is unsupervised learning. Nowadays, machine learning is widely used for classification purposes. Modern machine learning techniques involve training, validating, and testing processes. Training is where a classifier is trained to classify based on previous classification or label. Validation is to validate the proper training of the classifier. Testing is done to present the appropriate functioning of the classification. For each of these processes, a separate data set is desired. However, getting a large amount of data is not always possible. Thus, validation is mostly done using a training data set using an n-fold cross-validation process. The n-fold cross-validation process involves the division of data into "n" number of separate groups and testing the classifier "n" times, each time using a group of data out of "n" data groups.
Classifying glioma cells can help precisely identify glioma cells and decision-making for treatment. We intend to classify tumors based on IDH mutation and grade. We used a random forest and SVM algorithm for this classification.

1.3.1 Random forest

Random forest is a machine learning algorithm used for regression, classification, and other purposes. Random forest is based on the ensemble learning method where multiple classification layers, as in the figure 1.14, are used for end prediction. In the random forest, the prediction is based on decision trees. The classifier goes through multiple layers of decision trees before the end prediction is made. Prediction's re-

Die approbierte gedruckte Originalversion dieser Diplomarbeit ist an der TU Wien Bibliothek verfügbar
The approved original version of this thesis is available in print at TU Wien Bibliothek.
TU Bibliothek Your knowledge hub WIEN

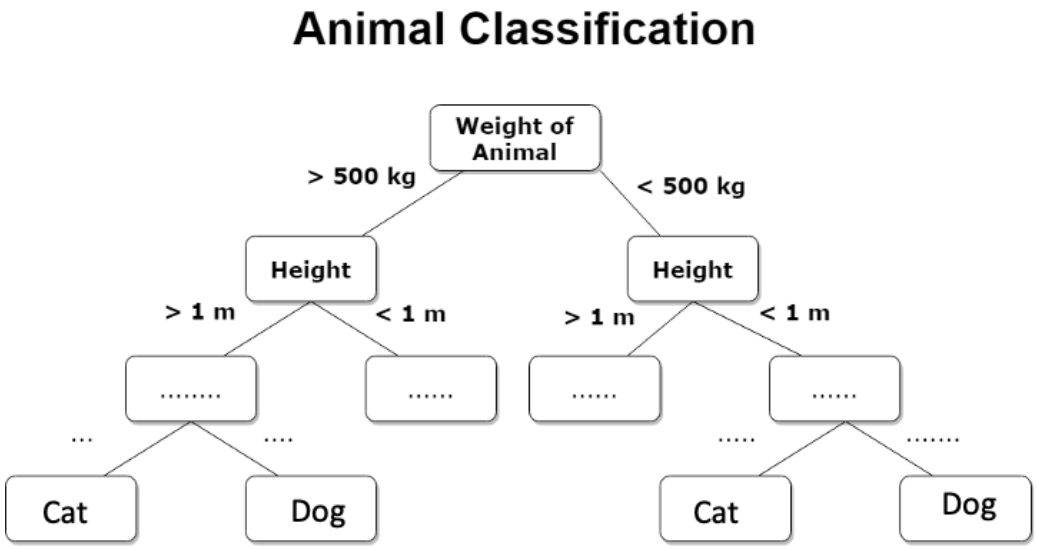

Figure 1.14: Decision tree involving multiple layer of classification

liability heavily depends on the number of decision trees used to train a classifier. Random forest is a supervised learning algorithm, meaning labelled outputs train the classifier. Supervised learning involves training the classifier until the classifier learns the pattern between input data and labelled output.

1.3.2 Support Vector Machine (SVM)

SVM is another machine learning tool widely used for regression and classification. The main idea behind SVM is to find a hyperplane in the multi-dimensional space to classify the data points in the space. For the optimal future classification, the hyperplane is desired to have the maximum possible distance from both classes, i.e., maximum marginal distance, to ensure better classification probability of additional data points. The dimension of the hyperplane depends on the number of features

Die approbierte gedruckte Originalversion dieser Diplomarbeit ist an der TU Wien Bibliothek verfügbar
The approved original version of this thesis is available in print at TU Wien Bibliothek.

involved in classification. The dimension of the hyperplane is n-1, where n is the number of features. The term support vector indicates the data points near the hyperplane, which plays a vital role in determining the position of the hyperplane.

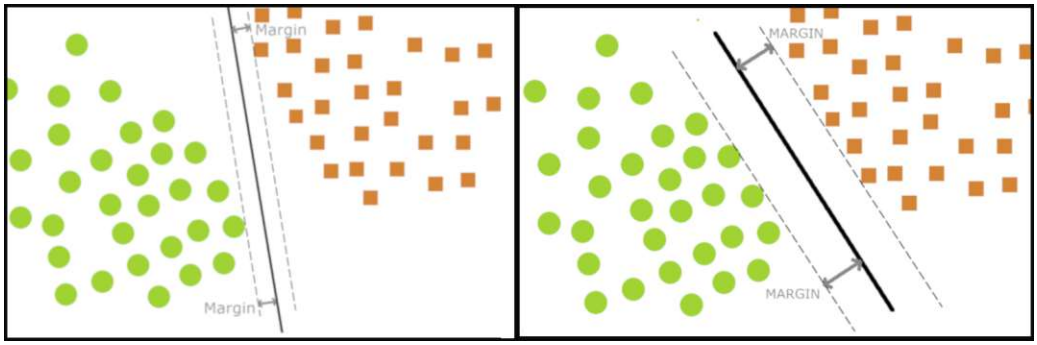

Figure 1.15: Support vectors and margins. The small margin on the left and the larger margin on the right.

The data points are not always linearly separable. In such cases, the data points are transformed to higher dimensions and the projection of higher dimensional separation to the original dimension results in non-linear boundaries. An increment in dimensions also increases computation cost. That is where the kernel trick comes into play. The linear kernel uses a linear separator, taking given features into consideration. At the same time, the non-linear kernel uses the given feature and the interaction of features in multiple ways to create non-linear separators. Polynomial kernel, radial basis function (RBF) kernel and sigmoid kernel are widely used SVM kernels. K-fold cross-validation is used for fine-tuning kernel parameters.

1.3.3 Feature Selection

Feature selection is a crucial part of machine learning. Feature selection is a process where the subset of the most relevant input variables for predicting output variables is

Die approbierte gedruckte Originalversion dieser Diplomarbeit ist an der TU Wien Bibliothek verfügbar
The approved original version of this thesis is available in print at TU Wien Bibliothek.
TU Bibliothek Your knowledge hub WIEN

selected. The features are selected based on their contribution to the classification. The features with higher contribution are iteratively selected. The unnecessarily higher number of features can lead to longer training time and over-fitting of a classifier.

The Recursive Feature Elimination Cross-Validation (RFECV) algorithm helps us determine essential features and the number of important features. RFECV combines the Recursive Feature Elimination (RFE) and Cross-Validation (CV) algorithms. RFE is a wrapper-based feature selection method. The different machine learning algorithms can be used as a wrapper to determine feature importance. RFE works similarly to the backward elimination method, which starts with the training process using all the given features and recursively eliminates the least important feature, calculated utilising a wrapper algorithm until a given number of features is reached. It is not always easy to determine the optimal number of features for machine learning. This is where RFECV comes into action. RFECV combines CV with RFE to determine an optimal number of features. The CV score is computed for each subset of features, from the maximum to the minimum number of features. The minimum number of features is provided as an argument. The subset of features with the highest CV score is selected for the training process.

1.3.4 Receiver Operating Characteristic (ROC) curve and Area Under the Curve (AUC)

ROC curve is plotted for classification with different threshold settings, an evaluation measure to determine the performance of binary classification. The ROC curve involves a True Positive Rate (TPR) and False Positive Rate (FPR). These parameters are derived from the elements of the confusion matrix in figure 1.16 and defined

Die approbierte gedruckte Originalversion dieser Diplomarbeit ist an der TU Wien Bibliothek verfügbar
The approved original version of this thesis is available in print at TU Wien Bibliothek.
TU Bibliothek Your knowledge hub WIEN

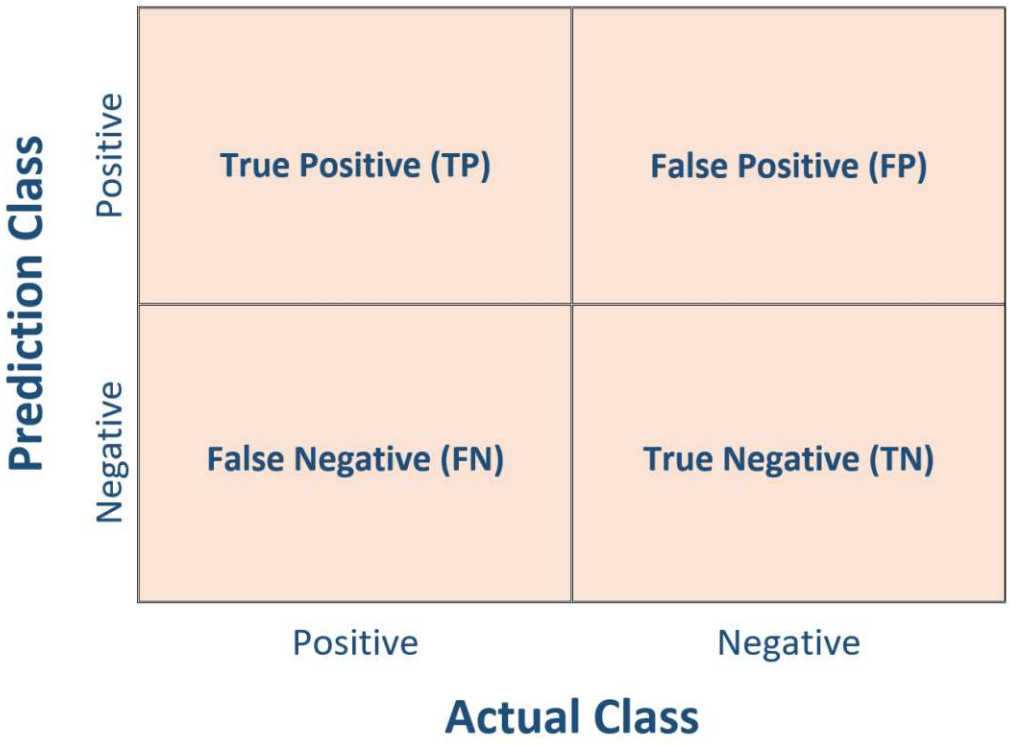

Figure 1.16: Confusion matrix

Die approbierte gedruckte Originalversion dieser Diplomarbeit ist an der TU Wien Bibliothek verfügbar
The approved original version of this thesis is available in print at TU Wien Bibliothek.

as:

$$TPR = \frac{TP}{TP + FN} \tag{1.22}$$

$$FPR = \frac{FP}{FP + TN} \tag{1.23}$$

The ROC curve is a curve of the relationship between TPR and FPR for different threshold settings, as shown in figure 1.17

AUC is the area under the ROC curve, as in figure 1.17. AUC measures classification performance and signifies the model's classification accuracy. AUC equals 0.5 means the classification is equivalent to the random prediction of binomial classification. The AUC value below or higher than 0.5 means better classification than random prediction. The AUC value generally varies from 0.5 to 1. A higher AUC means a better classification model. The AUC is lower than o. five is equally good as more significant than 0.5 but should be inversely labelled.

Die approbierte gedruckte Originalversion dieser Diplomarbeit ist an der TU Wien Bibliothek verfügbar
The approved original version of this thesis is available in print at TU Wien Bibliothek.
TU Bibliothek Your knowledge hub WIEN

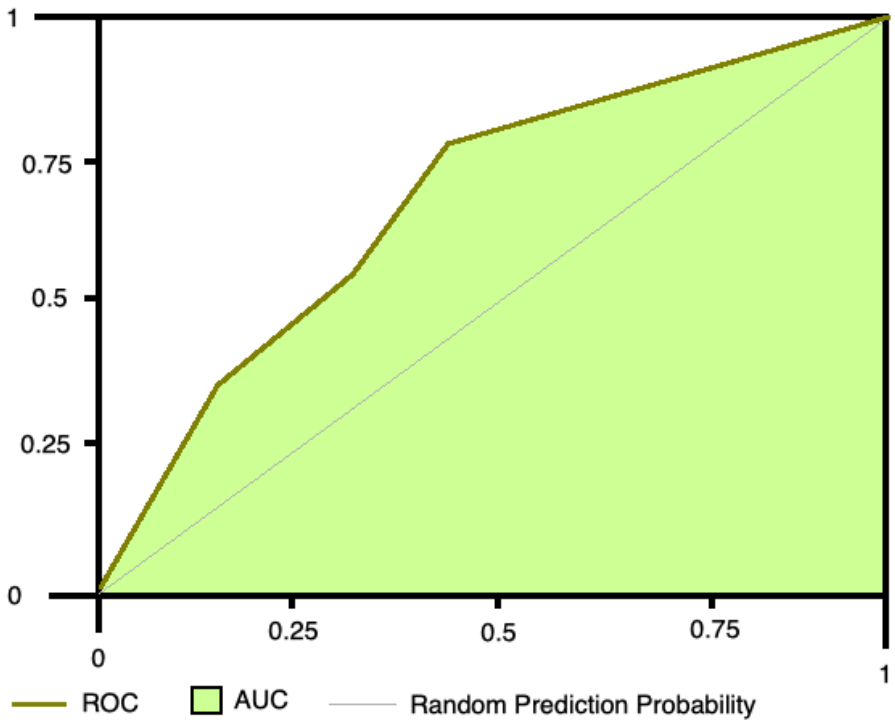

Figure 1.17: An example of the Receiver Operating Characteristic (ROC) curve and Area Under the Curve (AUC).

Die approbierte gedruckte Originalversion dieser Diplomarbeit ist an der TU Wien Bibliothek verfügbar
The approved original version of this thesis is available in print at TU Wien Bibliothek.

Die approbierte gedruckte Originalversion dieser Diplomarbeit ist an der TU Wien Bibliothek verfügbar
The approved original version of this thesis is available in print at TU Wien Bibliothek.

Die approbierte gedruckte Originalversion dieser Diplomarbeit ist an der TU Wien Bibliothek verfügbar
The approved original version of this thesis is available in print at TU Wien Bibliothek.

Chapter 2

Methods

The main objective of this thesis is to build a pipeline for statistical evaluations, which is further developed to classify IDH mutation and tumor grade. The research begins with patient recruitment and measurement. The data obtained from measurement goes through in-house built data post-processing resulting in 3D-MRI and MRSI images. As we focus on tumor regions, we also acquired tumor segmentation. After obtaining all the required image data, we further worked on building a database. The database was used for statistical evaluation and classification using the python programming language (Van Rossum & Drake Jr, 1995).

2.1 Patient recruitment

This study is based on 7T 3D-concentric ring trajectory (CRT)-based free induction decay (FID)-MRSI of 36 preoperative glioma patients. The used dataset consists of 14 female and 22 male patients within the age group of 33-77 years. Although we had initially recruited 57 patients, 21 measurements had to be eliminated in the

preliminary quality assessment.

Pat Code	Age at Measurement	Sex (Female)	WHO 2021	Grade	IDH Mutation
Tumor_Patient_021	39	0	Astrocytoma grade 2	2	IDH1
Tumor_Patient_023	51	0	Astrocytoma grade 4	4	IDH1
Tumor_Patient_027	52	0	Astrocytoma grade 4	4	IDH1
Tumor_Patient_030	47	1	Glioblastoma grade 4	4	WT
Tumor_Patient_031	46	1	Astrocytoma grade 3	3	IDH1
Tumor_Patient_034	29	0	Astrocytoma grade 3	3	IDH1
Tumor_Patient_035	52	0	Glioblastoma grade 4	4	WT
Tumor_Patient_037	33	0	Astrocytoma grade 2	2	IDH1
Tumor_Patient_038	58	0	Glioblastoma grade 4	4	WT
Tumor_Patient_039	77	1	Astrocytoma grade 2	2	IDH1
Tumor_Patient_040	34	1	Astrocytoma grade 3	3	WT
Tumor_Patient_046	71	0	Glioblastoma grade 4	4	WT
Tumor_Patient_050	51	0	Oligodendroglioma grade 3	3	IDH1
Tumor_Patient_054	62	0	Astrocytoma grade 3	3	IDH1
Tumor_Patient_055	30	1	Glioblastoma grade 4	4	WT
Tumor_Patient_056	34	0	Astrocytoma grade 2	2	IDH1
Tumor_Patient_057	56	0	Oligodendroglioma grade 3	3	IDH1
Tumor_Patient_058	61	0	Glioblastoma grade 4	4	WT
Tumor_Patient_059	60	0	Glioblastoma grade 4	4	WT
Tumor_Patient_062	28	1	Astrocytoma grade 3	3	IDH1
Tumor_Patient_063	62	0	Glioblastoma grade 4	4	WT
Tumor_Patient_065	50	1	Oligodendroglioma grade 2	2	IDH1
Tumor_Patient_066	38	1	Oligodendroglioma grade 2	2	IDH1
Tumor_Patient_067	61	0	Oligodendroglioma grade 2	2	IDH1
Tumor_Patient_068	77	1	Glioblastoma grade 4	4	WT
Tumor_Patient_073	33	0	Astrocytoma grade 2	2	IDH1
Tumor_Patient_074	75	1	Glioblastoma grade 4	4	WT
Tumor_Patient_078	58	0	Glioblastoma grade 4	3	WT
Tumor_Patient_081	57	1	Oligodendroglioma grade 3	3	IDH1
Tumor_Patient_084	40	0	Astrocytoma grade 3	3	IDH1
Tumor_Patient_086	58	0	Glioblastoma grade 4	4	WT
Tumor_Patient_091	27	1	Astrocytoma grade 4	4	IDH1
Tumor_Patient_096	72	0	Glioblastoma grade 4	4	WT
Tumor_Patient_098	26	1	Astrocytoma grade 4	4	IDH1
Tumor_Patient_100	59	0	Glioblastoma grade 4	4	WT
Tumor_Patient_104	46	1	Glioblastoma grade 4	4	WT

Table 2.1: Patients list with age, gender, who classification, grade and IDH mutation

Die approbierte gedruckte Originalversion dieser Diplomarbeit ist an der TU Wien Bibliothek verfügbar
The approved original version of this thesis is available in print at TU Wien Bibliothek.
TU Bibliothek Your knowledge hub WIEN

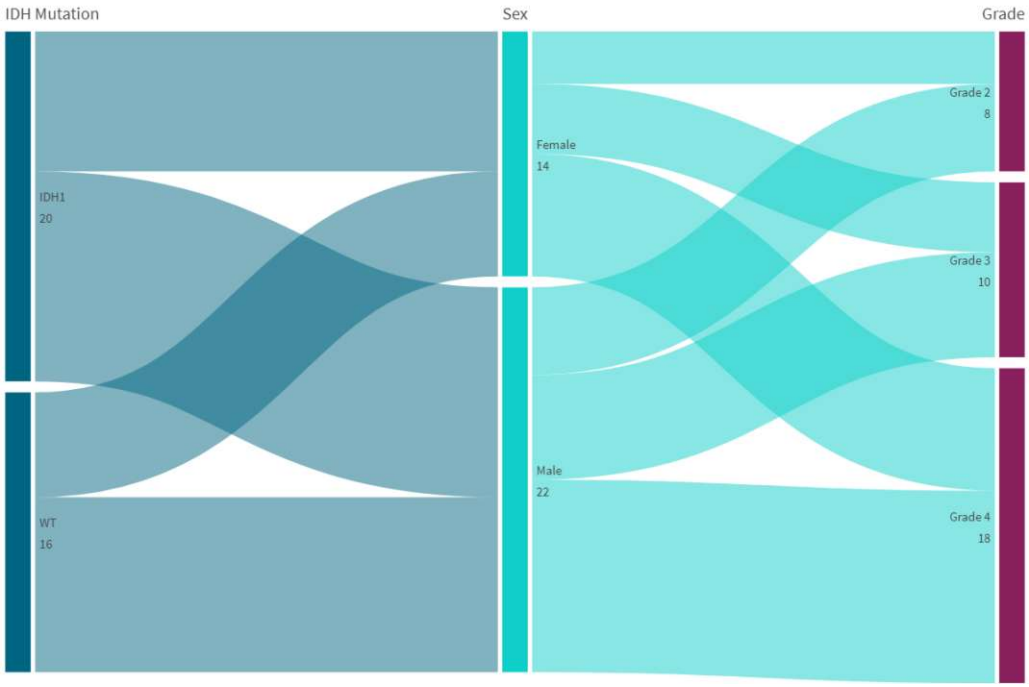

Figure 2.1: Distribution and interrelation of data classes.

2.2 Measurement Procedure

The measurement was performed using Magnetom (Siemens Healthineers, Erlangen, Germany) 7T whole-body MR scanner in the High Field MR Center of the Medical University of Vienna. The MR Scanner features a gradient system with a 70 mT/m of maximum gradient strength per direction, a 200 mT/m/s slew rate, and a 32-channel head receive coil array by Nova Medical (Wilmington, MA). B_1^+ maps for flip-angle optimization, B_0 maps, magnetization prepared two rapid gradient echoes (MP2RAGE) as the T_1-weighted morphological MRI reference (T_R 5000 ms, T_E 4.13 ms, T_{I1} 700 ms, T_{I2} 2700 ms, 0.75 x 0.75 x 0.75 mm^3 resolution, 8 min 2s with GRAPPA factor 3) was included in the protocol. 3D-CRT-FID-MRSI with the 3-

Die approbierte gedruckte Originalversion dieser Diplomarbeit ist an der TU Wien Bibliothek verfügbar
The approved original version of this thesis is available in print at TU Wien Bibliothek.

dimensional encoding of ellipsoidal k-space and phase encoding for in-plane encoding as described by Hingerl et al. (2020) results in a 64 x 64 x 39 matrix over a 220 x 220 x 133 mm^3 FOV with a nominal spatial resolution of 3.4 x 3.4 x 3.4 mm^3 and an effective resolution of 4.7 x 4.7 x 4.7 mm^3 or 0.1 cm^3. A 110m thick slab parallel to the horns of the corpus callosum, beginning from the superior part of the brain, was selected. The additional parameters of the MRSI scan include repetition time (T_R) of 450 ms, the scan time of 15 min, acquisition delay of 1.3ms, 39 °excitation flip angle as nominal average Ernst angle of NAA, tCr, tCho, Glu and mIns (Hangel et al., 2015), readout duration of 345 ms, the spectral bandwidth of 2778 Hz, varial temporal interleaves and 7T-optimized WET water suppression (Hangel et al., 2018; Ogg et al., 1994). The measurement does not include lipid suppression sequence to ensure short T_R. The lipid signal removal is performed in post-processing using L2-regularization (Bilgic et al., 2013).

2.3 Data post-processing

An in-house developed software pipeline (Považan et al., 2015) was used to post-process MRSI data. The pipeline is based on MINC (MINC Tools, McConnell Brain Imaging Center, Montreal, QC, Canada), MATLAB (MathWorks, Natick, MA), Bash (Free Software Foundation, Boston, MA) and FSL (Analysis Group, FMRIB, Oxford, UK). The pipeline comprises iMUSICAL coil combination (Hingerl et al., 2018; P. Moser et al., 2019; Strasser et al., 2013) with water normalization as in (A. Maudsley et al., 2009) and k-space reconstruction with in-plane spiral grids (Hingerl et al., 2018; Jackson et al., 1991). The post-processing also includes an off-resonance correction to compensate for the time delay of acquisition samples (Mayer et al., 2006). Spatial Hamming filtering and post-measurement lipid removal by L2 regularization (Bilgic

Die approbierte gedruckte Originalversion dieser Diplomarbeit ist an der TU Wien Bibliothek verfügbar
The approved original version of this thesis is available in print at TU Wien Bibliothek.

et al., 2013; Hangel et al., 2016) prior to spectral quantification are also included in post-processing.

LCModel (v6.3-1, LCMODEL, Oakville, Ontario, Canada) (Provencher, 2001) was used to quantify each spectrum. The range of spectrum evaluation comprises 0.2-1.2 ppm and 1.8-3.88 ppm. 1.2-1.8 ppm is excluded due to the possibility of remaining lipid signal after L2 regularization. The upper limit of 3.88ppm spectrum was chosen due to water suppression effects. The basic metabolites used for this thesis are Cr, PCr, GPC, PCh, NAA, NAAG, Glu, Gln, Ins, GABA, GSH, Gly, Tau, and serine (Ser). SNR was accomplished using the pseudo-replica method (Strasser et al., 2017), and FWHM was calculated for each voxel with the help of LCModel fits of NAA and tCr at 3.02 ppm. Grey matter (GM), white matter (WM), and cerebrospinal fluid (CSF) segmentation were acquired using FSL's FAST tool. The filters like tCr SNR < 5, tCr FWHM > 0.15, CRLB > 40 %, and metabolite fit value > 13 recommended by Wilson et al. (2019) were applied to ensure spectral quality.

2.4 Pipeline

The 3D-MINC maps of metabolites obtained by the post-processing are used as input for the new pipeline. With promising outcomes in the past for high-grade gliomas (HGG) (Hangel et al., 2020), this study aims to find out the combination of metabolites that can help us with the prediction and prognosis of glioma. To study this possibility, we need to observe the pattern of difference in the concentration of metabolites in tumor and non-tumor regions. We further focus our study on IDH mutation and the grade of the tumor. We intend to find the dependence of IDH mutation and tumor grade with the concentration of metabolites to predict those factors for other patients in the future with an exact combination of metabolites

Die approbierte gedruckte Originalversion dieser Diplomarbeit ist an der TU Wien Bibliothek verfügbar
The approved original version of this thesis is available in print at TU Wien Bibliothek.
TU Bibliothek Your knowledge hub WIEN

concentration. We intend to find a metabolite combination, which we can use to classify IDH mutation status and grade based on their concentration in patients' brains.

2.4.1 Tumor segmentation

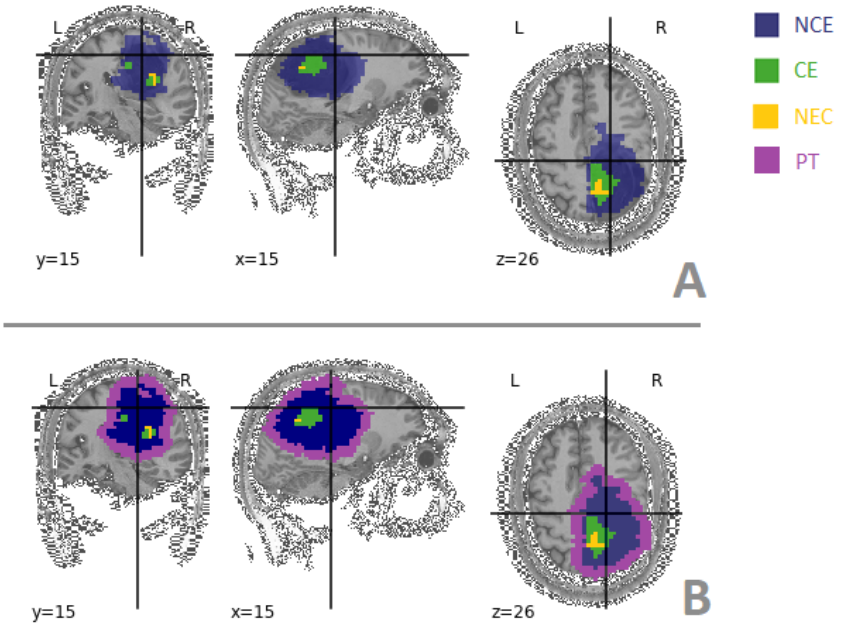

Figure 2.2: A: Tumor segmentation by neuro-radiologist co-registered on the anatomical image. B: Peritumoral region around tumor using a dilation operation. The blue colour indicates the non-contrast enhancing (NCE), green indicates contrast-enhancing (CE), yellow indicates necrosis (NEC), and purple for the peritumoral (PT) region. L and R are for the left and right side of the brain, and x, y, and z indicates sagittal, frontal, and transverse slice.

To differentiate between tumor and non-tumor regions, we first need to compare the concentration of the metabolites in those regions. The manual segmentation of tumors is the gold standard for segmentation though it is time-consuming. For

Die approbierte gedruckte Originalversion dieser Diplomarbeit ist an der TU Wien Bibliothek verfügbar
The approved original version of this thesis is available in print at TU Wien Bibliothek.
TU Bibliothek Your knowledge hub WIEN

segmentation of the tumor region, we requested the neuro-radiologist Julia Furtner for help. An experienced neuro-radiologist provided tumor segmentation for non-contrast enhancing (NCE) or edema, contrast-enhancing (CE), and necrosis (NEC) regions as shown in2.2. The segmentation was performed on a T1-weighted 7T-MRI 144 x 192 x 192 matrix image. It was resampled and co-registered with the 7T-MRSI 64 x 64 x 39 matrix maps.

The peritumoral (PT) region was later defined using a mathematical operation called dilation. The tumor's three layers of boundary voxels (3 x 3.4mm) were defined as a peritumoral region. Nibabel package (Gorgolewski et al., 2011) was used in python to read minc and nifti images. Numpy (C. R. Harris et al., 2020) and Scipy (Virtanen et al., 2020) packages were used for loading and processing image data in nifti and minc format.

2.4.2 Preliminary image quality assessment

A visual qualitative evaluation of the images was done for preliminary quality assessment. The main focus of the assessment was overall image quality, artefacts, tumor segmentation, and location of the tumor, as the tumors on the boundary and lower extremities of the head are more prone to artefacts. MRSI map of tNAA, tCho to tCr ratio, segmentation map, and magnitude map were used to determine quality criteria. Out of 57 initial cohorts, 15 had to be eliminated because of insufficient quality. Six were later eliminated due to incomplete data labelling information.

Die approbierte gedruckte Originalversion dieser Diplomarbeit ist an der TU Wien Bibliothek verfügbar
The approved original version of this thesis is available in print at TU Wien Bibliothek.
TU Bibliothek Your knowledge hub WIEN

2.5 MRSI Statistical Evaluation

Figure 2.3 shows the process of building a database and further use of the database for statistical evaluation. Before beginning with the statistical evaluation of MRSI data, we must build a database. Using a single comma-separated value (CSV) file as a database of statistical assessment is far more convenient than multiple 3D-image files. So, the first part of this work involved building a CSV file out of all the 3D-MRSI images in .mnc (minc format) and .nii (nifti format). Numpy (C. R. Harris et al., 2020) and Scipy (Virtanen et al., 2020) packages were used for reading 3D Minc and nifti images and converting them to table columns.

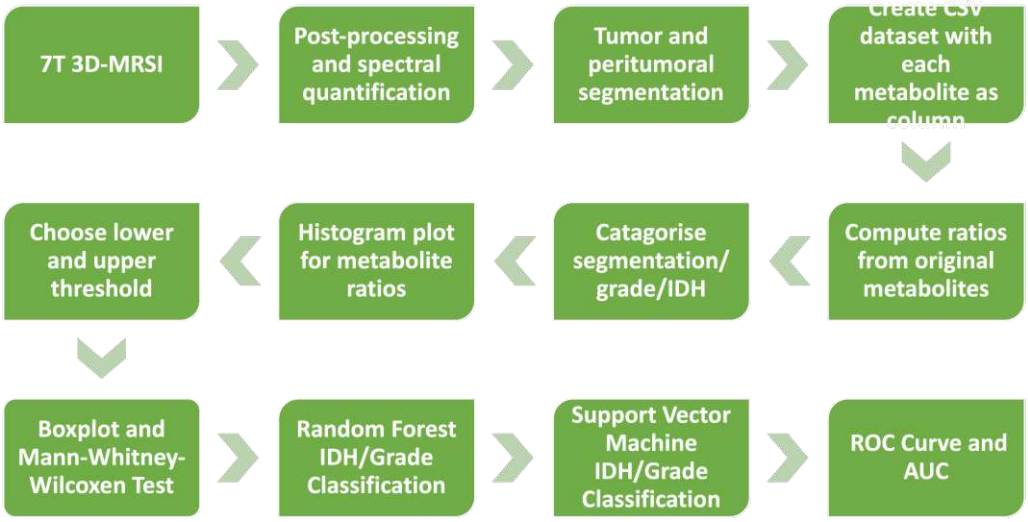

Figure 2.3: The process of building a database and further use of a database for statistical evaluation.

Die approbierte gedruckte Originalversion dieser Diplomarbeit ist an der TU Wien Bibliothek verfügbar
The approved original version of this thesis is available in print at TU Wien Bibliothek.
TU Bibliothek Your knowledge hub WIEN

2.5.1 CSV Database

The original metabolic MRSI 3D-MINC maps obtained after post-processing and the resampled segmentations from neuroradiologists (Figure 2.3) were used for each patient. The original metabolite maps used for statistical evaluation include tCr, GABA, Gln, Glu, GABA+Glu, Glu+Gln, Gly, tCho, GSH, Ins, Ins+Gly, NAA, NAAG, tNAA, Ser, and Tau. For each metabolite, ratios to tCr, NAA, and tNAA were calculated. Other ratios like Gly to Ins, Gly to Ins+Gly, Gln to Glu+Gln, and Glu to Glu+Gln were individually calculated. All these ratios are used for further statistical evaluation. We also included Cr mask maps, WM maps, and GM maps created during the data post-processing.

Firstly, the local coordinate system was defined for each voxel with the dimension of 64, 64, and 39 for the x, y, and z variables respectively. The coordinate system further helps to identify and plot each voxel in the table significantly. All the 3D maps were further converted to single-dimensional arrays with 159744 (64 x 64 x 93) elements. Cr mask maps, WM maps, and GM maps were initially added to the table. Each metabolites array was multiplied by a Cr mask to filter the voxels in the defined VOI. All the voxels outside of the Cr mask are then zero. These arrays are further added as an additional column to the database table. The metabolite ratios were calculated using the metabolite maps array, and the obtained ratios were also added as individual columns to the database table. The table for each patient now consists of preliminary histopathological information from the table 2.1 followed by XYZ coordinates, Cr mask map, WM maps, GM maps, MRSI voxel values from original 3D-MRSI maps of metabolites, and ratios of metabolites computed from original 3D-MRSI metabolite maps. An individual CSV file was created for each

Die approbierte gedruckte Originalversion dieser Diplomarbeit ist an der TU Wien Bibliothek verfügbar
The approved original version of this thesis is available in print at TU Wien Bibliothek.
TU Bibliothek Your knowledge hub WIEN

patient with 159744 rows.

As a next step, the CSV files for each patient are combined and post-processed to add the information required for the latter data evaluation. The CSV file for each patient is further filtered, and only Cr masked volume is acquired, as all required brain MRS information is contained in Cr masked volume. Furthermore, the Cr-masked regions from all the patients were combined into a single table, primarily used for statistical evaluation. We further defined the brain regions that were detected as Tumor VOI, Peritumoral VOI, and NAWM (Normal appearing white matter) using WM MRSI maps and tumor segmentation maps. IDH mutation label was provided for each voxel. The tumoral regions of patients with histopathological IDH-1 mutation were labelled as IDH positive (IDH column = 1), else; other voxels were defined as 0. The IDH mutation of peritumoral regions were separately defined as PT1 (Peritumoral region of the patient with IDH-1 mutation) and PT0 (Peritumoral region of the patient with wild-type mutation).

Similarly, for a grade, the high-grade column was defined and labelled as one for patients with high-grade tumors and labelled as zero for patients with low-grade tumors.

We finally had the CSV table with voxels in Cr masked regions of all the patients. Each voxel has defined coordinates and is labelled with the region of a tumor, IDH status, WM and GM content, Grade classification, age, gender, and patient code to whom they belong. The database table looks like the figure 2.4, which is further used for our statistical evaluation. Pandas (McKinney et al., 2010) was used to create tables and further statistical data analysis in python (Van Rossum & Drake Jr, 1995).

Die approbierte gedruckte Originalversion dieser Diplomarbeit ist an der TU Wien Bibliothek verfügbar
The approved original version of this thesis is available in print at TU Wien Bibliothek.
TU Bibliothek Your knowledge hub WIEN

Pat Code	Age at M	Gender (Female)	High_grade	Grade	WHO 2021	IDH	coordinate:x	coordinate:y	coordinate:z	Segmentation Region	WM	GM	Cr_mask	Cr+PCrToNAA	CysToNAA	GABAToNAA	GPC+PChToNAA
Tumor_Patient_098	26	1	1	4	Astrocytoma grade 4	1	24	34	36	1 Tumor VOI	0,24	0,76	1	0,431	0,000	0,200	0,240
Tumor_Patient_098	26	1	1	4	Astrocytoma grade 4	1	24	34	37	1 Tumor VOI	0,19	0,81	1	0,986	0,095	0,000	0,375
Tumor_Patient_098	26	1	1	4	Astrocytoma grade 4	1	24	34	38	1 Tumor VOI	0,16	0,84	1	1,243	0,103	0,000	0,427
Tumor_Patient_098	26	1	1	4	Astrocytoma grade 4	1	24	34	39	1 Tumor VOI	0,23	0,77	1	0,859	0,068	0,000	0,468
Tumor_Patient_098	26	1	1	4	Astrocytoma grade 4	1	24	34	40	1 Tumor VOI	0,37	0,63	1	1,009	0,109	0,000	0,437
Tumor_Patient_098	26	1	1	4	Astrocytoma grade 4	1	24	34	41	1 Tumor VOI	0,48	0,52	1	1,078	114,000	0,000	0,400
Tumor_Patient_098	26	1	1	4	Astrocytoma grade 4	1	24	34	42	1 Tumor VOI	0,27	0,73	1	0,845	0,000	0,000	0,304
Tumor_Patient_098	26	1	1	4	Astrocytoma grade 4	1	24	34	43	1 Tumor VOI	0,59	0,41	1	0,553	0,000	0,219	0,338
Tumor_Patient_098	26	1	1	4	Astrocytoma grade 4	1	24	34	44	1 Tumor VOI	0,49	0,51	1	0,627	0,000	0,048	0,301
Tumor_Patient_098	26	1	1	4	Astrocytoma grade 4	1	24	34	45	1 Tumor VOI	0,13	0,87	1	655,000	0,000	0,000	0,208

Figure 2.4: The structure of the database table used for statistical evaluation.

2.5.2 Histogram Analysis

After we get the database, the first thing we wanted to do is to see how our data is distributed. As we deal with enormous amounts of data, knowing the distribution procedure was essential. A histogram is an essential tool that helps us visualize and analyze our data to find the boundary where most data occur. It also allows us to see the primary differentiation between tumor and non-tumor data and their dominance in the amount of data.

Our primary focus is the tumor region; we tried to plot the histogram of tumor regions as shown in figure 3.2 and 3.1. We also included the peritumoral region in the histogram. We further calculated the median of the data and plotted it on a diagram to see where most of our data lie. It helps us set the data's lower and upper limits and eliminate unnecessary outliers.

2.5.3 Mann-Whitney-Wilcoxon Test and Boxplot

After data visualization through histogram, we realized our data were not normally distributed. We also determined the lower and upper cutoff for the data, which helps us to focus on the hotspots. With this information, we wanted to see if there is any statistically significant difference between the tumors with IDH-1 mutation and wild-type mutation using the Mann-Whitney-Wilcoxon test. We further used Boxplot to

Die approbierte gedruckte Originalversion dieser Diplomarbeit ist an der TU Wien Bibliothek verfügbar
The approved original version of this thesis is available in print at TU Wien Bibliothek.
TU Bibliothek Your knowledge hub WIEN

visualize the difference in these groups of patients. Before choosing Mann-Whitney-Wilcoxon Test, the Shapiro-Wilks test was performed to check the normality and Leven's Test to check the homogeneity of variance of the data as a prerequisite test for the T-test. Shapiro-Wilks test reported the conclusion that the data is not normally distributed. So, we opted for Mann-Whitney-Wilcoxon Test.

2.5.4 IDH Classification

The significant difference in concentration of metabolite ratios for IDH-1 mutation and Wild-type mutation contributes to the possibility of IDH mutation classification with the help of differentiation in metabolite ratios. Random forest regression was used for the classification of IDH mutation. Random forest and SVM being supervised machine learning algorithms are suitable for our application as our patients are labelled using histopathological biopsy reports. Sciencekit Learn packages (Pedregosa et al., 2011) were used for the complete classification. SVM takes computationally much more time than random forest. The random forest was approximately eight times faster than SVM for our computation.

Feature Selection

Before we began with feature selection, the correlation matrix of the features was built, and one out of two ratios with a correlation coefficient greater than 0.95 were eliminated from the classification dataset. A wrapper-type RFECV algorithm was used for the feature selection of the classifier. The random forest with ten decision trees and five-fold cross-validation was used as a wrapper for feature selection using the RFECV method.

Die approbierte gedruckte Originalversion dieser Diplomarbeit ist an der TU Wien Bibliothek verfügbar
The approved original version of this thesis is available in print at TU Wien Bibliothek.
TU Bibliothek Your knowledge hub WIEN

Training and Testing

Once an optimal subset of features is selected, classification training and testing were performed using the leave-one-out method. Leave-one-out is a method where data from a single patient is separated as a testing set, and all other patient's data are used for training. This process is iteratively applied to each patient. In this way, the prediction probability for each tumor voxel of all patients was calculated iteratively. All the patients except one were used as the training set in each prediction loop, and exempted patient data was used as a testing set.

2.5.5 Grade Classification

Like IDH classification, grade classification was performed using random forest and SVM. The feature selection method and classification process were similar to IDH classification. The high-grade and low-grade labelling obtained from histopathological findings, as shown in figure 2.1, was used for supervised training.

2.5.6 Threshold Comparisons

To improve our classifier, we further decided to threshold the tumor region. Using thresholded regions, we can focus on the tumour's hotspot regions, improving the classifier's training. We utilized concentration estimates of metabolites in (Hangel et al., 2021) to calculate concentration estimates for our metabolite ratios for different regions of interest. The min, mean, and max were calculated from the data obtained in table 2.5.6 and individually used as a lower threshold for our evaluation. To determine the upper threshold, we plotted a histogram for our whole data and found only some outliers greater than ten as in the figure 3.2.

Die approbierte gedruckte Originalversion dieser Diplomarbeit ist an der TU Wien Bibliothek verfügbar
The approved original version of this thesis is available in print at TU Wien Bibliothek.
TU Bibliothek Your knowledge hub WIEN

Index	ROI	GPC+PChTo NAA+NAAG	GlnTo NAA+NAAG
0	Subcortical WM (left)	0.16	0.18
1	Subcortical WM (right)	0.17	0.17
2	Subcortical WM (bilateral)	0.16	0.18
3	Motor subcortex WM	0.15	0.13
4	Motor cortex GM	0.14	0.17
5	Motor cortex/subcortex GM+WM	0.15	0.14
6	Parietal subcortex WM	0.15	0.15
7	Parietal cortex GM	0.14	0.19
8	Parietal cortex/subcortex GM+WM	0.14	0.17
9	Cingulate subcortex WM	0.18	0.15
10	Cingulate cortex GM	0.17	0.19
11	Cingulate cortex/subcortex GM+WM	0.18	0.16
12	Visual subcortex WM	0.14	0.19
13	Primary somatosensory subcortex WM	0.14	0.17
14	Primary somatosensory cortex/subcortex GM+WM	0.14	0.18
15	Thalamus	0.18	0.19
16	Putamen	0.2	0.27
17	Non-lobe WM	0.2	0.13
18	Cortical GM (left)	0.15	0.21
19	Cortical GM (right)	0.15	0.2
20	Cortical GM (bilateral)	0.15	0.21
21	Cortical GM+ subcortical WM (left)	0.16	0.2
22	Cortical GM+ subcortical WM (right)	0.16	0.19
23	Cortical GM+ subcortical WM (bilateral)	0.16	0.19
24	Subcortical GM (left)	0.2	0.21
25	Subcortical GM (right)	0.21	0.25
26	Subcortical GM (bilateral)	0.2	0.23
27	Auditory subcortex WM	0.18	0.25
28	Auditory cortex GM	0.17	0.28
29	Auditory cortex/subcortex GM+WM	0.18	0.26
30	Occipital subcortex WM	0.15	0.2
31	Occipital cortex GM	0.14	0.22
32	Occipital cortex/subcortex GM+WM	0.15	0.21
33	Temporal subcortex WM	0.19	0.23
34	Temporal cortex/subcortex GM+WM	0.18	0.24
35	Frontal subcortex WM	0.17	0.18
36	Frontal cortex GM	0.15	0.2
37	Frontal cortex/subcortex GM+WM	0.16	0.19
38	Visual cortex GM	0.12	0.21
39	Visual cortex/subcortex GM+WM	0.13	0.19
40	Primary somatosensory cortex GM	0.14	0.19
41	Pallidum	0.2	0.28
42	Hippocampus	0.24	0.26
43	Corpus callosum	0.18	0.16
	Min	0.12	0.13
	Max	0.24	0.28
	Mean	0.17	0.2

Table 2.2: Threshold table derived from Hangel et al., 2021 metabolite table

Die approbierte gedruckte Originalversion dieser Diplomarbeit ist an der TU Wien Bibliothek verfügbar
The approved original version of this thesis is available in print at TU Wien Bibliothek.
TU Bibliothek Your knowledge hub WIEN

So we decided on ten as our upper threshold. 'GPC+PChToNAA+NAAG' and 'GlnToNAA+NAAG' were used for thresholding. Voxels with metabolite ratios below the lower and above the higher threshold values were eliminated. Thus, we compared the classification where whole tumor region data was used with those using min, mean, and max as lower and ten as upper threshold.

2.5.7 Single vs Multiple Feature Comparison

Increased GPC+PCh and decreased NAA+NAAG are mentioned as important ratios for glioma in some literature, including (Hangel et al., 2020). Thus, we compared classification using GPC+PCh/NAA+NAAG as a single feature and classifications using multiple features from feature selection, including GPC+PCh/NAA+NAAG. We intended to understand the contribution of features other than GPC+PCh/NAA+NAAG in classification.

2.5.8 ROC Curve and AUC

For each patient, the prediction probability for all voxels of the tumor region was calculated. The prediction probabilities for each voxel were used to calculate the aggregate prediction for each patient. Again Sciencekit Learn (Pedregosa et al., 2011) and Matplotlib (Hunter, 2007) python package were used to compute AUC and draw ROC curves.

Different methods were used to compute aggregate prediction out of voxel classification for each patient. Four aggregation methods used to compute ROC and AUC are listed below :

- **Voxelwise ROC curve**

  This method is pretty simple. The prediction probability for each voxel ob-

Die approbierte gedruckte Originalversion dieser Diplomarbeit ist an der TU Wien Bibliothek verfügbar
The approved original version of this thesis is available in print at TU Wien Bibliothek.
TU Bibliothek Your knowledge hub WIEN

tained from random forest analysis was used to plot the ROC curve and calculate AUC. The ROC curve, in this case, shows TPR and FPR for different threshold values. The other methods of aggregation are derived from voxelwise classification.

- **ROC curve with prediction probability**

  In this method, the binomial classification of each voxel was obtained from the random forest with 0.5 as the threshold point for IDH positive and high-grade classification. The percentage of IDH positive or high-grade voxel in each patient was calculated. The ROC curve was then plotted based on these percentages of IDH positive or high-grade voxels, and AUC was calculated. ROC curve, in this case, shows what percent of IDH positive predicted voxels (high-grade predicted voxels in case of grade) is suitable to classify the patient as an IDH positive or high-grade tumor patient.

- **ROC curve with mean probability**

  This method uses the prediction probability of each voxel obtained from a random forest. The mean probability for IDH positive or high-grade classification was calculated from each voxel in a patient. Based on the mean probability of each patient, the ROC curve was plotted, and AUC was computed. The ROC curve here shows what cutoff mean probability value would be suitable for classifying a patient as IDH positive or high-grade tumor patient.

- **ROC curve with median probability**

  This method is similar to the above-mentioned mean probability method. The only difference is that here median is used instead of the mean.

Die approbierte gedruckte Originalversion dieser Diplomarbeit ist an der TU Wien Bibliothek verfügbar
The approved original version of this thesis is available in print at TU Wien Bibliothek.
TU Bibliothek Your knowledge hub WIEN

Die approbierte gedruckte Originalversion dieser Diplomarbeit ist an der TU Wien Bibliothek verfügbar
The approved original version of this thesis is available in print at TU Wien Bibliothek.

Chapter 3

Results

As discussed in the method, our evaluation started with histogram plots, which let us know the data range. Then we plotted the differences in IDH mutations using Box-plot and Mann-Whitney-Wilcoxon test. After seeing substantial differences in these tests, our evaluation leads to the classification process. The classification started with feature selection for machine learning algorithms and training the classification algorithm. The Validation of the training was performed using n-cross validation. At the final stage, the test classification was analyzed using the ROC curve and AUC.

3.1 Histogram analysis and threshold

The histogram analysis mentioned in section 2.5.2 shows data distribution. In figure 3.2, we see the histogram plot for a single patient. The proportion of necrosis is scarce compared to NCE and CE. The patients with low-grade tumors do not have necrosis and CE region, due to which the total necrosis in all patients is even smaller, as in the figure 3.1. NCE is the abundant voxel of tumor region, which is clearly

visible in figures 3.2 and 3.1. The histogram also includes the peritumoral regions. The median on the histogram tells us that most of the voxel values lie below one. Only a few outlier voxels lie above ten, so ten was used as the upper threshold for our evaluation. For lower threshold, Table 3 from Hangel et al. (2021) was used to derive metabolite ratio concentration estimates for different regions. The min, mean, and a max of the estimated ratio concentration were analyzed as a lower threshold for each metabolite ratio. Applying upper and lower thresholds for the data helped us focus on hotspots and avoid outliers. Likewise, figure 3.1 shows the histogram for data of all the patients. Here we see the histogram for GPC+PCh to NAA+NAAG. Similar histograms were plotted and analyzed for all the metabolite ratios. We concluded from the histogram plot that our data is right-skewed, and an upper threshold of ten can be applied to the data as only a few outliers were present beyond this threshold.

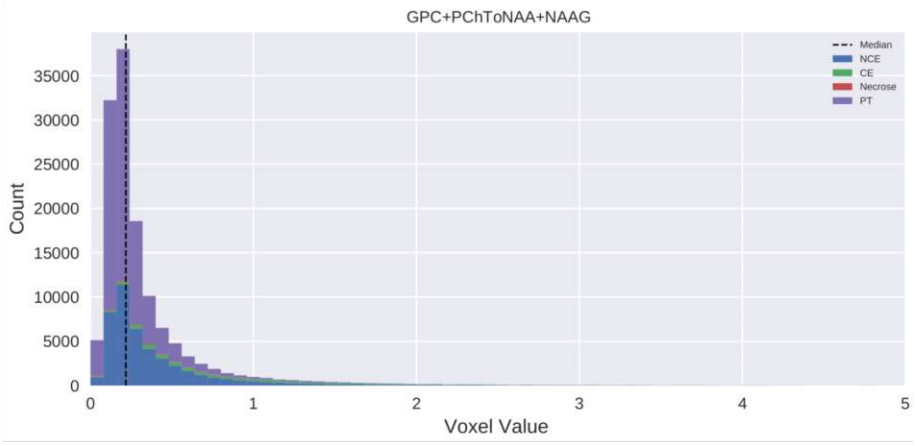

Figure 3.1: Histogram plot for all patients for metabolites ratio GPC+PCh to NAA+NAAG.NEC: Necrosis / CE: Contrast Enhancing / NCE: Non-Contrast Enhancing/ PT: Peritumoral Region

Die approbierte gedruckte Originalversion dieser Diplomarbeit ist an der TU Wien Bibliothek verfügbar
The approved original version of this thesis is available in print at TU Wien Bibliothek.
TU Bibliothek Your knowledge hub WIEN

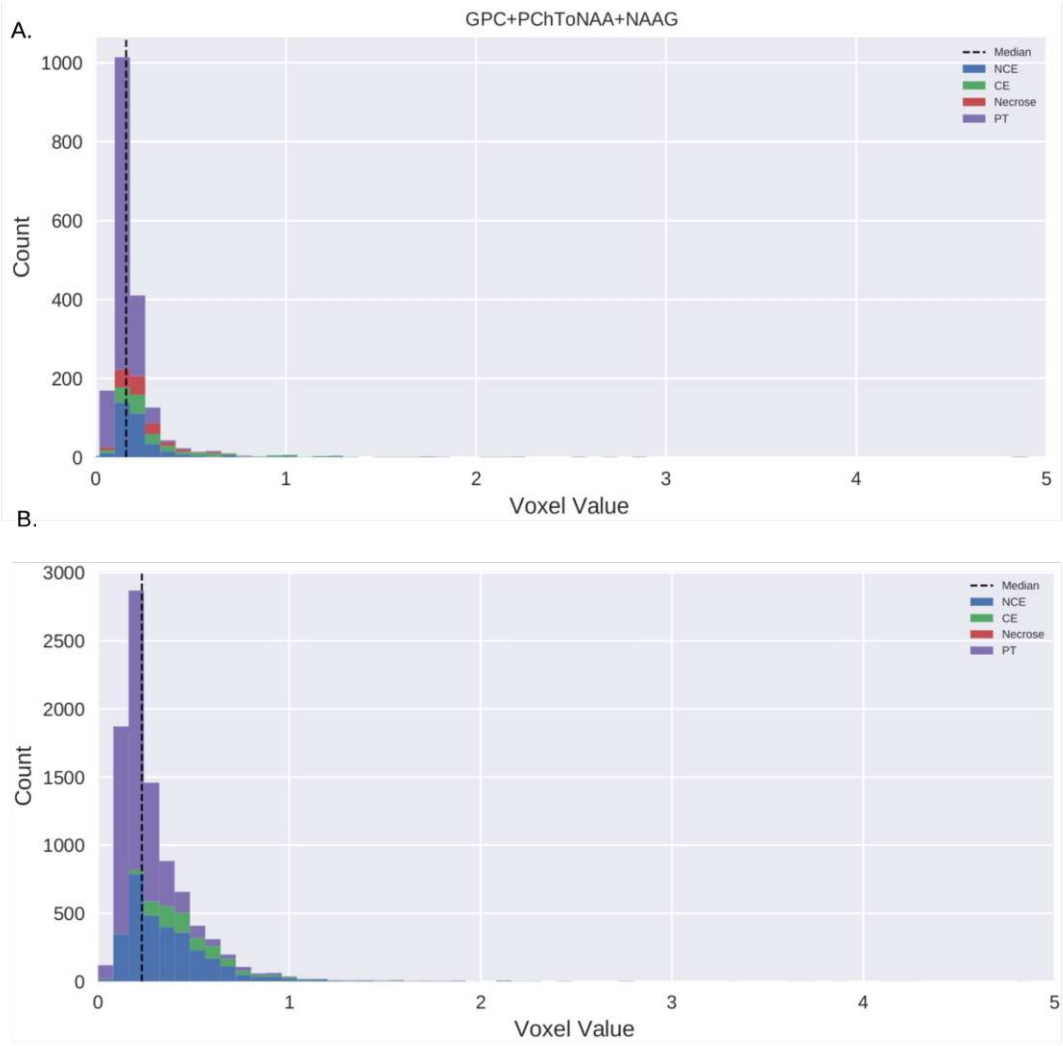

Figure 3.2: Histogram plot for single patients for metabolites ratio GPC+PCh to NAA+NAAG. Figure A above shows the patient with HGG with necrosis region in it. Whereas figure B below has no necrosis.NEC: Necrosis / CE: Contrast Enhancing / NCE: Non-Contrast Enhancing/ PT: Peritumoral Region

Die approbierte gedruckte Originalversion dieser Diplomarbeit ist an der TU Wien Bibliothek verfügbar
The approved original version of this thesis is available in print at TU Wien Bibliothek.

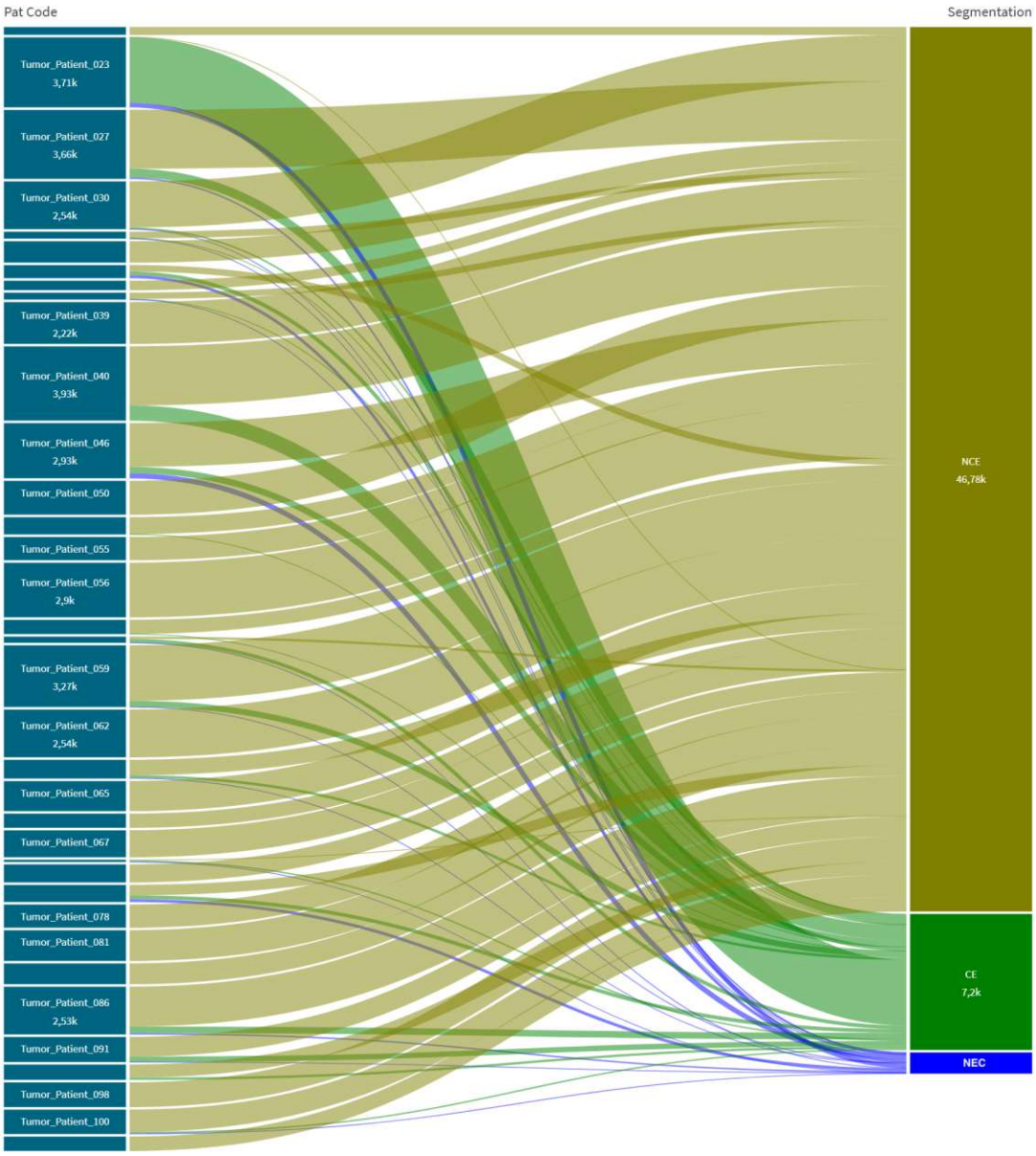

Figure 3.3: Sankey diagram to show the proportion of tumor regions obtained from each patient. NEC: Necrosis / CE: Contrast Enhancing / NCE: Non-Contrast Enhancing/ PT: Peritumoral Region

The Sankey diagram in figure 3.3 shows the proportion of tumor regions obtained

Die approbierte gedruckte Originalversion dieser Diplomarbeit ist an der TU Wien Bibliothek verfügbar
The approved original version of this thesis is available in print at TU Wien Bibliothek.

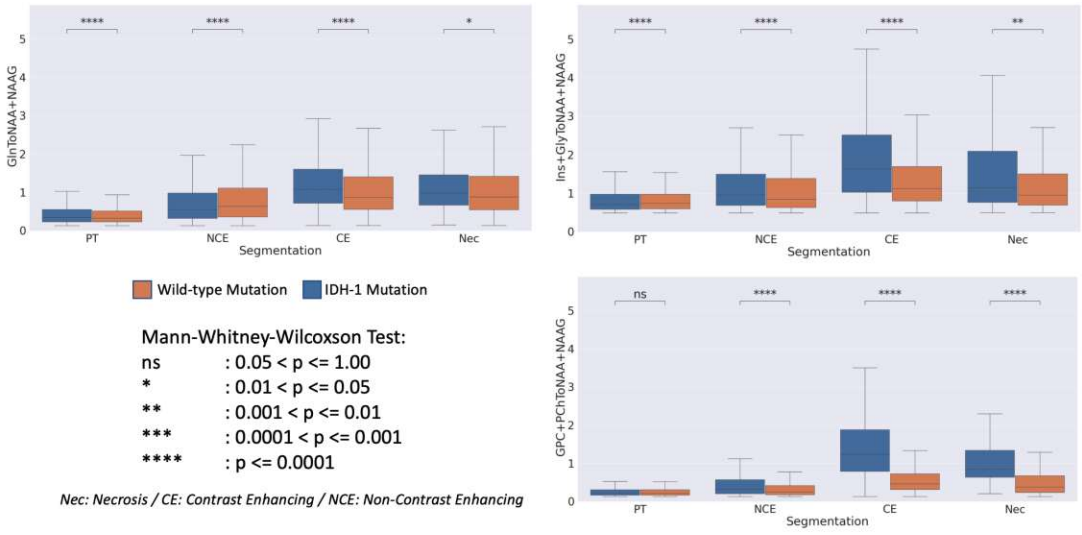

Figure 3.4: Boxplot for three different ratio metabolites (GPC+PCh/NAA+NAAG, Ins+Gly/NAA+NAAG, and Gln/NAA+NAAG) for Contrast Enhancing, Non-Contrast Enhancing, Necrosis and Paratumoral regions separately along with the result from Mann-Whitney-Wilcoxen Test for IDH differentiation.

from each patient.

3.2 IDH and grade differentiation

As mentioned in the section 2.5.3, the IDH and grade differentiation were visualized using boxplots and calculated using the Mann-Whitney-Wilcoxon test.

The result from the Mann-Whitney-Wilcoxon test can be seen in figure 3.4 and 3.5 along with the boxplots. Figure 3.4 and 3.5 show the boxplot for three different metabolite ratios for different regions.

The boxplots in figure 3.4 show a significant difference between IDH-1 mutation patients and Wild-type mutation patients for all three tumor segmentation for all three metabolites, GPC+PCh/NAA+NAAG, Ins+Gly/NAA+NAAG, and Gln/NAA+NAAG.

Die approbierte gedruckte Originalversion dieser Diplomarbeit ist an der TU Wien Bibliothek verfügbar
The approved original version of this thesis is available in print at TU Wien Bibliothek.

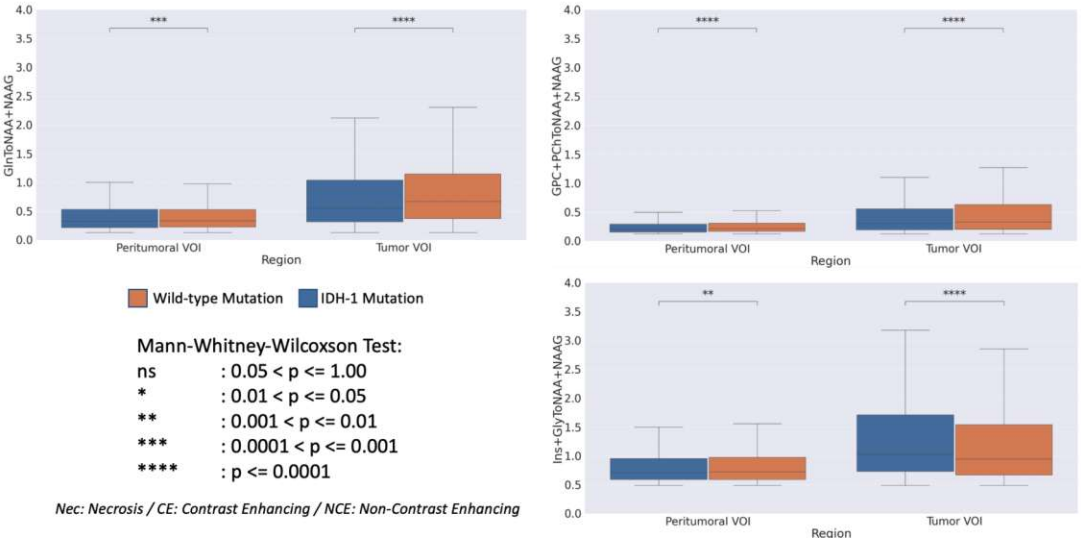

Figure 3.5: Boxplot for three different ratio metabolites (Gln/NAA+NAAG, GPC+PCh/NAA+NAAG, and Ins+Gly/NAA+NAAG) for Contrast Enhancing, Non-Contrast Enhancing, Necrosis and Paratumoral regions separately along with the result from Mann-Whitney-Wilcoxen Test for grade differentiation.

The same is valid for grades as well. However, the p-value is not always the same for all metabolites, representing the differentiation degree. The higher the difference the better it is for classification.

The difference between the peritumoral and tumor regions was also interesting to investigate. So, we also performed the Mann-Whitney-Wilcoxon test in the peritumoral region. Figure 3.4 and 3.5 also show the test results in the peritumoral region. As in figure 3.4, a significant difference was found for Gln/NAA+NAAG and Ins+Gly/NAA+NAAG in the peritumoral region and was insignificant for GPC+PCh/NAA+NAAG. In the case of LGG and HGG, the differences in all three metabolite ratios were significant.

Mann-Whitney-Wilcoxon test was performed for all the metabolite ratios men-

Die approbierte gedruckte Originalversion dieser Diplomarbeit ist an der TU Wien Bibliothek verfügbar
The approved original version of this thesis is available in print at TU Wien Bibliothek.

tioned in 2.5.1.

The boxplot diagram shows a difference in metabolite ratio concentration between tumors with and without IDH-1 mutation. Still, we cannot define metabolite as a biomarker for classifying IDH-1 mutation based on a boxplot. We used different statistical models for IDH classification, which will be discussed later in this thesis. Boxplot helps us to identify the essential metabolite ratios for the classification process. With classification using machine learning, we can combine this differentiation for significant classification of IDH. The same is valid for grade classification.

Thus, the significant IDH and grade differentiation results of the boxplot and Mann-Whitney-Wilcoxon test lead us to the possibility of classification of IDH and grade using a combination of different metabolites. Machine learning is the right tool for that purpose.

3.3 IDH and grade classification

Feature selection is key to reliable classification. Before moving to classification, it is important to know the features. In order to determine the proper set of features for classification, we work on feature selection.

We started by looking at the correlation of the features.

Die approbierte gedruckte Originalversion dieser Diplomarbeit ist an der TU Wien Bibliothek verfügbar
The approved original version of this thesis is available in print at TU Wien Bibliothek.
TU Bibliothek Your knowledge hub WIEN

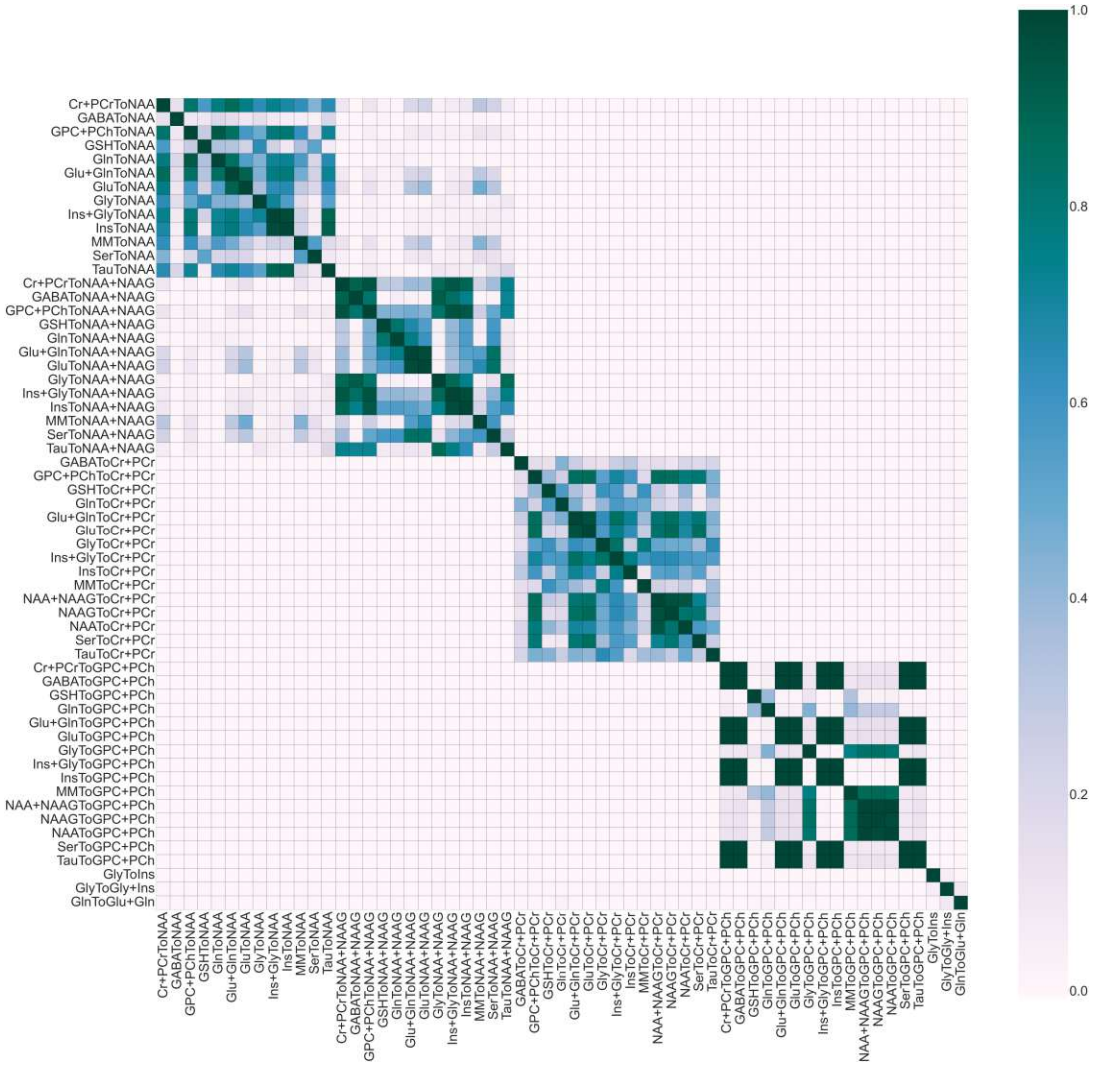

Figure 3.6: Correlation map for the metabolite ratios.

Figure 3.6 shows the correlation of features used for classification.

One of two similar features with more than 95 percent co-relation was eliminated. As explained in the method, a cross-validation score was used to determine the number of features. The cross-validation scores used for feature selection for IDH and grade classification are shown in figure 3.7 and 3.8.

Die approbierte gedruckte Originalversion dieser Diplomarbeit ist an der TU Wien Bibliothek verfügbar
The approved original version of this thesis is available in print at TU Wien Bibliothek.
TU Bibliothek Your knowledge hub WIEN

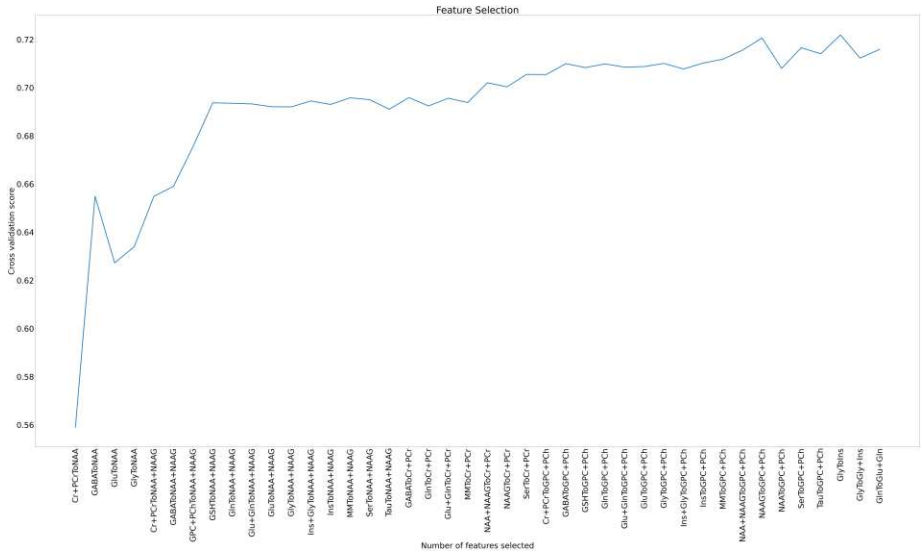

Figure 3.7: Cross-validation score determining features for IDH classification.

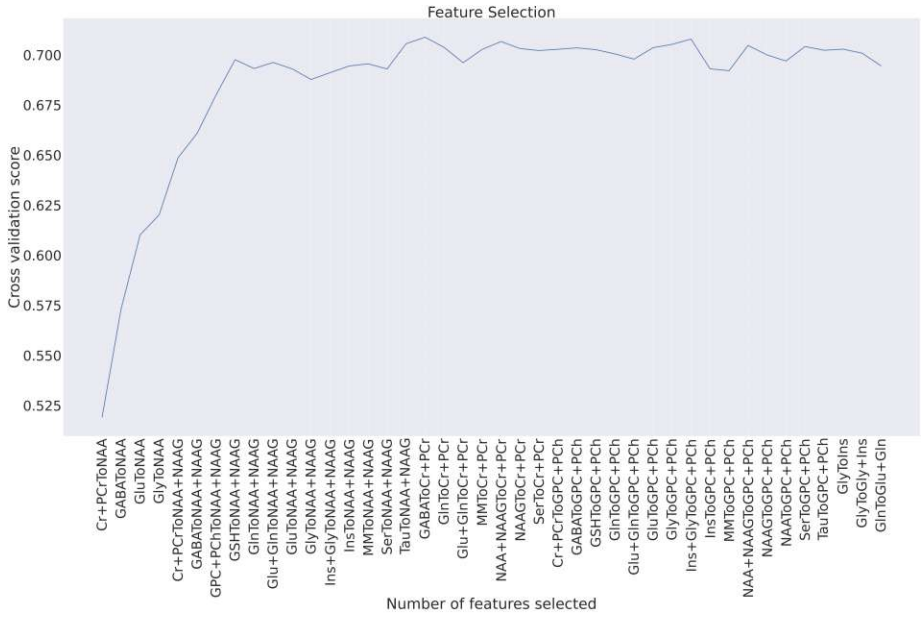

Figure 3.8: Cross-validation score determining features for grade classification.

Die approbierte gedruckte Originalversion dieser Diplomarbeit ist an der TU Wien Bibliothek verfügbar
The approved original version of this thesis is available in print at TU Wien Bibliothek.
TU Bibliothek Your knowledge hub WIEN

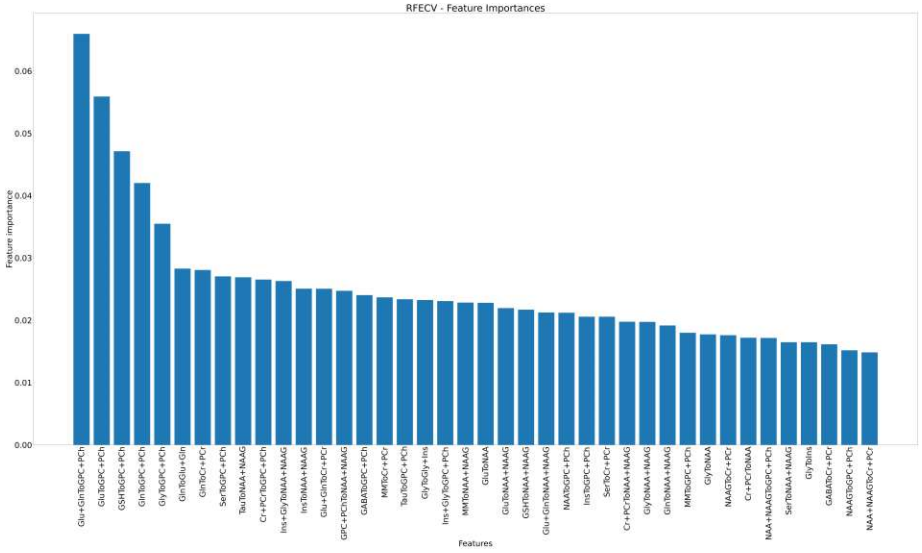

Figure 3.9: Important features for IDH classification with their relative importance.

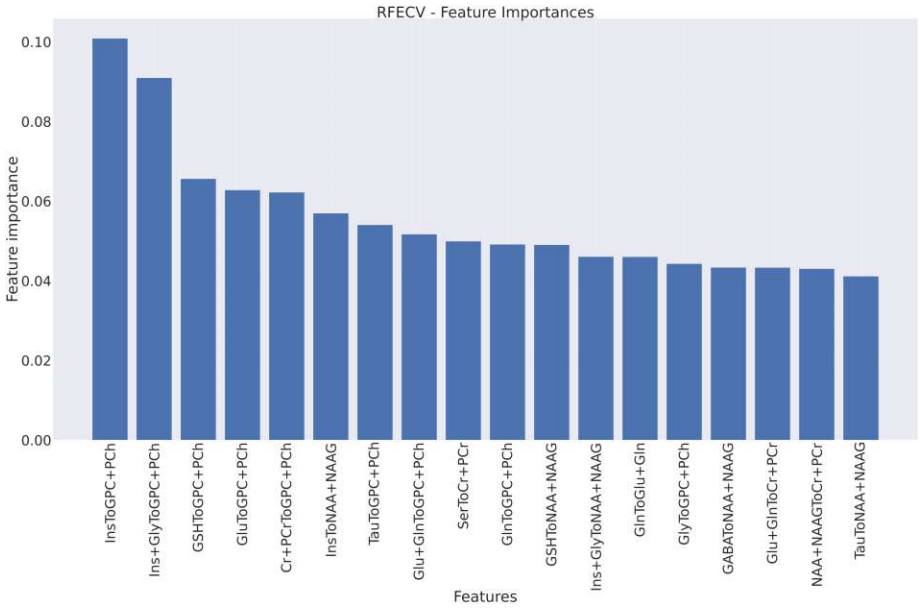

Figure 3.10: Important features for grade classification with their relative importance.

Die approbierte gedruckte Originalversion dieser Diplomarbeit ist an der TU Wien Bibliothek verfügbar
The approved original version of this thesis is available in print at TU Wien Bibliothek.
TU Bibliothek Your knowledge hub WIEN

Based on these CV scores, the number of features is determined. The feature importance plot in 3.9 and 3.10 shows important features for IDH and grade classification.

The first ten metabolite ratios in figure 3.9 and 3.10 are used to classify IDH and grade. Glu+GlnToGPC+PCH, GluToGPC+PCH, and GSHToGPC+PCh have higher contributions in IDH classification, and similarly, InsToGPC+PCh, Ins+GlyToGPC+PCh, and GSHToGPC+PCh have a higher importance in grade classification. The graphical representation of the IDH mutation prediction probability for each voxel of a patient is presented in figure 3.11.

The cross-validation score in the figures 3.7 and 3.8 and feature importance in the figures 3.9 and 3.10 is for the tumor data filtered by the mean threshold, as mentioned in the section 2.5.6. Similar cross-validation scores and feature importance analyses were also done for minimum, maximum, and without thresholds. The classification result will be presented in the latter part of this thesis.

3.4 ROC curve and AUC

As we have determined the list of important features. The classification was done using these features for one to ten features. We tried to find a suitable number of features for the classification and how the classification develops with increasing features. It was found that in all the cases, there was no significant improvement in performance.

As mentioned in the method, the classification using GPC+PChToNAA+NAAG as a single feature and multiple features was compared. Here are some of the classification results.

Die approbierte gedruckte Originalversion dieser Diplomarbeit ist an der TU Wien Bibliothek verfügbar
The approved original version of this thesis is available in print at TU Wien Bibliothek.
TU Bibliothek Your knowledge hub WIEN

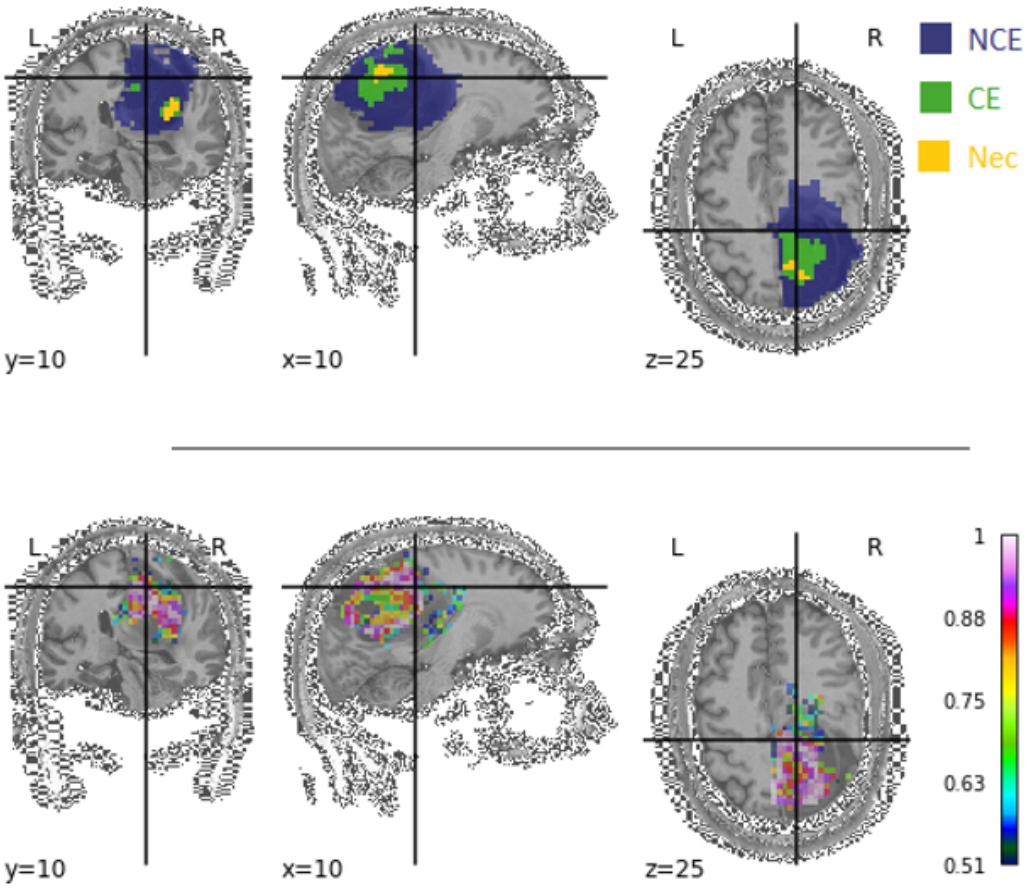

Figure 3.11: IDH prediction probability for each voxel in a patient was calculated using the leave-one-out method.

Die approbierte gedruckte Originalversion dieser Diplomarbeit ist an der TU Wien Bibliothek verfügbar
The approved original version of this thesis is available in print at TU Wien Bibliothek.

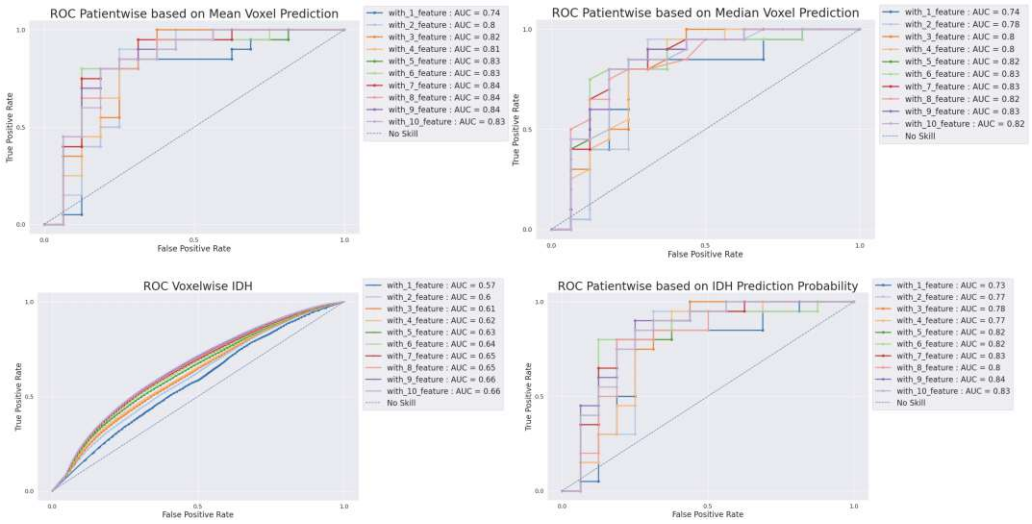

Figure 3.12: ROC curve with corresponding AUC for IDH classification with multiple features using random forest. The four different methods of aggregated classification can be seen in the figure.

3.4.1 Classification with multiple features

The classification was done using the first ten features from feature selection iteratively, as seen in the figure below. The presented results are for mean thresholds with random forest and SVM. The ROC curves were also analyzed for min, max, and without thresholds.

The figures 3.12, 3.13, 3.14 and 3.15 are for IDH and Grade classification using random forest and SVM. Four different subplots in the above ROC curves are for different ways of aggregating voxelwise classification to patients classification, including voxelwise classification as mentioned in 2.5.8. With all these aggregation methods, we tried to find which of these aggregations is effective in classifying IDH and grade tumors effectively. These figures show that the classification gets better with increasing features. However, the classification does not improve with additional metabolites later. This analysis concludes that using more than ten metabolites does

Die approbierte gedruckte Originalversion dieser Diplomarbeit ist an der TU Wien Bibliothek verfügbar
The approved original version of this thesis is available in print at TU Wien Bibliothek.

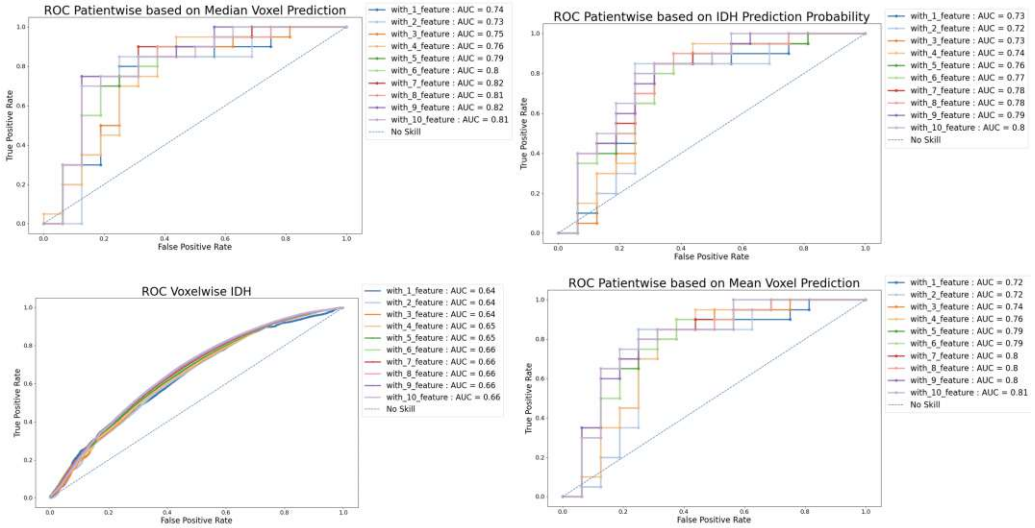

Figure 3.13: ROC curve with corresponding AUC for IDH classification with multiple features using SVM. The four different methods of aggregated classification can be seen in the figure.

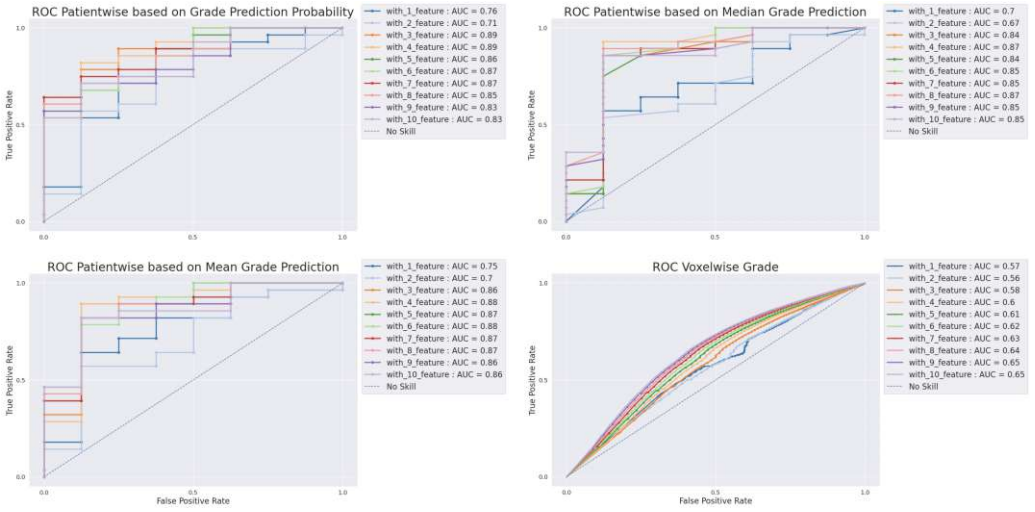

Figure 3.14: ROC curve with corresponding AUC for grade classification with multiple features using random forest. The four different methods of aggregated classification can be seen in the figure.

Die approbierte gedruckte Originalversion dieser Diplomarbeit ist an der TU Wien Bibliothek verfügbar
The approved original version of this thesis is available in print at TU Wien Bibliothek.
TU Bibliothek Your knowledge hub WIEN

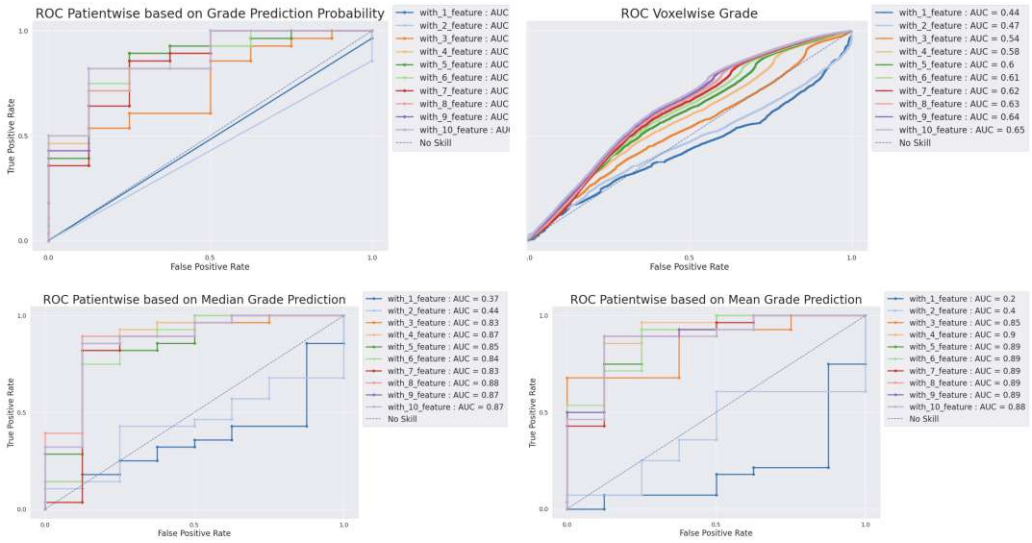

Figure 3.15: ROC curve with corresponding AUC for grade classification with multiple features using SVM. The four different methods of aggregated classification can be seen in the figure.

not improve the classification.

3.4.2 Classification with a single feature

The classification using GPC+PChToNAA+NAAG was done for comparison as a single-featured classification.

The figures 3.16, 3.17, 3.18 and 3.19 are for IDH and Grade classification using random forest and SVM. Each subplot again represents aggregation methods for patient classification. In the above figures, the classification was conducted using GPC+PCh/NAA+NAAG. The metabolite ratio was chosen based on its popularity and past knowledge in the brain's MRSI research field. Each ROC curves in subplots represent different threshold parameters as mentioned in section 2.5.6.

Die approbierte gedruckte Originalversion dieser Diplomarbeit ist an der TU Wien Bibliothek verfügbar
The approved original version of this thesis is available in print at TU Wien Bibliothek.

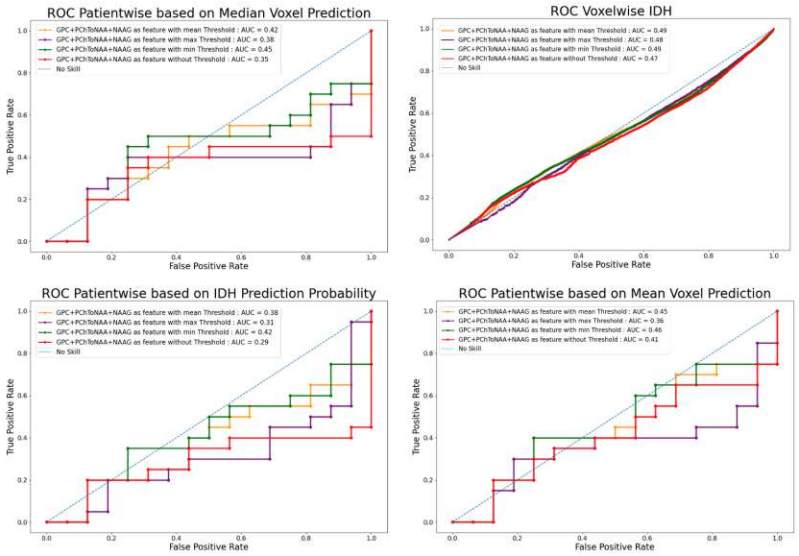

Figure 3.16: ROC curve with corresponding AUC for IDH classification with GPC+PCH/NAA+NAAG using random forest. The four different methods of aggregated classification can be seen in the figure.

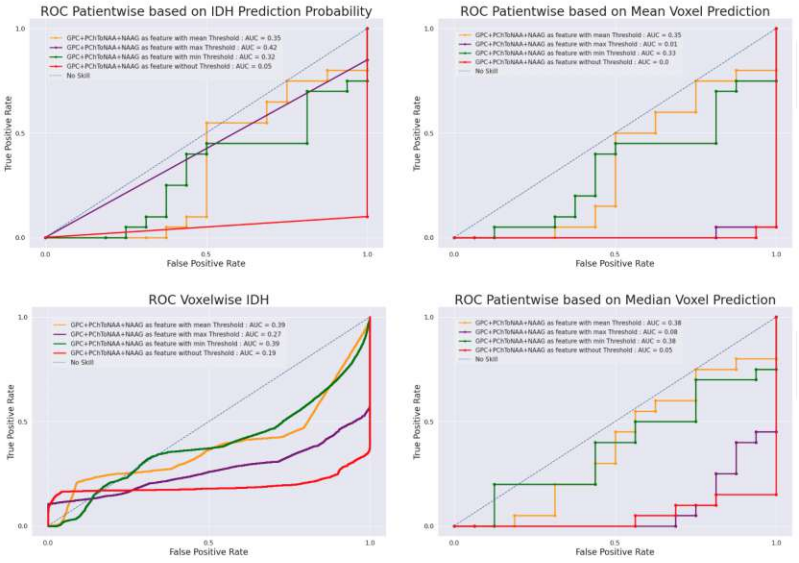

Figure 3.17: ROC curve with corresponding AUC for IDH classification with GPC+PCH/NAA+NAAG using SVM. The four different methods of aggregated classification can be seen in the figure.

Die approbierte gedruckte Originalversion dieser Diplomarbeit ist an der TU Wien Bibliothek verfügbar
The approved original version of this thesis is available in print at TU Wien Bibliothek.

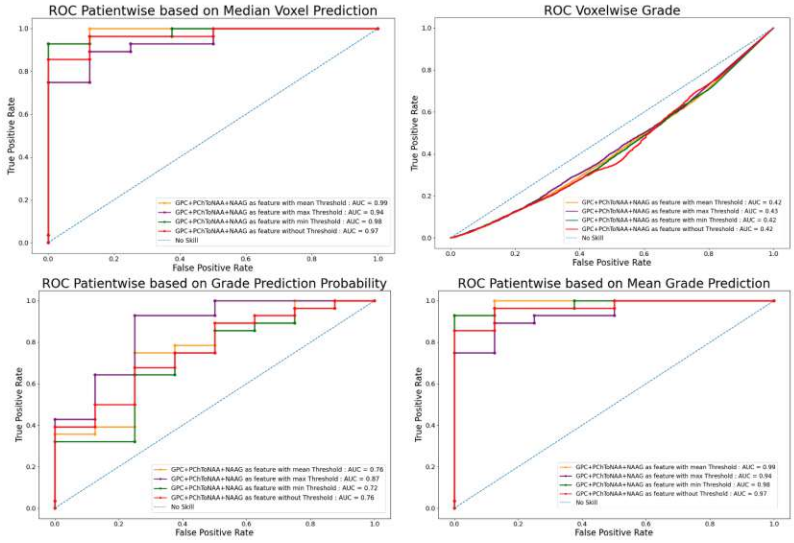

Figure 3.18: ROC curve with corresponding AUC for grade classification with GPC+PCH/NAA+NAAG using random forest. The four different methods of aggregated classification can be seen in the figure.

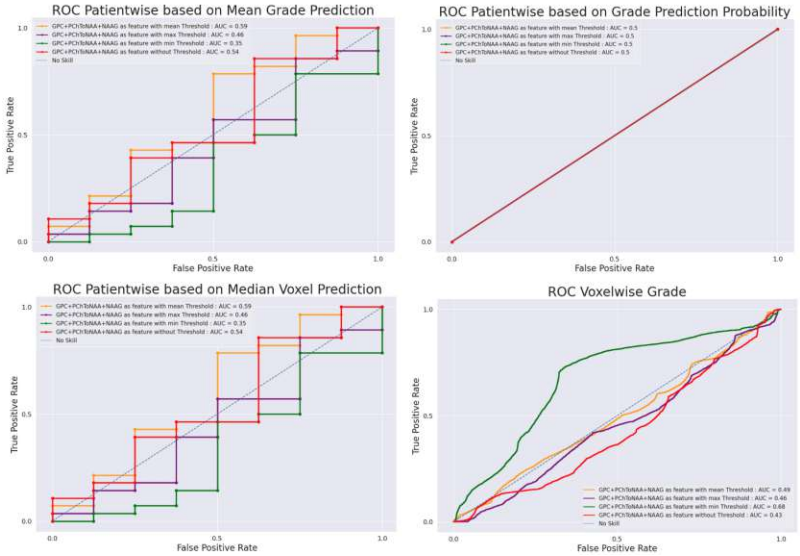

Figure 3.19: ROC curve with corresponding AUC for grade classification with GPC+PCH/NAA+NAAG using SVM. The four different methods of aggregated classification can be seen in the figure.

Die approbierte gedruckte Originalversion dieser Diplomarbeit ist an der TU Wien Bibliothek verfügbar
The approved original version of this thesis is available in print at TU Wien Bibliothek.
TU Bibliothek Your knowledge hub WIEN

IDH

			Feature : 1	Feature : 2	Feature : 3	Feature : 4	Feature : 5	Feature : 6	Feature : 7	Feature : 8	Feature : 9	Feature : 10	GPC+PCh/NAA+NAAG
Mean Voxel Prediction	RF	Ohne Threshold	0,71	0,77	0,77	0,78	0,81	0,8	0,79	0,8	0,8	0,8	0,41
		Min Threshold	0,72	0,79	0,79	0,79	0,77	0,8	0,81	0,81	0,82	0,82	0,46
		Mean Threshold	0,74	0,8	0,82	0,81	0,83	0,83	0,84	0,84	0,84	0,83	0,45
		Max Threshold	0,74	0,79	0,8	0,84	0,84	0,86	0,85	0,83	0,84	0,84	0,36
	SVM	Ohne Threshold	0,38	0,65	0,65	0,65	0,65	0,65	0,65	0,66	0,69	0,68	0
		Min Threshold	0,72	0,71	0,71	0,73	0,75	0,77	0,76	0,77	0,76	0,76	0,33
		Mean Threshold	0,72	0,72	0,74	0,76	0,79	0,79	0,8	0,8	0,8	0,81	0,35
		Max Threshold	0,67	0,77	0,78	0,82	0,82	0,79	0,79	0,81	0,82	0,81	0,01
Median Voxel Prediction	RF	Ohne Threshold	0,71	0,76	0,75	0,76	0,79	0,79	0,79	0,8	0,78	0,77	0,35
		Min Threshold	0,72	0,78	0,79	0,78	0,77	0,8	0,8	0,81	0,82	0,82	0,45
		Mean Threshold	0,74	0,78	0,8	0,8	0,82	0,83	0,83	0,82	0,83	0,82	0,42
		Max Threshold	0,77	0,78	0,79	0,84	0,85	0,85	0,85	0,83	0,84	0,84	0,38
	SVM	Ohne Threshold	0,41	0,68	0,68	0,66	0,66	0,65	0,66	0,67	0,7	0,69	0,05
		Min Threshold	0,72	0,73	0,73	0,74	0,78	0,77	0,76	0,76	0,75	0,75	0,38
		Mean Threshold	0,74	0,73	0,75	0,76	0,79	0,8	0,82	0,81	0,82	0,81	0,38
		Max Threshold	0,7	0,77	0,78	0,84	0,84	0,8	0,8	0,8	0,81	0,81	0,08
Prediction Probability	RF	Ohne Threshold	0,72	0,75	0,74	0,74	0,77	0,77	0,76	0,77	0,79	0,78	0,29
		Min Threshold	0,72	0,77	0,76	0,75	0,74	0,79	0,81	0,8	0,83	0,82	0,42
		Mean Threshold	0,73	0,77	0,78	0,77	0,82	0,82	0,83	0,8	0,84	0,83	0,38
		Max Threshold	0,77	0,76	0,78	0,84	0,84	0,84	0,84	0,83	0,82	0,83	0,31
	SVM	Ohne Threshold	0,3	0,64	0,65	0,64	0,64	0,63	0,63	0,63	0,65	0,66	0,05
		Min Threshold	0,71	0,71	0,71	0,72	0,74	0,76	0,71	0,7	0,69	0,71	0,32
		Mean Threshold	0,73	0,72	0,73	0,74	0,76	0,77	0,78	0,78	0,79	0,8	0,35
		Max Threshold	0,65	0,76	0,77	0,81	0,8	0,75	0,75	0,77	0,77	0,77	0,42
Voxelwise	RF	Ohne Threshold	0,54	0,57	0,58	0,59	0,6	0,61	0,61	0,62	0,62	0,63	0,47
		Min Threshold	0,56	0,59	0,61	0,61	0,62	0,63	0,63	0,64	0,65	0,65	0,49
		Mean Threshold	0,57	0,6	0,61	0,62	0,63	0,64	0,65	0,65	0,66	0,66	0,49
		Max Threshold	0,57	0,6	0,62	0,64	0,65	0,66	0,67	0,67	0,67	0,68	0,48
	SVM	Ohne Threshold	0,44	0,49	0,52	0,53	0,54	0,58	0,55	0,55	0,56	0,56	0,19
		Min Threshold	0,62	0,63	0,64	0,64	0,64	0,65	0,65	0,65	0,65	0,64	0,39
		Mean Threshold	0,64	0,64	0,64	0,65	0,65	0,66	0,66	0,66	0,66	0,66	0,39
		Max Threshold	0,59	0,61	0,63	0,66	0,67	0,67	0,67	0,67	0,67	0,67	0,27

Figure 3.20: Summary of AUC values for IDH classification. The summary includes classification with different features and GPC+PChToNAA+NAAG as a single feature with SVM and random forest methods.

The following figures 3.20 and 3.21 show the summary of all the AUC obtained from the classifications mentioned above.

Die approbierte gedruckte Originalversion dieser Diplomarbeit ist an der TU Wien Bibliothek verfügbar
The approved original version of this thesis is available in print at TU Wien Bibliothek.
TU Bibliothek Your knowledge hub WIEN

GRADE

			Feature : 2	Feature : 3	Feature : 4	Feature : 5	Feature : 6	Feature : 7	Feature : 8	Feature : 9	Feature : 10	GPC+PCh/NAA+NAAG
Mean Voxel Prediction	RF	Ohne Threshold	0,72	0,79	0,85	0,75	0,85	0,83	0,81	0,81	0,85	0,97
		Min Threshold	0,83	0,88	0,88	0,87	0,84	0,85	0,86	0,86	0,86	0,98
		Mean Threshold	0,7	0,86	0,88	0,87	0,88	0,87	0,87	0,86	0,86	0,99
		Max Threshold	0,71	0,67	0,73	0,76	0,88	0,83	0,82	0,83	0,83	0,94
	SVM	Ohne Threshold	0,47	0,45	0,62	0,54	0,55	0,6	0,58	0,56	0,57	0,54
		Min Threshold	0,62	0,84	0,89	0,89	0,88	0,88	0,88	0,88	0,89	0,35
		Mean Threshold	0,4	0,85	0,9	0,89	0,89	0,89	0,89	0,89	0,88	0,59
		Max Threshold	0,35	0,5	0,67	0,75	0,86	0,85	0,74	0,72	0,73	0,46
Median Voxel Prediction	RF	Ohne Threshold	0,71	0,79	0,84	0,75	0,83	0,81	0,83	0,8	0,85	0,97
		Min Threshold	0,82	0,87	0,86	0,86	0,81	0,85	0,86	0,86	0,86	0,98
		Mean Threshold	0,67	0,84	0,87	0,84	0,85	0,85	0,87	0,85	0,85	0,99
		Max Threshold	0,67	0,63	0,71	0,76	0,84	0,81	0,8	0,84	0,84	0,94
	SVM	Ohne Threshold	0,49	0,59	0,8	0,67	0,71	0,88	0,81	0,76	0,77	0,54
		Min Threshold	0,79	0,91	0,89	0,89	0,88	0,83	0,84	0,86	0,88	0,35
		Mean Threshold	0,44	0,83	0,87	0,85	0,84	0,83	0,88	0,87	0,87	0,59
		Max Threshold	0,55	0,53	0,67	0,76	0,83	0,81	0,77	0,77	0,75	0,46
Prediction Probability	RF	Ohne Threshold	0,75	0,8	0,81	0,73	0,86	0,86	0,82	0,82	0,86	0,76
		Min Threshold	0,86	0,88	0,89	0,87	0,88	0,81	0,83	0,84	0,83	0,72
		Mean Threshold	0,71	0,89	0,89	0,86	0,87	0,87	0,85	0,83	0,83	0,76
		Max Threshold	0,69	0,68	0,78	0,8	0,86	0,82	0,79	0,83	0,81	0,87
	SVM	Ohne Threshold	0,46	0,46	0,46	0,48	0,48	0,48	0,48	0,48	0,5	0,5
		Min Threshold	0,59	0,77	0,84	0,85	0,83	0,81	0,81	0,83	0,85	0,5
		Mean Threshold	0,43	0,75	0,88	0,85	0,86	0,84	0,85	0,86	0,87	0,5
		Max Threshold	0,39	0,44	0,64	0,68	0,76	0,77	0,45	0,41	0,43	0,5
Voxelwise	RF	Ohne Threshold	0,56	0,57	0,59	0,59	0,6	0,61	0,61	0,62	0,62	0,42
		Min Threshold	0,59	0,61	0,62	0,63	0,63	0,64	0,65	0,65	0,65	0,42
		Mean Threshold	0,56	0,58	0,6	0,61	0,62	0,63	0,64	0,65	0,65	0,42
		Max Threshold	0,57	0,58	0,59	0,61	0,62	0,63	0,64	0,65	0,65	0,43
	SVM	Ohne Threshold	0,48	0,52	0,56	0,57	0,57	0,59	0,6	0,61	0,61	0,43
		Min Threshold	0,64	0,64	0,64	0,64	0,64	0,64	0,64	0,65	0,65	0,68
		Mean Threshold	0,47	0,54	0,58	0,6	0,61	0,62	0,63	0,64	0,65	0,46
		Max Threshold	0,49	0,56	0,58	0,59	0,61	0,62	0,63	0,63	0,64	0,49

Figure 3.21: Summary of AUC values for grade classification. The summary includes classification with different features and GPC+PChToNAA+NAAG as a single feature with SVM and random forest methods.

Die approbierte gedruckte Originalversion dieser Diplomarbeit ist an der TU Wien Bibliothek verfügbar
The approved original version of this thesis is available in print at TU Wien Bibliothek.
TU Bibliothek Your knowledge hub WIEN

TU Bibliothek Your knowledge hub
Die approbierte gedruckte Originalversion dieser Diplomarbeit ist an der TU Wien Bibliothek verfügbar
The approved original version of this thesis is available in print at TU Wien Bibliothek.

Die approbierte gedruckte Originalversion dieser Diplomarbeit ist an der TU Wien Bibliothek verfügbar
The approved original version of this thesis is available in print at TU Wien Bibliothek.

Chapter 4

Discussion

This study's main concern is identifying important metabolite ratios for the classification of IDH mutation and tumor grades. MRSI quantification of GPC+PCh, Cr+PCr, and NAA+NAAG mainly used in combination with other imaging techniques for non-invasive tumor grading (Boonzaier et al., 2017; Bulik et al., 2013; Caulo et al., 2014; Stadlbauer et al., 2018; Wang et al., 2016). Differences in MRSI quantification were seen for Gln, Gly, GSH, Ins, and Tau in low and high glioma grades (Kallenberg et al., 2009; McBean, 2017; Righi et al., 2010) in recent studies. Similarly, quantification of GPC+PCh, Cr+PCr, Ctn, and NAA+NAAG has been correlated with IDH mutation (Branzoli et al., 2019; Goryawala et al., 2020).

Due to the capability of 7T MRSI to map multiple metabolites, it was possible to get information about the metabolite concentration of many metabolites, which were used as features for classification. The high spectral resolution of 7T made it possible to obtain a large number of voxels even with a small cohort of patients, which fulfilled the requirement of a large amount of data for training and testing the machine learning algorithms. The histograms shown in the section 3.1 were used to

determine the range of data and avoid outliers from the data set. We found that the upper threshold of ten and the lower threshold of zero would include all the tumor segments. The Sankey plot in 3.1 shows that each patient's data distribution for different tumor regions is not uniform. Some patients rather dominate some specific segments. For example, CE region data are mostly from patient 23. This would not be a great problem for our classification as we are dealing with voxelwise classification. However, it has some influence on the aggregation of voxel classification to patient classification, specifically for patient 23. As expected, the NCE region is far more dominant in numbers than necrosis. The further thresholding of the dataset, as mentioned in section 2.5.6, focuses on the hotspot of the tumor, which increases the classification quality.

The boxplots in the section 3.2 helped identify the capability of metabolites to classify IDH and grade. The Mann-Whitney test was implemented to find the significance of the difference in IDH and grade metabolite concentration values. As shown in the figure 3.4 for three different metabolites, differentiation of voxel values for IDH-1 mutation and wildtype mutation is more persistent in CE regions than in other regions. The small number of necrosis voxels might be the region behind less significant differences in necrosis regions. Even the peritumoral region shows some differences for some metabolites, which can be due to infiltration of IDH mutation in those regions. A similar phenomenon can be seen for a grade in 3.5 where a significant difference was seen for metabolites in tumor and peritumoral volume of interest. The investigation of peritumoral regions was only limited to boxplot analysis and the Mann-Whitney test.

With favourable results from boxplots, we move forward to classification. Before starting with the classification, dealing with the feature selection is crucial. The feature selection process began with the correlation matrix map in figure 3.6. As

Die approbierte gedruckte Originalversion dieser Diplomarbeit ist an der TU Wien Bibliothek verfügbar
The approved original version of this thesis is available in print at TU Wien Bibliothek.
TU Bibliothek Your knowledge hub WIEN

we dealt with the ratios, the correlation was observed for metabolite ratios with the same denominator metabolites. The high correlation between metabolite ratios means higher feature similarity and less new information. When the correlation of features exceeded 0.95, only one metabolite was selected, and the next one was eliminated. With this result, we moved on to feature selection. Figure 3.9 and 3.10 show important grade and IDH classification features. In both the figures, ratios with GPC+PCh as the denominator have higher importance as features. Besides that, Glu, Gln, Gly and GSH are seen to be essential metabolites for IDH. Whereas Ins, Gly, Glu, and GSH are important for grade classification. Further classification was done with these features. Though we had more than ten features from feature importance, the improvement in classification was not significant for more than ten features which can also be seen in the cross-validation results in figure 3.7 and 3.8.

4.1 Classification with a single feature

The classification using GPC+PChToNAA+NAAG was not consistent. For IDH voxel classification, the AUC of 0.19 was obtained using SVM, whereas, in the case of the random forest, the classification was near about 0.50, which is a random prediction. In the case of patient classification AUC of 0.29 was obtained using random forest, and with SVM, an AUC of 0.01 was obtained, which is good but with inversed labels.

A similar scenario was observed for grade where voxel classification has an AUC of 0.42 to 0.49 for different thresholds. They performed very well, up to an AUC of 0.99 for patient classification. The result of patient classification with 0.99 is auspicious, but further investigation is required to find if this was coincidentally for this dataset or if this result is consistent for additional data.

Die approbierte gedruckte Originalversion dieser Diplomarbeit ist an der TU Wien Bibliothek verfügbar
The approved original version of this thesis is available in print at TU Wien Bibliothek.
TU Bibliothek Your knowledge hub WIEN

4.2 Classifictaion with multiple features

4.2.1 IDH Classification

The results of IDH classification are included in the section 3.4. The voxelwise classification shows progressive improvement of classification with a consecutive increment of features. The improvement is, however, constant with more than ten features which can also be seen around eight to ten featured classifications. With random forest, the AUC of up to 0.68 can be yielded with voxelwise classification. The aggregation of voxel classification results up to 0.85 AUC for patient classification, as seen in figure 3.20. Both random forest and SVM results are almost equally good for IDH classification. The min and mean threshold yield better and consistent AUC values.

4.2.2 Grade Classification

The results of grade classification are presented in the section 3.4. The voxelwise classification shows improvement in classification with an increasing number of features. The improvement is insignificant, with more than ten features in this case. The voxelwise classification shows an AUC of up to 0.65 in the best-case scenario with min and means threshold. The AUC of 0.89 was yielded for patient classification with different aggregation methods. The random forest algorithm works better with consistent results for a grade in comparison with SVM. The min and mean threshold delivers better results in comparison with other thresholds.

The results mentioned above show the very optimistic potential of 7T MRSI for

Die approbierte gedruckte Originalversion dieser Diplomarbeit ist an der TU Wien Bibliothek verfügbar
The approved original version of this thesis is available in print at TU Wien Bibliothek.
TU Bibliothek Your knowledge hub WIEN

preoperative IDH and grade prediction of the tumor. As mentioned in 1.2.1, the IDH enzyme is involved in cell homeostasis and metabolic processes, which makes it part of the glioma cycle. The mutation of IDH causes the alteration of the concentration of metabolites (Ohka et al., 2014). 7T MRSI makes mapping of metabolite with high resolution possible. Based on the mapping of 7T MRSI images, we can trace the IDH mutation and classify patients with IDH mutations. The same is valid for grades where different tumor grades can be classified based on alteration of metabolite profile caused by astrocytoma, oligodendroglioma, and glioblastoma. The metabolite Ins is considered an important metabolite in grade classification, which relates with mIns being a vital component of osmoregulation in astrocyte cells (J. L. Harris et al., 2015) with higher concentration in astrocytes than in neurons (Brand et al., 1993). In the case of IDH, the evidence of an increase in glutaminolysis is observed in gliomas with IDH1 mutation (Ohka et al., 2014), which involves the conversion of Gln to Glu through glutaminase. The glutaminolysis results in a decrease of Gln and an increase of Glu in gliomas with IDH mutation. This evidence correlates with our classification of Glu and Gln in combination with GPC+PCh, an important feature for IDH classification. GSH has a high concentration in astrocytes (Rice & Russo-Menna, 1997; Sun et al., 2006) and a decrease of GSH concentration is evidential in gliomas with IDH1 mutation (Shi et al., 2015). In this study, GSH is an important metabolite in both IDH and grade classification. The interesting finding in the study was that GPC+PChToNAA+NAAG has a very high AUC value of up to 0.99 for patient classification, which is more than even with other metabolites. However, the voxel classification with GPC+PChToNAA+NAAG is 0.19 and 0.68 for IDH and grade but not consistent for all thresholds.

The accuracy of our multifeatured RF classification is in harmony with other studies. A similar study, Tietze et al., 2018 has explored the possibility of classifying IDH

Die approbierte gedruckte Originalversion dieser Diplomarbeit ist an der TU Wien Bibliothek verfügbar
The approved original version of this thesis is available in print at TU Wien Bibliothek.
TU Bibliothek Your knowledge hub WIEN

mutation with a sensitivity of 94% and specificity of 89%. Citak-Er et al., 2018 also performed glioma grade classification similar to us using SVM and achieved 93.0% accuracy with 86.7% specificity and 96.4% sensitivity. Other studies (Falk Delgado et al., 2018; Kim et al., 2020; Tan et al., 2017) also demonstrated the potential of noninvasive imaging techniques for assessing IDH mutation status and grade in gliomas.

All the aggregation methods for voxel-to-patient classification were consistent with their results. Though the classifications were performed iteratively till ten features, in most cases, the optimal results were obtained already with six to seven features.

Die approbierte gedruckte Originalversion dieser Diplomarbeit ist an der TU Wien Bibliothek verfügbar
The approved original version of this thesis is available in print at TU Wien Bibliothek.
TU Bibliothek Your knowledge hub WIEN

Chapter 5

Conclusion and Outlook

The ability of 7T MRSI to measure the concentration of multiple metabolites with high spectral resolution is very advantageous for IDH and grade classification, even with a small cohort. The metabolites GPC+PCh, Glu, Gln, and GSH in ratio with GPC+PCh are important for preoperative IDH classification. Likewise, Ins, Gln, Glu, and GSH in ratio with GPC+PCh are key features for grade classification. The RF and SVM both deliver promising results for classification. RF was better than SVM in comparison and computationally very efficient. The GPC+PChToNAA+NAAG performs well in the classification of both IDH and grade. This study demonstrates the possibility of non-invasive classification of IDH mutation and grades using machine learning. However, we are in the very early stage of exploring this possibility. The multi-featured classification using SVM and RF performed similarly in the classification of IDH with 0.85 and 0.84 AUC for RF and SVM, respectively. The min and mean threshold in 'GPC+PChToNAA+NAAG'and 'GlnToNAA+NAAG' to filter the hotspot regions of the tumor worked better than the max or without threshold. In the case of grade again, SVM and RF yield AUC of 0.91 and 0.89, respectively

Die approbierte gedruckte Originalversion dieser Diplomarbeit ist an der TU Wien Bibliothek verfügbar
The approved original version of this thesis is available in print at TU Wien Bibliothek.
TU Bibliothek Your knowledge hub WIEN

with min and mean thresholds. The classification with higher accuracy by using machine learning algorithms, even with such a small cohort, was only possible due to the spatial resolution of 7T MRSI.

In our cohort, each patient's contribution to classifier training was not uniform. However, the larger cohort with more uniformly distributed grade and IDH patients would increase the classification accuracy. Analysis of the peritumoral regions can add some new insights in the classification of tumors. An extension of this study has future perspectives for use cases such as assisting in decision-making for treatment planning, maximum safe resection of the tumor and non-invasive control of treatment strategies.

Die approbierte gedruckte Originalversion dieser Diplomarbeit ist an der TU Wien Bibliothek verfügbar
The approved original version of this thesis is available in print at TU Wien Bibliothek.
TU Bibliothek Your knowledge hub WIEN

Bibliography

Azevedo, F. A. C., Carvalho, L. R. B., Grinberg, L. T., Farfel, J. M., Ferretti, R. E. L., Leite, R. E. P., Jacob Filho, W., Lent, R., & Herculano-Houzel, S. (2009). Equal numbers of neuronal and nonneuronal cells make the human brain an isometrically scaled-up primate brain. *The Journal of Comparative Neurology*, *513*(5), 532–541. https://doi.org/10.1002/cne.21974

Bilgic, B., Gagoski, B., Kok, T., & Adalsteinsson, E. (2013). Lipid suppression in CSI with spatial priors and highly undersampled peripheral k-space. *Magnetic Resonance in Medicine*, *69*(6), 1501–1511. https://doi.org/10.1002/mrm.24399

Bloch, F. (1946). Nuclear Induction. *Physical Review*, *70*(7-8), 460–474. https://doi.org/10.1103/PhysRev.70.460

Bogner, W., Gruber, S., Trattnig, S., & Chmelik, M. (2012). High-resolution mapping of human brain metabolites by free induction decay 1H MRSI at 7 T. *NMR in Biomedicine*, *25*(6), 873–882. https://doi.org/10.1002/nbm.1805

Boonzaier, N. R., Larkin, T. J., Matys, T., van der Hoorn, A., Yan, J.-L., & Price, S. J. (2017). Multiparametric MR Imaging of Diffusion and Perfusion in Contrast-enhancing and Nonenhancing Components in Patients with Glioblastoma. *Radiology*, *284*(1), 180–190. https://doi.org/10.1148/radiol.2017160150

Die approbierte gedruckte Originalversion dieser Diplomarbeit ist an der TU Wien Bibliothek verfügbar
The approved original version of this thesis is available in print at TU Wien Bibliothek.
TU Bibliothek Your knowledge hub WIEN

Brand, A., Richter-Landsberg, C., & Leibfritz, D. (1993). Multinuclear NMR Studies on the Energy Metabolism of Glial and Neuronal Cells. *Developmental Neuroscience*, *15*(3-5), 289–298. https://doi.org/10.1159/000111347

Branzoli, F., Deelchand, D. K., Sanson, M., Lehéricy, S., & Marjańska, M. (2019). In vivo 1H MRS detection of cystathionine in human brain tumors. *Magnetic Resonance in Medicine*, *82*(4), 1259–1265. https://doi.org/10.1002/mrm.27810

Bulik, M., Jancalek, R., Vanicek, J., Skoch, A., & Mechl, M. (2013). Potential of MR spectroscopy for assessment of glioma grading. *Clinical Neurology and Neurosurgery*, *115*(2), 146–153. https://doi.org/10.1016/j.clineuro.2012.11.002

Caulo, M., Panara, V., Tortora, D., Mattei, P. A., Briganti, C., Pravatà, E., Salice, S., Cotroneo, A. R., & Tartaro, A. (2014). Data-driven Grading of Brain Gliomas: A Multiparametric MR Imaging Study. *Radiology*, *272*(2), 494–503. https://doi.org/10.1148/radiol.14132040

Citak-Er, F., Firat, Z., Kovanlikaya, I., Ture, U., & Ozturk-Isik, E. (2018). Machine-learning in grading of gliomas based on multi-parametric magnetic resonance imaging at 3T. *Computers in Biology and Medicine*, *99*, 154–160. https://doi.org/10.1016/j.compbiomed.2018.06.009

De Graaf, R. A. (2019). *In vivo NMR spectroscopy: Principles and techniques* (3rd ed). John Wiley & Sons, Inc.

Falk Delgado, A., Nilsson, M., van Westen, D., & Falk Delgado, A. (2018). Glioma Grade Discrimination with MR Diffusion Kurtosis Imaging: A Meta-Analysis of Diagnostic Accuracy. *Radiology*, *287*(1), 119–127. https://doi.org/10.1148/radiol.2017171315

Die approbierte gedruckte Originalversion dieser Diplomarbeit ist an der TU Wien Bibliothek verfügbar
The approved original version of this thesis is available in print at TU Wien Bibliothek.
TU Bibliothek Your knowledge hub WIEN

Goodenberger, M. L., & Jenkins, R. B. (2012). Genetics of adult glioma. *Cancer Genetics*, *205*(12), 613–621. https://doi.org/10.1016/j.cancergen.2012.10.009

Gorgolewski, K. ., Burns, C. D., Madison, C. ., Clark, D. ., Halchenko, Y. O., Waskom, M. L., & Ghosh, S. S. (2011). Nipype: A Flexible, Lightweight and Extensible Neuroimaging Data Processing Framework in Python. *Frontiers in Neuroinformatics*, *5*. https://doi.org/10.3389/fninf.2011.00013

Goryawala, M., Saraf-Lavi, E., Nagornaya, N., Heros, D., Komotar, R., & Maudsley, A. A. (2020). The Association between Whole-Brain MR Spectroscopy and IDH Mutation Status in Gliomas. *Journal of Neuroimaging: Official Journal of the American Society of Neuroimaging*, *30*(1), 58–64. https://doi.org/10.1111/jon.12685

Haase, A., Frahm, J., Hanicke, W., & Matthaei, D. (1985). 1H NMR chemical shift selective (CHESS) imaging. *Physics in Medicine and Biology*, *30*(4), 341–344. https://doi.org/10.1088/0031-9155/30/4/008

Hangel, G. (2015). *Accelerated high-resolution 3D magnetic resonance spectroscopic imaging in the brain at 7 T* (Doctoral dissertation). Medical University of Vienna. https://repositorium.meduniwien.ac.at/obvumwhs/download/pdf/1714157

Hangel, G., Cadrien, C., Lazen, P., Furtner, J., Lipka, A., Hečková, E., Hingerl, L., Motyka, S., Gruber, S., Strasser, B., Kiesel, B., Mischkulnig, M., Preusser, M., Roetzer, T., Wöhrer, A., Widhalm, G., Rössler, K., Trattnig, S., & Bogner, W. (2020). High-resolution metabolic imaging of high-grade gliomas using 7T-CRT-FID-MRSI. *NeuroImage: Clinical*, *28*, 102433. https://doi.org/10.1016/j.nicl.2020.102433

Hangel, G., Spurny-Dworak, B., Lazen, P., Cadrien, C., Sharma, S., Hingerl, L., Hečková, E., Strasser, B., Motyka, S., Lipka, A., Gruber, S., Brandner, C.,

Die approbierte gedruckte Originalversion dieser Diplomarbeit ist an der TU Wien Bibliothek verfügbar
The approved original version of this thesis is available in print at TU Wien Bibliothek.
TU Bibliothek Your knowledge hub WIEN

Lanzenberger, R., Rössler, K., Trattnig, S., & Bogner, W. (2021). Inter-subject stability and regional concentration estimates of 3D-FID-MRSI in the human brain at 7 T. *NMR in Biomedicine*, *n/a*(n/a), e4596. https://doi.org/10.1002/nbm.4596

Hangel, G., Strasser, B., Považan, M., Gajdošík, M., Gruber, S., Chmelík, M., Trattnig, S., & Bogner, W. (2016). A comparison of lipid suppression by double inversion recovery, L1- and L2-regularisation for high resolution MRSI in the brain at 7 T. *ISMRM 24th Annual Meeting& Exhibition, Singapore*. https://archive.ismrm.org/2016/2354.html

Hangel, G., Strasser, B., Považan, M., Gruber, S., Chmelík, M., Gajdošík, M., Trattnig, S., & Bogner, W. (2015). Lipid suppression via double inversion recovery with symmetric frequency sweep for robust 2D-GRAPPA-accelerated MRSI of the brain at 7 T. *NMR in Biomedicine*, *28*(11), 1413–1425. https://doi.org/10.1002/nbm.3386

Hangel, G., Strasser, B., Považan, M., Heckova, E., Hingerl, L., Boubela, R., Gruber, S., Trattnig, S., & Bogner, W. (2018). Ultra-high resolution brain metabolite mapping at 7 T by short-TR Hadamard-encoded FID-MRSI. *NeuroImage*, *168*, 199–210. https://doi.org/10.1016/j.neuroimage.2016.10.043

Harris, C. R., Millman, K. J., van der Walt, S. J., Gommers, R., Virtanen, P., Cournapeau, D., Wieser, E., Taylor, J., Berg, S., Smith, N. J., Kern, R., Picus, M., Hoyer, S., van Kerkwijk, M. H., Brett, M., Haldane, A., Fernández del Río, J., Wiebe, M., Peterson, P., ... Oliphant, T. E. (2020). Array programming with NumPy. *Nature*, *585*, 357–362. https://doi.org/10.1038/s41586-020-2649-2

Harris, J. L., Choi, I.-Y., & Brooks, W. M. (2015). Probing astrocyte metabolism in vivo: Proton magnetic resonance spectroscopy in the injured and aging

Die approbierte gedruckte Originalversion dieser Diplomarbeit ist an der TU Wien Bibliothek verfügbar
The approved original version of this thesis is available in print at TU Wien Bibliothek.
TU Bibliothek Your knowledge hub WIEN

brain. *Frontiers in Aging Neuroscience*, *7*. Retrieved October 30, 2022, from https://www.frontiersin.org/articles/10.3389/fnagi.2015.00202

Hingerl, L., Bogner, W., Moser, P., Považan, M., Hangel, G., Heckova, E., Gruber, S., Trattnig, S., & Strasser, B. (2018). Density-weighted concentric circle trajectories for high resolution brain magnetic resonance spectroscopic imaging at 7T. *Magnetic Resonance in Medicine*, *79*(6), 2874–2885. https://doi.org/10.1002/mrm.26987

Hingerl, L., Strasser, B., Moser, P., Hangel, G., Motyka, S., Heckova, E., Gruber, S., Trattnig, S., & Bogner, W. (2020). Clinical High-Resolution 3D-MR Spectroscopic Imaging of the Human Brain at 7 T. *Investigative Radiology*, *55*(4), 239–248. https://doi.org/10.1097/RLI.0000000000000626

Hunter, J. D. (2007). Matplotlib: A 2d graphics environment. *Computing in science & engineering*, *9*(3), 90–95.

iChemLabs. (n.d.). ChemDoodle | Chemical Drawing Software. https://www.chemdoodle.com/

Jackson, J., Meyer, C., Nishimura, D., & Macovski, A. (1991). Selection of a convolution function for Fourier inversion using gridding (computerised tomography application). *IEEE Transactions on Medical Imaging*, *10*(3), 473–478. https://doi.org/10.1109/42.97598

Kallenberg, K., Bock, H. C., Helms, G., Jung, K., Wrede, A., Buhk, J.-H., Giese, A., Frahm, J., Strik, H., Dechent, P., & Knauth, M. (2009). Untreated Glioblastoma Multiforme: Increased Myo-inositol and Glutamine Levels in the Contralateral Cerebral Hemisphere at Proton MR Spectroscopy. *Radiology*, *253*(3), 805–812. https://doi.org/10.1148/radiol.2533071654

Kennedy, B. C., MD. (2021). Astrocytoma: Practice Essentials, Background, Pathophysiology. https://emedicine.medscape.com/article/283453-overview

Die approbierte gedruckte Originalversion dieser Diplomarbeit ist an der TU Wien Bibliothek verfügbar
The approved original version of this thesis is available in print at TU Wien Bibliothek.
TU Bibliothek Your knowledge hub WIEN

Kim, M., Jung, S. Y., Park, J. E., Jo, Y., Park, S. Y., Nam, S. J., Kim, J. H., & Kim, H. S. (2020). Diffusion- and perfusion-weighted MRI radiomics model may predict isocitrate dehydrogenase (IDH) mutation and tumor aggressiveness in diffuse lower grade glioma. *European Radiology*, *30*(4), 2142–2151. https://doi.org/10.1007/s00330-019-06548-3

Louis, D. N., Perry, A., Wesseling, P., Brat, D. J., Cree, I. A., Figarella-Branger, D., Hawkins, C., Ng, H. K., Pfister, S. M., Reifenberger, G., Soffietti, R., von Deimling, A., & Ellison, D. W. (2021). The 2021 WHO Classification of Tumors of the Central Nervous System: A summary. *Neuro-Oncology*, *23*(8), 1231–1251. https://doi.org/10.1093/neuonc/noab106

Maudsley, A., Domenig, C., Govind, V., Darkazanli, A., Studholme, C., Arheart, K., & Bloomer, C. (2009). Mapping of brain metabolite distributions by volumetric proton MR spectroscopic imaging (MRSI). *Magnetic Resonance in Medicine*, *61*(3), 548–559. https://doi.org/10.1002/mrm.21875

Maudsley, A. A., Matson, G. B., Hugg, J. W., & Weiner, M. W. (1994). Reduced phase encoding in spectroscopic imaging. *Magnetic Resonance in Medicine*, *31*(6), 645–651. https://doi.org/10.1002/mrm.1910310610

Mayer, D., Levin, Y. S., Hurd, R. E., Glover, G. H., & Spielman, D. M. (2006). Fast metabolic imaging of systems with sparse spectra: Application for hyperpolarized 13C imaging. *Magnetic Resonance in Medicine*, *56*(4), 932–937. https://doi.org/10.1002/mrm.21025

McBean, G. J. (2017). Cysteine, Glutathione, and Thiol Redox Balance in Astrocytes. *Antioxidants*, *6*(3), 62. https://doi.org/10.3390/antiox6030062

McKinney, W. et al. (2010). Data structures for statistical computing in python. *Proceedings of the 9th Python in Science Conference*, *445*, 51–56.

Die approbierte gedruckte Originalversion dieser Diplomarbeit ist an der TU Wien Bibliothek verfügbar
The approved original version of this thesis is available in print at TU Wien Bibliothek.
TU Bibliothek Your knowledge hub WIEN

Moonen, C., von Kienlin, M., van zijl, P., Cohen, J., Gillen, J., Daly, P., & Wolf, G. (1989). Comparison of single shot localization methods (STEAM and PRESS) for In vivo proton NMR spectroscopy. *NMR in biomedicine*, *2*, 201–8. https://doi.org/10.1002/nbm.1940020506

Moser, E., Stahlberg, F., Ladd, M. E., & Trattnig, S. (2012). 7-T MR—from research to clinical applications? *NMR in Biomedicine*, *25*(5), 695–716. https://doi.org/10.1002/nbm.1794

Moser, P., Bogner, W., Hingerl, L., Heckova, E., Hangel, G., Motyka, S., Trattnig, S., & Strasser, B. (2019). Non-Cartesian GRAPPA and coil combination using interleaved calibration data – application to concentric-ring MRSI of the human brain at 7T. *Magnetic Resonance in Medicine*, *82*(5), 1587–1603. https://doi.org/10.1002/mrm.27822

Ogg, R. J., Kingsley, R. B., & Taylor, J. S. (1994). WET, a T1- and B1-Insensitive Water-Suppression Method for in Vivo Localized 1H NMR Spectroscopy. *Journal of Magnetic Resonance, Series B*, *104*(1), 1–10. https://doi.org/10.1006/jmrb.1994.1048

Ohka, F., Ito, M., Ranjit, M., Senga, T., Motomura, A., Motomura, K., Saito, K., Kato, K., Kato, Y., Wakabayashi, T., Soga, T., & Natsume, A. (2014). Quantitative metabolome analysis profiles activation of glutaminolysis in glioma with IDH1 mutation. *Tumour Biology: The Journal of the International Society for Oncodevelopmental Biology and Medicine*, *35*(6), 5911–5920. https://doi.org/10.1007/s13277-014-1784-5

Ostrom, Q. T., Patil, N., Cioffi, G., Waite, K., Kruchko, C., & Barnholtz-Sloan, J. S. (2020). CBTRUS Statistical Report: Primary Brain and Other Central Nervous System Tumors Diagnosed in the United States in 2013-2017. *Neuro-Oncology*, *22*(12 Suppl 2), iv1–iv96. https://doi.org/10.1093/neuonc/noaa200

Die approbierte gedruckte Originalversion dieser Diplomarbeit ist an der TU Wien Bibliothek verfügbar
The approved original version of this thesis is available in print at TU Wien Bibliothek.
TU Bibliothek Your knowledge hub WIEN

Pan, J. W., Duckrow, R. B., Gerrard, J., Ong, C., Hirsch, L. J., Resor, S. R., Zhang, Y., Petroff, O., Spencer, S., Hetherington, H. P., & Spencer, D. D. (2013). 7T MR spectroscopic imaging in the localization of surgical epilepsy. *Epilepsia*, *54*(9), 1668–1678. https://doi.org/10.1111/epi.12322

Pedregosa, F., Varoquaux, G., Gramfort, A., Michel, V., Thirion, B., Grisel, O., Blondel, M., Prettenhofer, P., Weiss, R., Dubourg, V., et al. (2011). Scikit-learn: Machine learning in python. *Journal of machine learning research*, *12*(Oct), 2825–2830.

Posse, S., Otazo, R., Dager, S. R., & Alger, J. (2013). MR spectroscopic imaging: Principles and recent advances. *Journal of Magnetic Resonance Imaging*, *37*(6), 1301–1325. https://doi.org/10.1002/jmri.23945

Považan, M., Strasser, B., Hangel, G., Gruber, S., Trattnig, S., & Bogner, W. (2015). Multimodal post-processing software for MRSI data evaluation. *Proc Int Soc Magn Reson Med.s*.

Provencher, S. W. (2001). Automatic quantitation of localized in vivo 1H spectra with LCModel. *NMR in Biomedicine*, *14*(4), 260–264. https://doi.org/10.1002/nbm.698

Purcell, E. M., Torrey, H. C., & Pound, R. V. (1946). Resonance Absorption by Nuclear Magnetic Moments in a Solid. *Physical Review*, *69*(1-2), 37–38. https://doi.org/10.1103/PhysRev.69.37

Ratai, E., Kok, T., Wiggins, C., Wiggins, G., Grant, E., Gagoski, B., O'Neill, G., Adalsteinsson, E., & Eichler, F. (2008). Seven-Tesla proton magnetic resonance spectroscopic imaging in adult X-linked adrenoleukodystrophy. *Archives of neurology*, *65*(11), 1488–1494. https://doi.org/10.1001/archneur.65.11.1488

Die approbierte gedruckte Originalversion dieser Diplomarbeit ist an der TU Wien Bibliothek verfügbar
The approved original version of this thesis is available in print at TU Wien Bibliothek.
TU Bibliothek Your knowledge hub WIEN

Rice, M. E., & Russo-Menna, I. (1997). Differential compartmentalization of brain ascorbate and glutathione between neurons and glia. *Neuroscience*, *82*(4), 1213–1223. https://doi.org/10.1016/S0306-4522(97)00347-3

Righi, V., Andronesi, O. C., Mintzopoulos, D., Black, P. M., & Tzika, A. A. (2010). High-resolution magic angle spinning magnetic resonance spectroscopy detects glycine as a biomarker in brain tumors. *International Journal of Oncology*, *36*(2), 301–306. https://doi.org/10.3892/ijo_00000500

Shi, J., Sun, B., Shi, W., Zuo, H., Cui, D., Ni, L., & Chen, J. (2015). Decreasing GSH and increasing ROS in chemosensitivity gliomas with IDH1 mutation. *Tumor Biology*, *36*(2), 655–662. https://doi.org/10.1007/s13277-014-2644-z

Skoch, A., Jiru, F., & Bunke, J. (2008). Spectroscopic imaging: Basic principles. *European Journal of Radiology*, *67*(2), 230–239. https://doi.org/10.1016/j.ejrad.2008.03.003

Slavkovsky, P., & Uhliar, R. (2004). The Nobel Prize in Physiology or Medicine in 2003 to Paul C. Lauterbur, Peter Mansfield for magnetic resonance imaging. *Bratislavske Lekarske Listy*, *105*(7-8), 245–249.

Srinivasan, R., Ratiney, H., Hammond-Rosenbluth, K. E., Pelletier, D., & Nelson, S. J. (2010). MR spectroscopic imaging of glutathione in the white and gray matter at 7 T with an application to multiple sclerosis. *Magnetic Resonance Imaging*, *28*(2), 163–170. https://doi.org/10.1016/j.mri.2009.06.008

Stadlbauer, A., Zimmermann, M., Doerfler, A., Oberndorfer, S., Buchfelder, M., Coras, R., Kitzwögerer, M., & Roessler, K. (2018). Intratumoral heterogeneity of oxygen metabolism and neovascularization uncovers 2 survival-relevant subgroups of IDH1 wild-type glioblastoma. *Neuro-Oncology*, *20*(11), 1536–1546. https://doi.org/10.1093/neuonc/noy066

Die approbierte gedruckte Originalversion dieser Diplomarbeit ist an der TU Wien Bibliothek verfügbar
The approved original version of this thesis is available in print at TU Wien Bibliothek.
TU Bibliothek Your knowledge hub WIEN

Strasser, B., Chmelik, M., Robinson, S. D., Hangel, G., Gruber, S., Trattnig, S., & Bogner, W. (2013). Coil combination of multichannel MRSI data at 7 T: MUSICAL. *NMR in Biomedicine*, *26*(12), 1796–1805. https://doi.org/10.1002/nbm.3019

Strasser, B., Považan, M., Hangel, G., Hingerl, L., Chmelik, M., Gruber, S., Trattnig, S., & Bogner, W. (2017). (2 + 1)D-CAIPIRINHA accelerated MR spectroscopic imaging of the brain at 7T. *Magnetic Resonance in Medicine*, *78*(2), 429–440. https://doi.org/10.1002/mrm.26386

Sun, X., Shih, A. Y., Johannssen, H. C., Erb, H., Li, P., & Murphy, T. H. (2006). Two-photon Imaging of Glutathione Levels in Intact Brain Indicates Enhanced Redox Buffering in Developing Neurons and Cells at the Cerebrospinal Fluid and Blood-Brain Interface *. *Journal of Biological Chemistry*, *281*(25), 17420–17431. https://doi.org/10.1074/jbc.M601567200

Tabakov, S. D. (2021). Professor John Mallard, 1927 – 2021. *Health and Technology*, *11*(3), 443–444. https://doi.org/10.1007/s12553-021-00548-4

Tan, W., Xiong, J., Huang, W., Wu, J., Zhan, S., & Geng, D. (2017). Noninvasively detecting Isocitrate dehydrogenase 1 gene status in astrocytoma by dynamic susceptibility contrast MRI. *Journal of magnetic resonance imaging: JMRI*, *45*(2), 492–499. https://doi.org/10.1002/jmri.25358

Tietze, A., Choi, C., Mickey, B., Maher, E. A., Parm Ulhøi, B., Sangill, R., Lassen-Ramshad, Y., Lukacova, S., Østergaard, L., & von Oettingen, G. (2018). Non-invasive assessment of isocitrate dehydrogenase mutation status in cerebral gliomas by magnetic resonance spectroscopy in a clinical setting. *Journal of Neurosurgery*, *128*(2), 391–398. https://doi.org/10.3171/2016.10.JNS161793

Trattnig, S., Bogner, W., Gruber, S., Szomolanyi, P., Juras, V., Robinson, S., Zbýň, Š., & Haneder, S. (2016). Clinical applications at ultrahigh field (7 T). Where

Die approbierte gedruckte Originalversion dieser Diplomarbeit ist an der TU Wien Bibliothek verfügbar
The approved original version of this thesis is available in print at TU Wien Bibliothek.

does it make the difference? *NMR in Biomedicine*, *29*(9), 1316–1334. https://doi.org/10.1002/nbm.3272

Van Rossum, G., & Drake Jr, F. L. (1995). *Python reference manual*. Centrum voor Wiskunde en Informatica Amsterdam.

Virtanen, P., Gommers, R., Oliphant, T. E., Haberland, M., Reddy, T., Cournapeau, D., Burovski, E., Peterson, P., Weckesser, W., Bright, J., van der Walt, S. J., Brett, M., Wilson, J., Millman, K. J., Mayorov, N., Nelson, A. R. J., Jones, E., Kern, R., Larson, E., ... SciPy 1.0 Contributors. (2020). SciPy 1.0: Fundamental Algorithms for Scientific Computing in Python. *Nature Methods*, *17*, 261–272. https://doi.org/10.1038/s41592-019-0686-2

von Kienlin, M., & Mejia, R. (1991). Spectral localization with optimal pointspread function. *Journal of Magnetic Resonance (1969)*, *94*(2), 268–287. https://doi.org/10.1016/0022-2364(91)90106-4

Wang, Q., Zhang, H., Zhang, J., Wu, C., Zhu, W., Li, F., Chen, X., & Xu, B. (2016). The diagnostic performance of magnetic resonance spectroscopy in differentiating high-from low-grade gliomas: A systematic review and meta-analysis. *European Radiology*, *26*(8), 2670–2684. https://doi.org/10.1007/s00330-015-4046-z

Wilson, M., Andronesi, O., Barker, P. B., Bartha, R., Bizzi, A., Bolan, P. J., Brindle, K. M., Choi, I.-Y., Cudalbu, C., Dydak, U., Emir, U. E., Gonzalez, R. G., Gruber, S., Gruetter, R., Gupta, R. K., Heerschap, A., Henning, A., Hetherington, H. P., Huppi, P. S., ... Howe, F. A. (2019). Methodological consensus on clinical proton MRS of the brain: Review and recommendations. *Magnetic Resonance in Medicine*, *82*(2), 527–550. https://doi.org/10.1002/mrm.27742

Yan, H., Parsons, D. W., Jin, G., McLendon, R., Rasheed, B. A., Yuan, W., Kos, I., Batinic-Haberle, I., Jones, S., Riggins, G. J., Friedman, H., Friedman, A.,

Die approbierte gedruckte Originalversion dieser Diplomarbeit ist an der TU Wien Bibliothek verfügbar
The approved original version of this thesis is available in print at TU Wien Bibliothek.

Reardon, D., Herndon, J., Kinzler, K. W., Velculescu, V. E., Vogelstein, B., & Bigner, D. D. (2009). IDH1 and IDH2 mutations in gliomas. *The New England Journal of Medicine*, *360*(8), 765–773. https://doi.org/10.1056/NEJMoa0808710

Die approbierte gedruckte Originalversion dieser Diplomarbeit ist an der TU Wien Bibliothek verfügbar
The approved original version of this thesis is available in print at TU Wien Bibliothek.
TU Bibliothek Your knowledge hub WIEN